Mie Resonance Based All-Dielectric Metamaterials at Optical Frequencies

By

Parikshit Moitra

Dissertation
Submitted to the Faculty of the
Graduate School of Vanderbilt University
in partial fulfillment of the requirements
for the degree of

DOCTOR OF PHILOSOPHY
in

Interdisciplinary Materials Science
August, 2015
Nashville, Tennessee

Approved:

Professor Jason G. Valentine

Professor Sharon M. Weiss

Professor Richard F. Haglund Jr.

Professor Norman H. Tolk

Professor Deyu Li

To my beloved parents and siblings

For their never ending support and motivation

Acknowledgement

I take this opportunity to acknowledge the contribution of my professors, co-workers, friends and family for their love, support and guidance throughout my doctoral studies. Without their support the journey to completion of my PhD would not have been possible.

First and foremost, I would like to thank my PhD advisor Professor Jason Valentine for giving me the opportunity to work with him in his newly formed lab in the Summer of 2009 and introducing me to the wonder-world of metamaterials. I learned a lot from him in every aspect of research, be it numerical modeling, fabrication or experiment. I acknowledge the excellent guidance and support he provided me throughout my graduate studies.

I would also like to thank PhD committee members Prof Sharon Weiss, Prof Richard Haglund, Prof Norman Tolk and Prof Deyu Li. They not only did an excellent job in evaluating and critiquing my research, also taught me courses in Physics and Optoelectronics and let me work in their labs as Research Rotation student.

A special thanks is given to all my lab members in Valentine Lab - Wenyi Wang, Yuanmu Yang, Wei Li, Zack Coppens and Zhihua Zhu, who have been thoroughly helpful and cooperative and they made working in the lab so much fun. Thanks for all the memories.

My acknowledgement won't be complete if I do not mention the staff scientists in Vanderbilt Institute of Nanoscale Science and Engineering (VINSE) and Center for Nanophase Materials Sciences (CNMS), especially Dr. Ivan Kravchencko, Dayrl Briggs, Prof Anthony Hmelo and Dr. Benjamin Schmidt, for training me on nanofabrication tools and helping me out whenever I stumbled with any fabrication problems. I would also like to thank my collaborators, especially Dr. Brian Slovick and Dr. Srini Krishnamurthy in SRI International, for their theoretical inputs in my research.

A special thanks goes to my maternal grandfather Dr. Shankar Nath Mukherjee for motivating me to take graduate studies in the first place.

Finally and most importantly, I would like to thank my parents (Maa and Baba), my brother Parashar Moitra and my sister Pallabi Moitra, for their unconditional love and support. Thank you for believing in me.

Table of Contents

Page

List of Figures

List of Publications

Peer Reviewed

- **Parikshit Moitra**, Yuanmu Yang, Zachary Anderson, Ivan I. Kravchencko, Daryl P. Briggs & Jason Valentine. Realization of an all-dielectric zero-index optical metamaterial. ***Nature Photonics*** 7, 791–795 (2013).
- **Parikshit Moitra**, Brian Slovick, Zhi Gang Yu, Srini Krishnamurthy & Jason Valentine. Experimental demonstration of a broadband all-dielectric metamaterial perfect reflector. ***Applied Physics Letters*** 104, 171102 (2014).
- **Parikshit Moitra**, Brian Slovick, Wei Li, Ivan I. Kravchencko, Daryl P. Briggs, Srini Krishnamurthy & Jason Valentine. Large scale all-dielectric metamaterial perfect reflectors. ***ACS Photonics*** 2, 692-698 (2015)
- Yuanmu Yang, Wenyi Wang, **Parikshit Moitra**, Ivan I. Kravchencko, Daryl P. Briggs & Jason Valentine. Dielectric meta-reflectarray for broadband linear polarization conversion and optical vortex generation. ***Nano Letters*** 14, 1394-1399 (2014).
- Aditya Jain, **Parikshit Moitra**, Thomas Koschny, Jason Valentine & Costas M. Soukoulis. Electric and magnetic response in dielectric dark states for low loss subwavelength optical meta atoms. ***Accepted in Advanced Optical Materials*** (2015)

Chapter 1

Introduction

1.1 Motivation

Electromagnetic metamaterials are artificially fabricated structures that exhibit properties unattainable in naturally occurring materials, such as negative index[1]–[4], epsilon-near-zero[5]–[7], ultra-high index[8], perfect lensing[9], [10] and cloaking[4], [11]–[13]. Since their inception, metallic unit cells have dominated the field of metamaterials. However, metallic unit cells suffer from conduction loss[14]–[16], magnetic saturation at high frequencies[17], exhibit anisotropic optical responses[18] and requires expensive lithography method for fabrication and hence large area scalability is not feasible for practical applications. Recently, there has been burgeoning interest in exploiting the Mie resonances[19] in dielectric particles with simple geometries to design all-dielectric metamaterials, which not only have much less absorption losses at optical frequencies than their metallic counterparts, but also provide the potential for achieving isotropic optical responses by simplifying the design. The main motivations of this dissertation are two fold - first, to understand how electric and magnetic Mie resonances in dielectric particles can be used to design metamaterials exhibiting novel and unique optical properties; and second, to experimentally realize metamaterials using nanofabrication techniques, with a strong motivation towards scaling the metamaterial to large area for practical applications. This chapter will serve as a guide to understand the inception and brief history of metallic metamaterials and will also help us to understand the limitations of metallic unit cells and advantages of transition from metallic unit cells to their dielectric counterparts.

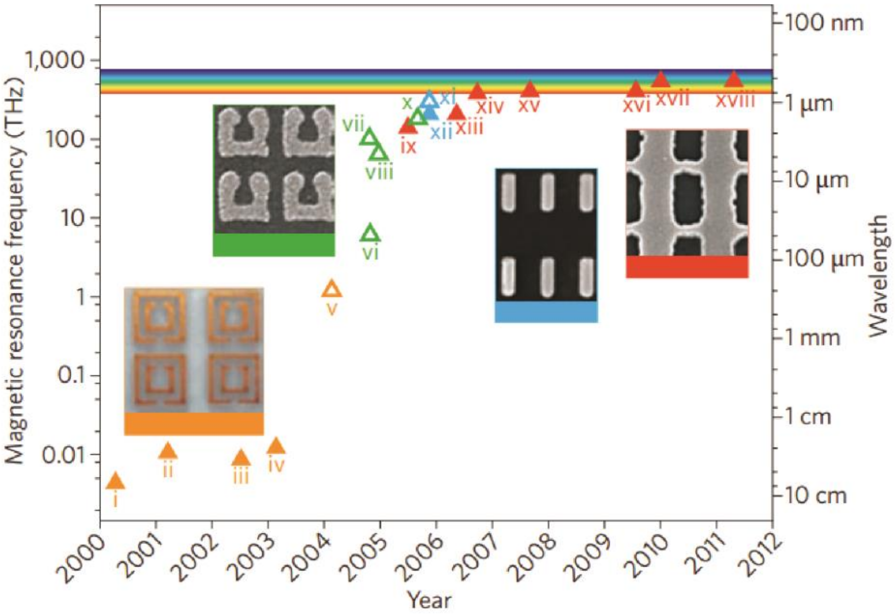

Figure 0.1 Progress of metal-based metamaterial with respect to operation frequency and time. double SRRs denoted by orange; U-shaped SRRs denoted by green; metallic cut-wire pairs denoted by blue; double fishnet structures denoted by red. The insets show optical image and scanning electron microscope images of four different types of structures. Adapted from reference[20].

1.2 Engineering Index of Refraction

The field of metamaterials provides the framework to engineer optical properties, which would not otherwise be possible using naturally occurring materials. To achieve novel optical properties metamaterials needs to be artificially fabricated with periodic or random arrays of properly structured elements or unit cells, the size and spacing of which must be much smaller than the wavelength of electromagnetic radiation. Hence, the probing wavelength cannot “see” individual unit cells and the collective response from all the unit cells can be modeled using a homogeneous effective permittivity and permeability. Most interesting of all is that the effective permeability can also be controlled by proper unit cell design.

1.2.1 Negative Index Metamaterials

It is useful to begin the discussion of metamaterials with negative index of refraction to comprehend the inception of this field and how it excited the imagination of researchers worldwide. Refractive index is a complex number given by $n = n' + n''$. n' is a measure of how the phase velocity of light is slowed down when passing through a material and n'' is a measure of absorption of electromagnetic radiation and hence loss. The complex refractive index is defined by $n = \sqrt{\varepsilon\mu}$, where ε and μ are the complex electric permittivity and magnetic permeability of a material. ε and μ define the polarizabilities of a material under the electric and magnetic field of light, respectively. Based on their ε and μ values all the materials can be categorized in terms of materials parameter space[21]. The materials parameter space is divided in four quadrants (Figure 1.2). Quadrant I lists most of the dielectric materials with simultaneous positive permittivity and permeability. Quadrant II consists of materials with negative permittivity such as metals and doped semiconductors. Quadrant IV consists of materials with negative permeability but positive permittivity, which includes some ferrite materials. The most interesting region is Quadrant III with simultaneous negative permittivity and permeability. No naturally occurring materials belong to this region of parameter space.

Veselago[22] in 1968 was the first to postulate the optical properties of a hypothetical material exhibiting simultaneous negative values of permittivity and permeability i.e. negative index of refraction. He postulated that when light propagates from a positive index to negative index material, or vice versa, it will refract in the wrong way i.e. at the same side of the normal to the interface. To understand this concept let us review Maxwell's equations (Eq. 1.1) and the constitutive equations (Eq. 1.2), where the electric and magnetic fields of incident plane wave are defined as $\vec{E}(\omega,\vec{k}) = E_0 \exp(i\vec{k}.\vec{r} - i\omega.t)$ and $\vec{H}(\omega,\vec{k}) = H_0 \exp(i\vec{k}.\vec{r} - i\omega.t)$, respectively.

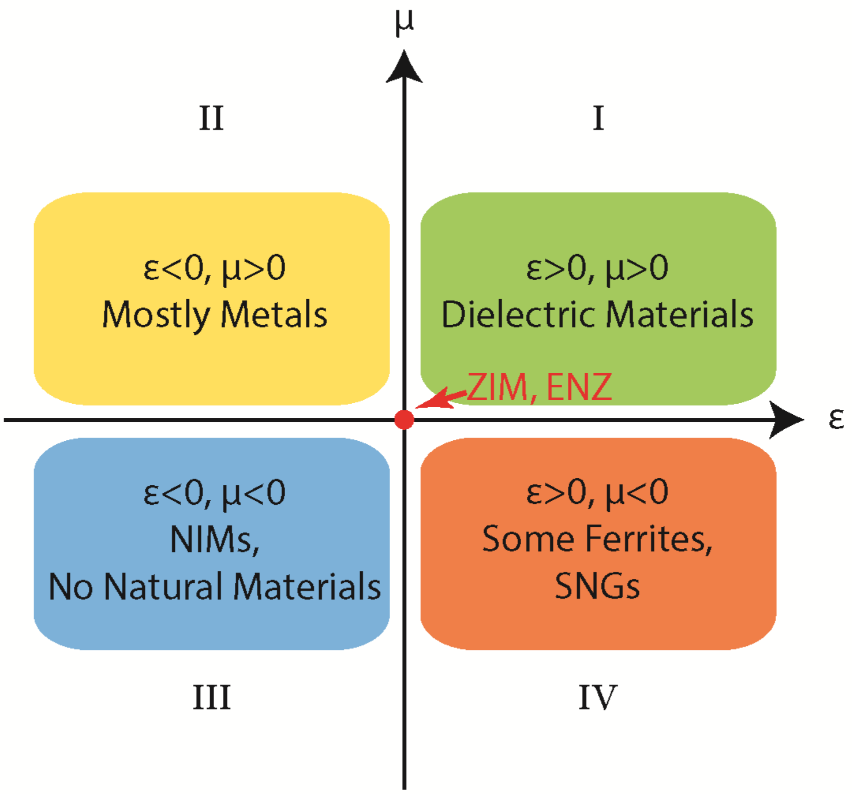

Figure 0.2 Materials parameter space illustrating different materials at different Quadrants[21].

$$\begin{aligned} &\nabla \cdot \vec{B} = 0, \\ &\nabla \times \vec{E} = -\frac{\partial \vec{B}}{\partial t}, \\ &\nabla \cdot \vec{D} = \rho, \\ &\nabla \times \vec{H} = \vec{j} + \frac{\partial \vec{D}}{\partial t}, \end{aligned} \qquad 1.1$$

$$\begin{aligned} &\vec{D} = \varepsilon \vec{E} = \varepsilon_r \varepsilon_0 \vec{E} \\ &\vec{B} = \mu \vec{H} = \mu_r \mu_0 \vec{H} \end{aligned} \qquad 1.2$$

Here, $\vec{B}$ is the magnetic flux density, $\vec{D}$ is the electric flux density, ρ is the charge density, and $\vec{j}$ is the current density. In absence of any free charges (ρ) and currents ($\vec{j}$), Eq. 1.1 and 1.2 can be simplified to

$$\vec{k}\times\vec{E}=\mu\omega\vec{H}$$
$$\vec{k}\times\vec{H}=-\varepsilon\omega\vec{E} \qquad 1.3$$

For the propagation of a plane wave in conventional dielectric materials with $\varepsilon>0$ and $\mu>0$, the triplet vectors, $\vec{k}$, $\vec{E}$ and $\vec{H}$, follow the right hand rule (Eq. 1.3). However, during propagation in a medium with $\varepsilon<0$ and $\mu<0$, these vectors follow the left-hand rule. Contrary to conventional understanding, the Poynting vector, which is defined as $\vec{S}=\vec{E}\times\vec{H}$, and the wave vector $\vec{k}$ are directed in opposite directions in such media (Figure 1.3). Furthermore, the real part of refractive index which is given by $n=\pm\sqrt{|\varepsilon_r||\mu_r|}$, should take a negative sign to conserve causality[22].

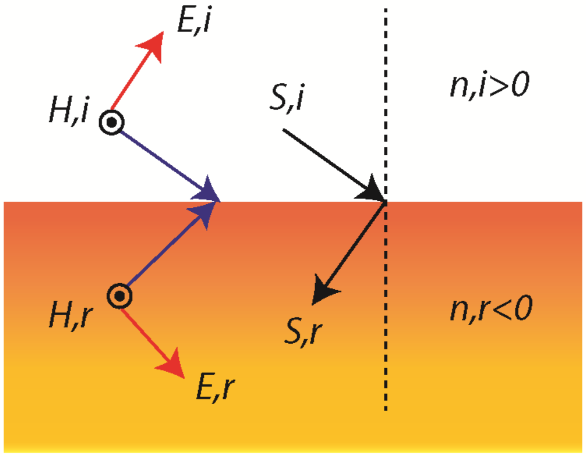

Figure 0.3 Schematic of refraction behavior when light travels from positive to negative index medium. Adapted from reference [21].

Designing Simultaneous Negative Permittivity and Permeability: Realization of negative index requires both permittivity (ε) and permeability (μ) to be negative. Realizing negative permittivity is relatively simple. Metals possess negative permittivity below plasma frequency.

The dielectric permittivity of a metal can be defined by Drude-Lorentz model at optical frequencies as,

$$\varepsilon(\omega) = 1 - \frac{\omega^2{}_p}{\omega(\omega - i\gamma)} \qquad 1.4$$

Where, ω_p is the plasma frequency of the metal and γ is the damping coefficient. However, use of naturally occurring and unstructured metal does not provide any flexibility in terms of engineering the permittivity and manipulating it at particular frequencies. On the other hand, manipulation of the permittivity is possible at different frequencies using the metamaterial approach. In 1996, Pendry et al.[23] proposed design of dilute metals with a three dimensional lattice of metallic wires (Figure 1.4(a)), which possesses extremely low plasma frequency. The effective dielectric permittivity is demonstrated in Figure 1.4(b).

However, realizing negative permeability has been a challenge because the magnetic field of light couples weakly with materials. That is why the significance of Veselago's work went unnoticed for more than 30 years until Sir John Pendry proposed a practical way to realize a strong magnetic resonance[24] that leads to achieve negative permeability.

A magnetic response can be induced by generating a circulating electric current in a ring shaped structure using an external magnetic field passing along the axis of the ring. But this induced magnetic moment will be weak, until a resonance is introduced into the structure. The split ring resonator (SRR) design provides the opportunity to generate strong artificial magnetism[24]. Each SRR has a gap and in the double SRR geometry (Figure 1.4(c), these gaps are in the opposite directions to each other. The SRR can be modeled as an LC circuit with a natural resonance frequency defined by $\omega_0 = \sqrt{1/LC}$ (L and C are inductance and capacitance, respectively).

A strong circulating electric field can be induced in the SRR by magnetic flux directed along the axis of the SRR in the frequency range centered at ω_0, which results in an effective magnetic moment. The induced magnetic field can be either in or out of phase with the external magnetic field. A strong induced magnetic field can lead to effective negative permeability.

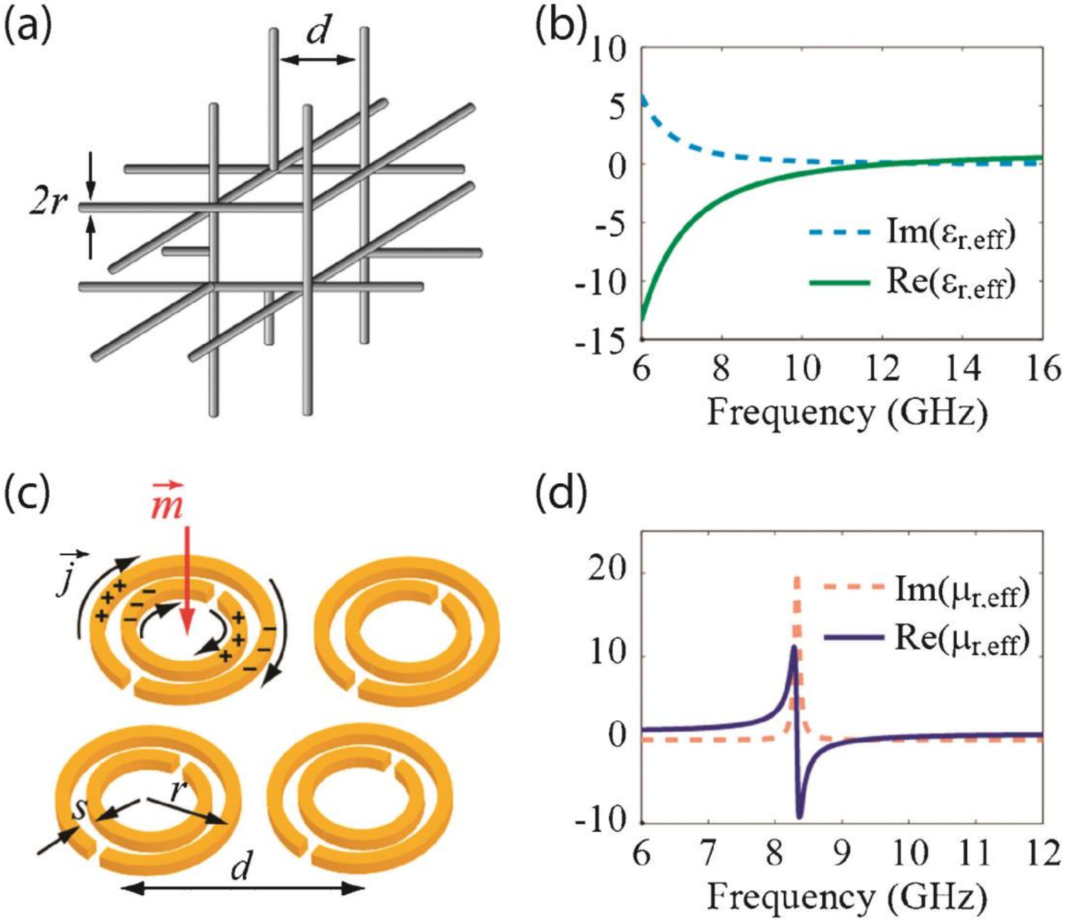

Figure 0.4 (a) Schematic of periodic wires (with radius r) arranged in a simple cubic lattice (with lattice constant d). (b) Effective permittivity of wire media, acting as dilute metals with an extremelylow plasma frequency. (c) Schematic of split ring resonators, with outer radius r and separation s between the two rings. A magnetic field penetrating the resonator induces a current ($\vec{j}$), and thus a magnetic moment ($\vec{m}$). (d) Effective permeability of split ring resonators around the resonance frequency. Adapted from reference [21].

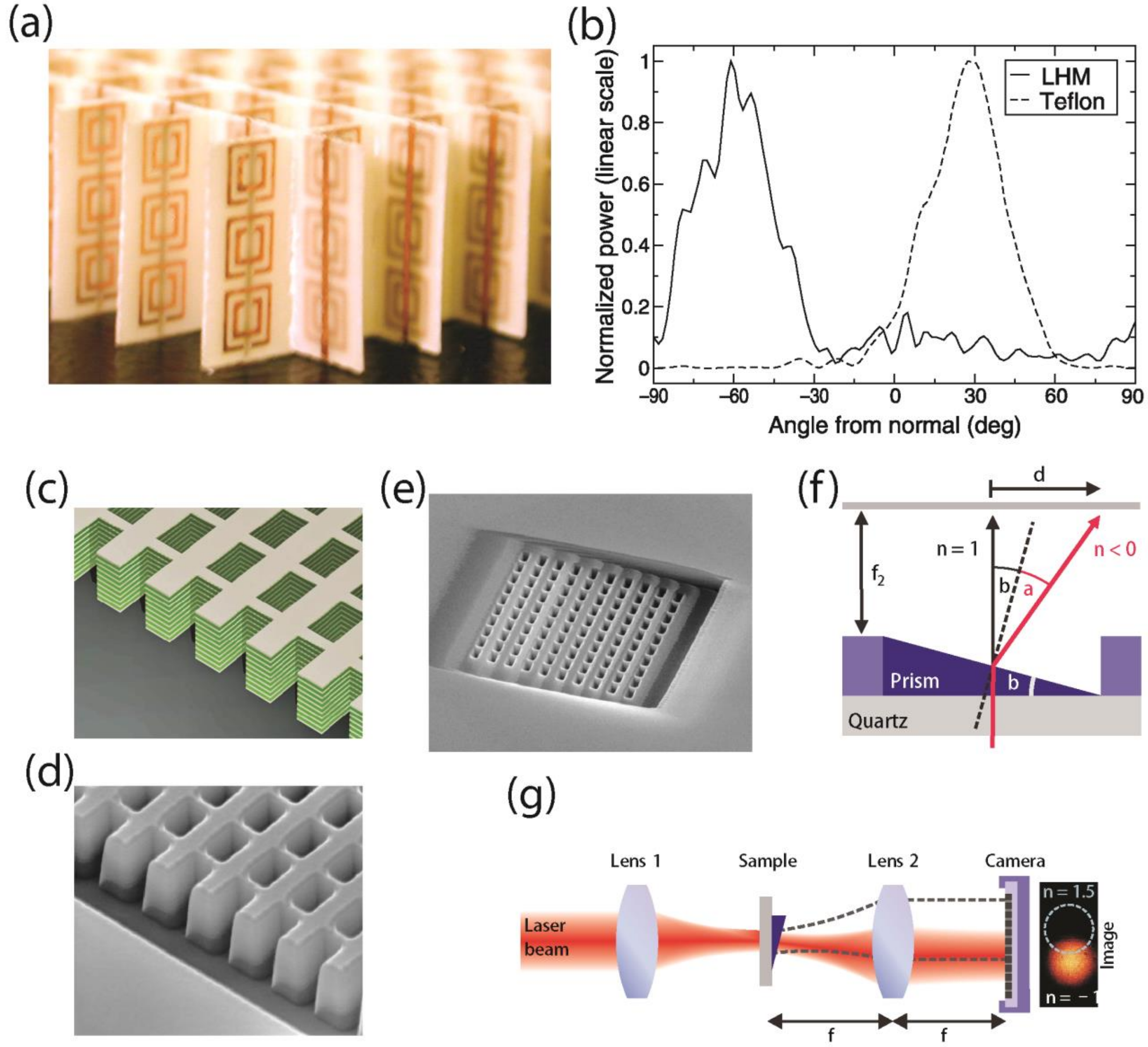

Figure 0.5 (a) Optical image of NIM sample. The NIM sample is made of copper split rings and copper wires. (b) Transmitted power with respect to refraction angle for Teflon (positive index, dashed curve) and NIM sample (solid curve). Adapted from reference [1]. (c) Schematic and (d) SEM image of fishnet metamaterial. (e) SEM of prism of fishnet metamaterials milled using FIB. (f) Ray diagram to demonstrate direction of refracted light coming out a prism with negative index. (g) Fourier imaging to demonstrate bending the light in the other way of normal as expected from a NIM. Adapted from reference[26].

Following Pendry’s work, Smith first experimentally demonstrated the practical realization of a negative index medium [18] using periodic arrays of SRRs and a cut-wires

(Figure 1.5). All these ground breaking studies opened the door to the field of ‘metamaterials’ which has been followed by much work devoted to achieving better design methodologies for negative index metamaterials at telecom (Figure 1.5) and visible frequencies[25]–[27].

1.3 All-Dielectric Metamaterials: Mie Resonance

Since the inception of metamaterials, researchers have strived to scale metamaterials to optical frequencies[20], [28]. However, one of the major limitations in metal-based metamaterials has been the presence of ohmic damping which results in absorption[14]–[16]. Moreover, as the plasmon resonance frequency is approached, the kinetic induction of the electrons in the metal results in saturation of the magnetic response, limiting the use of metal-based metamaterials at high frequencies[17]. In search for an alternative to metallic unit cells, the interaction between electromagnetic waves and high dielectric materials has been investigated by researchers. Exact theoretical solutions of light scattering by small dielectric spherical particles was derived long ago by Lorentz and Mie and the theory is more popularly known as Mie theory (Figure 1.6)[19].

Solutions to Mie theory for dielectric spherical particles yields electric and magnetic multipole resonances characterized by peaks in the scattering coefficients. The lowest order electric and magnetic resonances are the dipole modes. A magnetic dipole resonance is accompanied by a circulating electric displacement current and an electric dipole resonance is accompanied with a circulating magnetic field (Figure 1.7). These electric and magnetic dipole resonances in a dielectric particle form the basis of utilizing them as a meta-atom.

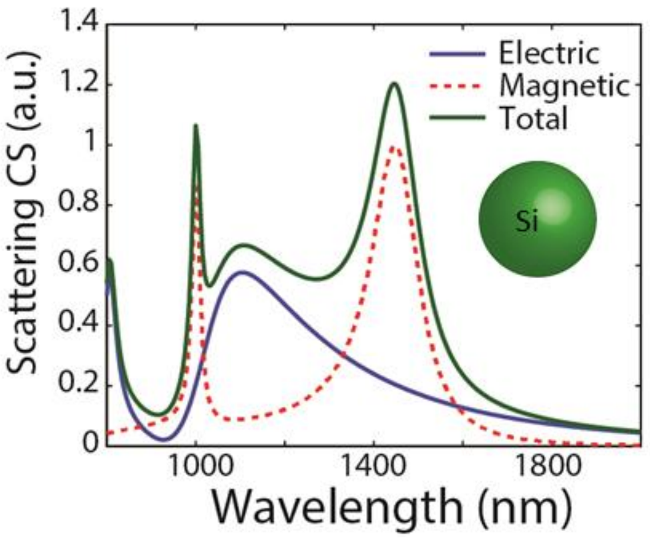

Figure 0.6 Calculation of scattering cross-section of Si sphere based on Mie theory. Plot demonstrates total scattering cross section and contribution of electric and magnetic dipole modes to the total scattering.

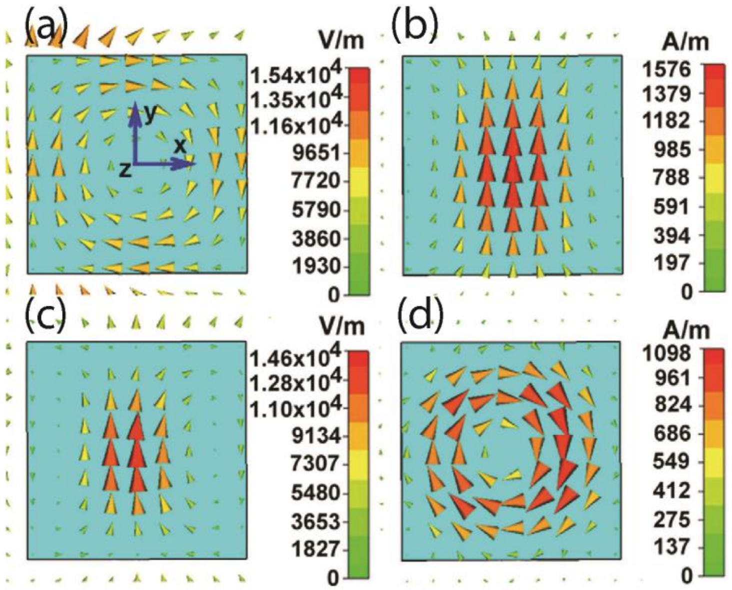

Figure 0.7 Electric and magnetic field distribution in a dielectric cube with the magnetic field polarized along the z axis and electric field polarized along the y axis. (a) Electric field in the plane z=0 near the first Mie resonance. (b) Magnetic field in the plane y=0 near the first Mie resonance. (c) Electric field in the plane z=0 near the second Mie resonance. (d) Magnetic field in the plane y=0 near the second Mie resonance. Adapted from reference [29].

In 1947, Lewin[30] combined the scattering solution from Mie theory with Clausius-Mossotti effective medium theory to calculate the effective permittivity and permeability of a collection of non-interacting magneto-dielectric spheres (Figure 1.8).

$$\frac{3\nu_f}{\frac{F(\theta)+2b_e}{F(\theta)-b_e}-\nu_f}<-1 \tag{1.6}$$

where, *F(θ)* is,

$$\begin{gathered} F(\theta)=\frac{2(\sin\theta-\theta\cos\theta)}{(\theta^2-1)\sin\theta+\theta\cos\theta}, \\ \theta=k_0a\sqrt{\varepsilon'_{r2}\mu'_{r2}}, \\ b_e=\frac{\varepsilon_1}{\varepsilon_2}, \end{gathered} \tag{1.7}$$

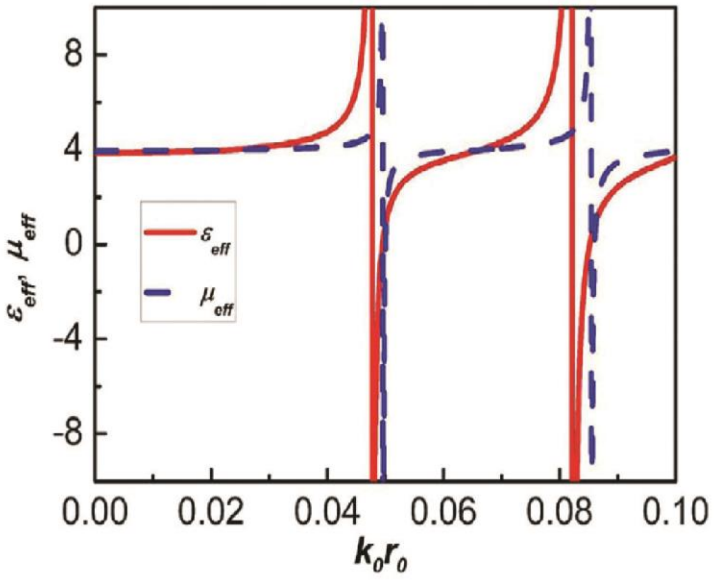

Figure 0.8 Calculation of effective permittivity and permeability based on Lewin’s theory.

It didn’t take long to recognize the implications of Lewin’s work after the inception of the field of metamaterials. In 2002, with a different approach than Lewin’s, O’Brien and Pendry[31] showed that effective negative permeability can be obtained at the magnetic resonance of ferroelectric rods arranged in a two dimensional lattice.

There are several advantages of using dielectric materials over metals as the metamaterial building block. Firstly, dielectric materials experience less optical absorption than metals at high frequencies, e.g. telecommunication and visible ranges. Secondly, dielectric materials do not exhibit magnetic saturation at high frequencies. Thirdly, electric and magnetic Mie resonances are inherent to dielectric particles with simple geometries opposed to more complicated metallic unit cell geometries. The complicated unit cell geometry of metal based metamaterials leads to anisotropic optical properties. Also, because of the complicated geometry of the metallic unit cells, slow and expensive patterning techniques such as electron beam lithography or focused ion beam lithography needs to be used to fabricate metal based metamaterials. This limits the scalability of metal based metamaterials to large areas. However, due to having a simple unit cell geometry, dielectric metamaterials are amenable low cost and high throughput patterning techniques such as self-assembly based nanosphere lithography[32]–[49].

Dielectric metamaterial properties were first experimentally demonstrated in the microwave regime[29], [50]–[54] which allows design of deep sub-wavelength unit cells because of the availability of high dielectric constituents (e.g. $\varepsilon > 100$). Simple unit cell designs e.g spheres[30], [55]–[58], cylinders[29], [31], [59], [60] and cubes[51]–[53], [61] have been used to achieve all-dielectric metamaterials demonstrating high frequency magnetism[51]–[53], [59], [61] and negative refractive index[29], [50], [54].

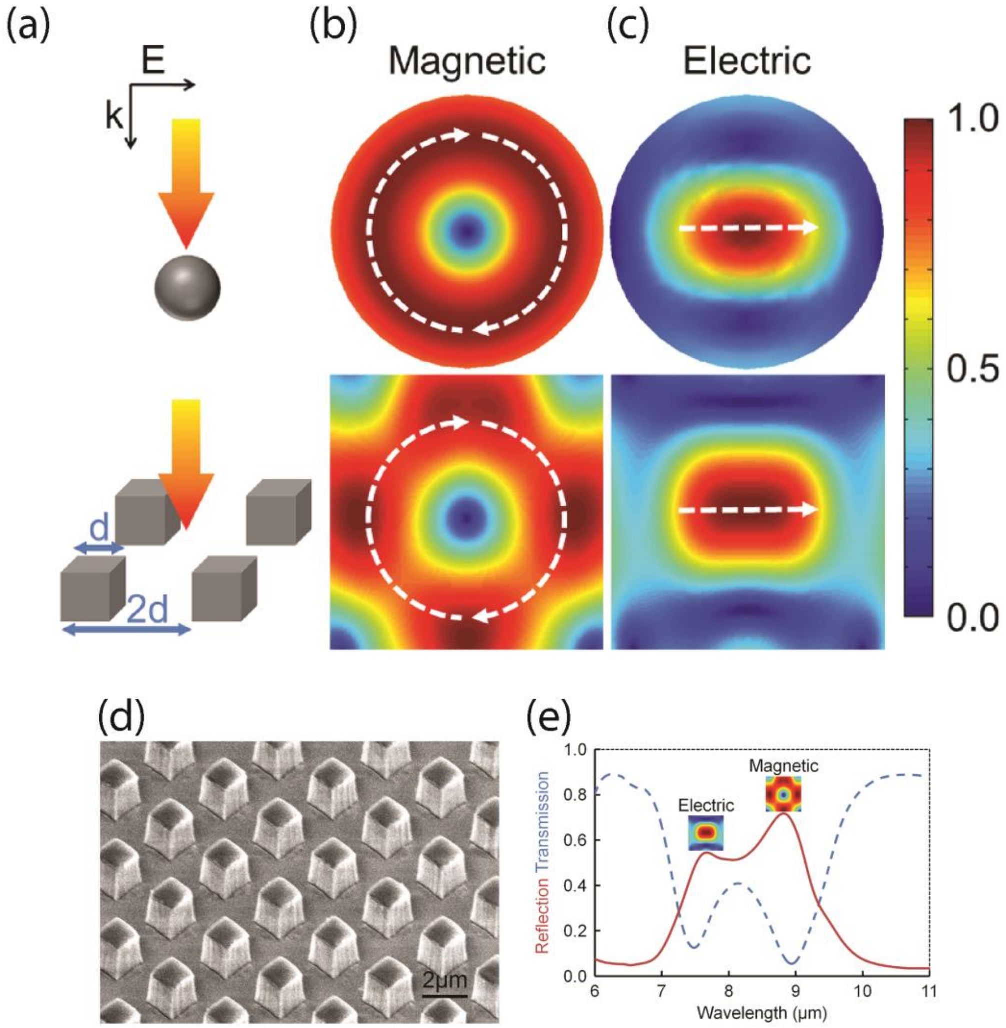

Figure 0.9 (a) Light illumination scheme for an isolated sphere (top) and an array of cube resonators. Electric field profiles at electric and magnetic modes for dielectric (b) sphere and (c) cube. (d) SEM image of Te cube arrays. (e) Experimentally measured transmission and reflection demonstrating distinct resonance corresponding to electric and magnetic modes. Adapted from reference [61].

One of the major challenges that dielectric metamaterials face at optical frequencies (mid infrared, telecommunication and visible range) is that the permittivity of the constituent dielectric materials is greatly reduced compared to that in the microwave regime. This makes it challenging to realize a metamaterial that still falls under the effective medium limit as the unit cell size becomes larger. Hence, search for proper materials is crucial which exhibit moderately high dielectric permittivity at optical frequencies. Telurium (Te) serves as a good choice of dielectric material with moderately high permittivity ($\varepsilon \sim 25$) with low loss at mid infrared regime. Figure 1.9 illustrates realization of strong electric and magnetic dipole resonances in Te cube resonators at mid-infrared frequencies. Silicon (Si) serves as the most suitable dielectric material at telecommunication frequencies because it exhibits moderately high permittivity ($\varepsilon \sim 12$) with low loss. Demonstrations of a magnetic response from metamaterials composed of Si resonators at visible and telecommunication wavelengths along with its amenability to top-down fabrication processes make Si a popular choice for a constituent material. Equipped with the understanding of electric and magnetic scattering behaviors[62], [63] for any arbitrary shape of single dielectric particle[64], manipulation of electric and magnetic responses can be more adequately controlled by engineering the shape of the dielectric particle.

Recently, there has been a tremendous progress in the dielectric metamaterials research at optical frequencies. Some of the important demonstrations includes realization of metasurfaces for controlling the phase of reflected light[65], demonstration of Fano resonances [66] from dielectric oligomers, achieving negative phase propagation with square arrays of dielectric rods[60] (Figure 1.10), realization of Huygens' surface by overlapping electric and magnetic dipole resonances in cylindrical unit cells[67], [68] (Figures 1.11(a,b)), generating electric and magnetic hot-spots between resonator dimers (Figures 1.11(f,g)), achieving super-directive antennae radiation[69], active tuning of resonant modes[70] (Figures 1.11(c-e)), demonstration of magnetic mirror with zero reflection phase[71], demonstration of achromatic lensing[72] and many more. These interesting properties of dielectric metamaterials have drawn the attention of many researchers and provide ample opportunities for further study. In this dissertation, I will demonstrate my earnest attempts to take this field a step forward.

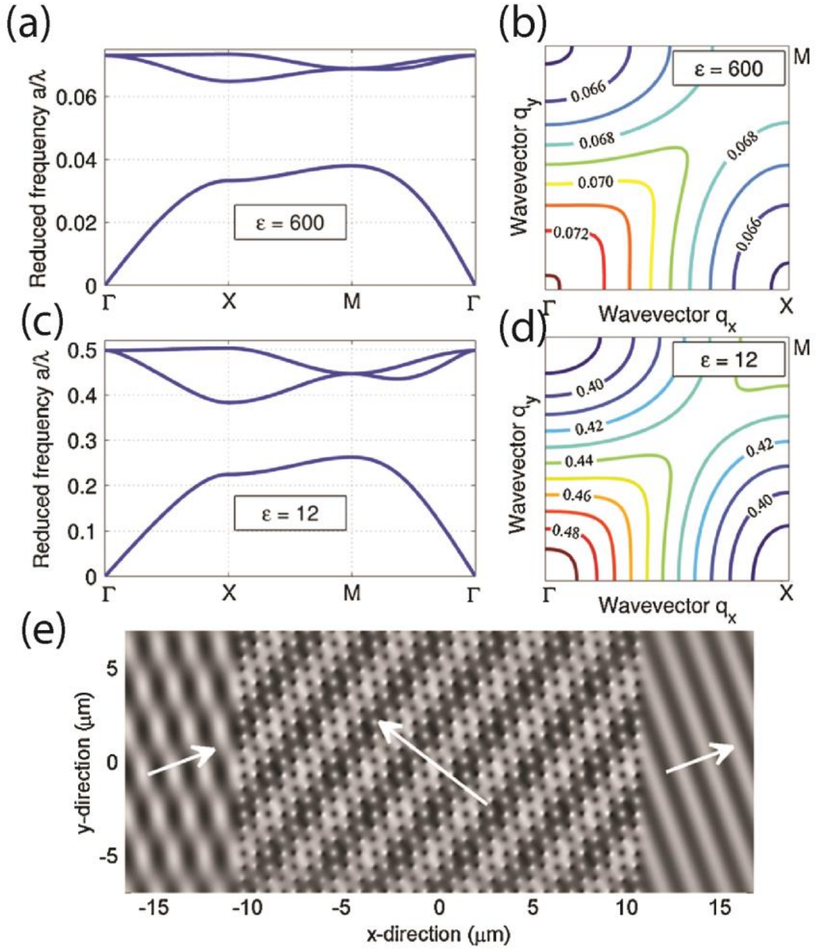

Figure 0.10 Photonic band structures with square rod arrays with (a) ε=600 and (b) ε=12. (c, d) Second-band IFCs of higher and lower ε rod arrays. (e) Electric field profile showing negative phase propagation inside the rod (ε=12) arrays at 1.55 μm wavelength with light incident at 20°. Adapted from reference [60].

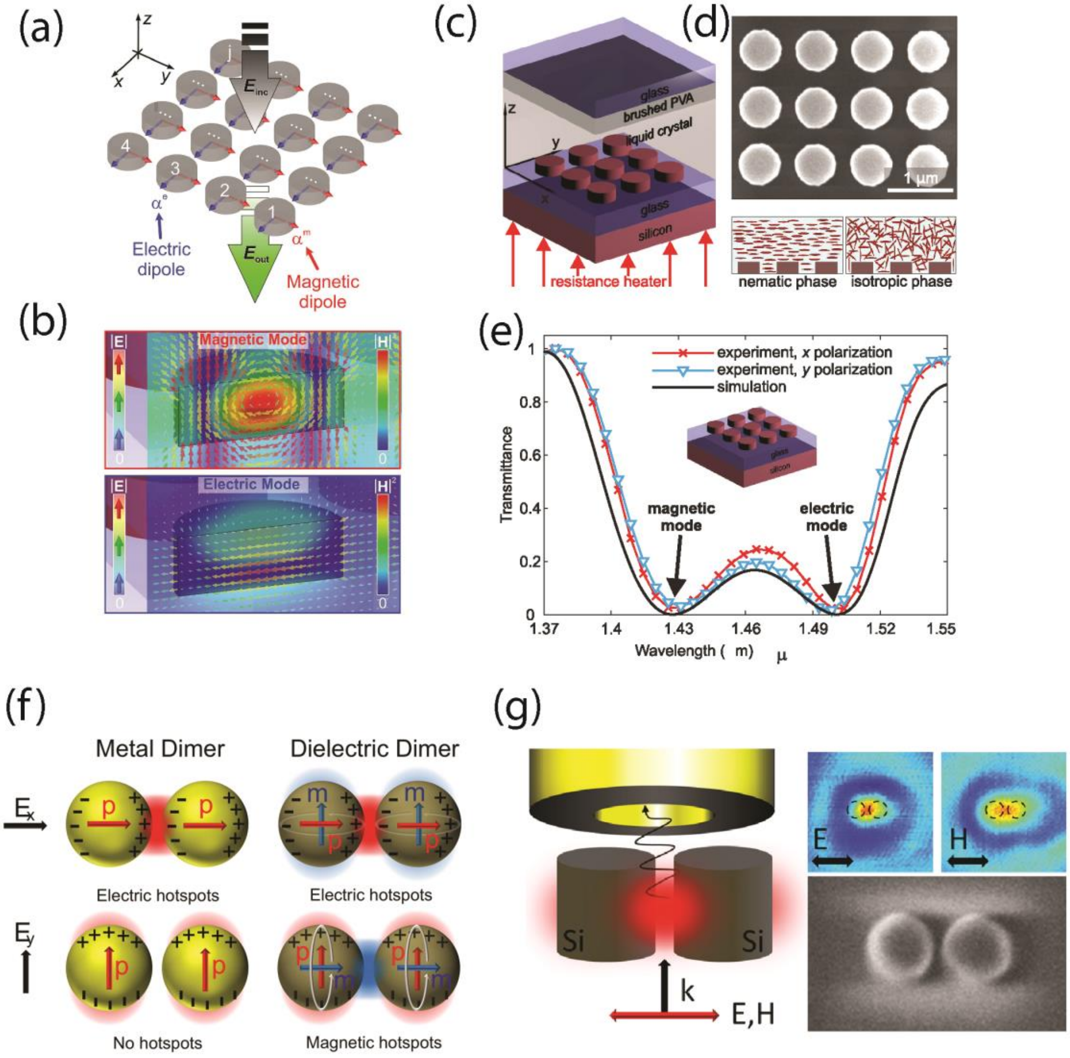

Figure 0.11 (a) Diagram illustrating an infinite array of nanodisks resonators where individual resonators are represented as electric and magnetic dipoles for x-polarized incident light describing a Huygens' metasurface. b) Electric and magnetic field profiles of the magnetic (top) and electric (bottom) mode of a silicon-nanodisk resonator. (c) Schematic of the silicon nanodisk metasurface integrated into an LC cell. (d) SEM image of Si nanodisks arrays (top). Sketch of the (idealized) arrangement of the LC molecules in the nematic and the isotropic phase, respectively (bottom). (f) Comparison between metal and dielectric dimers. (g) Schematic (left) and experimental near field measurement of electromagnetic field enhancement in the gap between Si nano dimers (right top). SEM of nano dimer (right bottom). Adapted from references [68] (a,b); [70] (c,d,e); [73] (f,g).

1.4 Organization of the Document

Chapter 2 will describe the realization of an all-dielectric zero index metamaterial (ZIM) at optical frequencies. The design methodology will be discussed in detail, followed by discussion on the bulk fabrication methodology. Finally realization of the ZIM will be demonstrated by optical experiments.

In Chapter 3, I will discuss the realization of near perfect broadband reflectance from a single layer sub-wavelength-thick all-dielectric metamaterial. The role of the fundamental modes of the single resonator will be discussed in achieving a broad near perfect reflectance band. We will also explore the effect of disorder on the strength of reflectance by randomizing the unit cells in the metamaterial. Finally, we will propose a mechanism to engineer the unit cell to broaden the high reflectance bandwidth.

Chapter 4 will be devoted to demonstration of scalability of dielectric metamaterials to large areas (centimeter sized) using nanosphere lithography, a low cost and high throughput patterning technique. Large scale perfect reflection will be demonstrated over large areas using a single layer of silicon resonators. The effect of disorder on the magnetic and electric dipole resonances will be studied and mechanisms will proposed for overcoming the influence of disorder on reflectance. The possibility of achieving a magnetic mirror at optical frequencies will also be explored.

In Chapter 5, I will discuss the advancement of nanosphere lithography technique to fabricate asymmetric resonators. Here, we propose an advanced large area and high throughput lithography technique which can control the size and orientation of asymmetric patterns spatially. This advanced gradient lithography technique will pave the way towards simple, expedited, and high throughput large scale fabrication of gradient metasurfaces.

In Chapter 6, I will summarize the accomplished work and give a perspective of future work on dielectric metamaterials.

Chapter 2

Impedance-Matched All-Dielectric Optical Zero Index Metamaterial

2.1 Introduction

Epsilon near zero (ENZ) and zero index metamaterials (ZIMs) are a special class of metamaterials which exist at the origin of the parameter space (Figure 1.2, *Chapter* 1). A simple way to realize an ENZ using a metal is to operate at the plasma frequency (ω_p). From the Drude-Lorentz model (Eq. 1.4, *Chapter* 1), the permittivity of a metal at its plasma frequency is zero. Control over realizing ENZ at different frequencies can be achieved by stacking thin layers[74] or by a composite of complementary split ring resonators (SRRs) in host media[6]. Another alternative way to design an ENZ is by utilizing the dispersive properties of metallic waveguides which is operating near cut-off frequency of dominant waveguide mode[75]. The permittivity of the transverse mode of a rectangular metallic waveguide can be given by, $\varepsilon_{eff} / \varepsilon_0 = n^2 - c^2 / (4 f^2 w^2)$, where, *w* is the width of waveguide, *n* is the refractive index, *c* is the speed of light and f is the operating frequency. Hence, the effective permittivity is zero at the waveguide cut-off frequency ($f = c / 2wn$).

ENZs have been experimentally demonstrated in the microwave[6], [76], mid-IR[77], and visible regimes[75]. ENZ metamaterials have a permittivity (ε) near-zero while the permeability (μ) remains unity, resulting in a near-zero refractive index ($n = \sqrt{\mu\varepsilon}$). However, since the permeability remains finite, the relative optical impedance, ($Z = \sqrt{\mu/\varepsilon}$), is grossly mismatched from free-space, which results in large reflections from the ENZ-air interface and limits the functionality of ENZs.

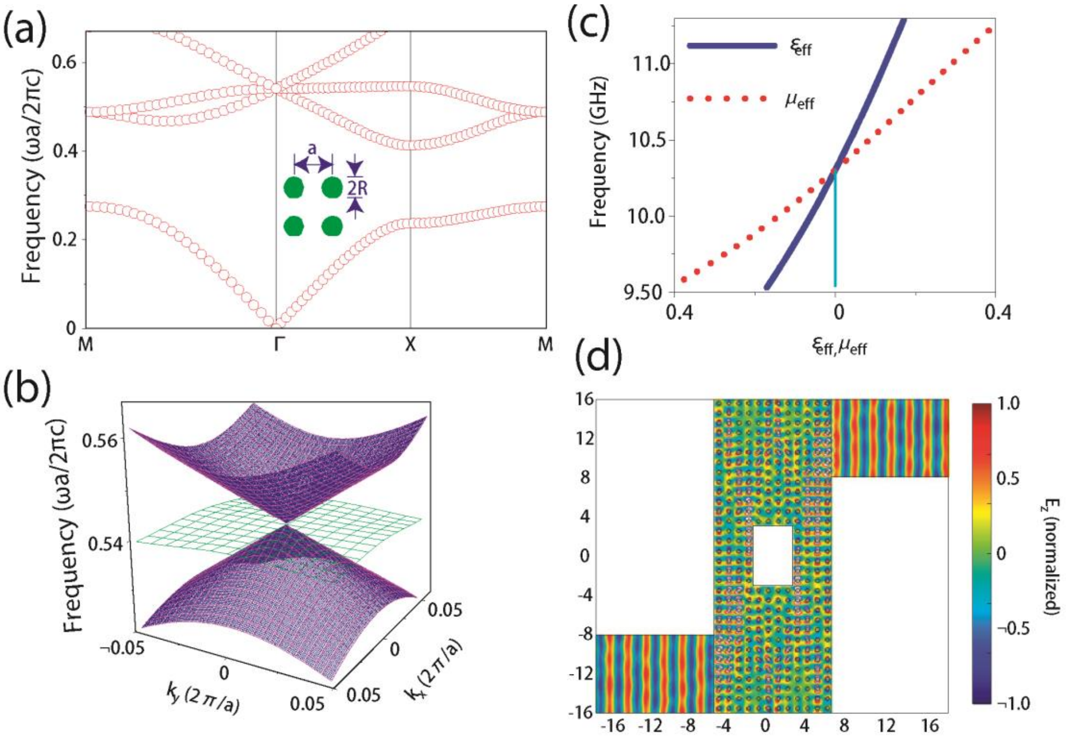

Figure 0.12 (a) and (b) Dirac cone like dispersion in 2D square lattice of circular rods. (c) Retrieved effective parameters showing cross-over at zero at Dirac point demonstrating zero index of refraction. (d) Simulated field profile to demonstrate wave can turn through waveguide bends with a channel composed of ZIM and any obstacle cannot be recognized because the wavelength is infinitely long inside a ZIM. Adapted from reference [78].

The solution to overcome the issue of high reflectance is to design a zero index metamaterial which is impedance matched to air, i.e. both permittivity and permeability are equal to zero. Impedance matched zero refractive index has been demonstrated at optical frequencies with a fishnet geometry[79], however, the metamaterial only functions with normal incidence of light. A more elegant design for an impedance matched ZIM was proposed by Huang et al[78]. In their design the realization of zero refractive index is dictated by designing a periodic structure of infinite rods which forms a Dirac cone like dispersion at the Γ point in the band diagram (Figure 2.1). Prior to this study, Wang et al [80] proposed that a Dirac cone like dispersion can be achieved at the Γ point from a hypothetical homogeneous medium with linear dispersion varying from negative-to-zero-to-positive from lower to higher frequencies. From these studies the correlation between Dirac cone like dispersion and zero index of refraction is substantiated.

The most interesting feature of a ZIM is that the wave-vector inside such a material is zero ($k = 0$), which leads to many other interesting properties. The phase velocity, defined as ω / k, is infinite and the effective wavelength ($\lambda_n = \lambda / n$) inside a ZIM is infinite as well. Hence any object inside a ZIM will practically be cloaked because an object will not scatter light if its size is infinitely smaller than the wavelength of light illuminating it. Another interesting feature is that a ZIM only transmits light normal to the interface. This follows directly from Snell's law,

$$n_1 \sin\theta_1 = n_2 \sin\theta_2 \qquad 2.1$$

where, n_1 and n_2 are the refractive indices of two different media (medium 1 and 2) and light is incident from medium 1 to medium 2 at an angle θ_1 and refracts in medium 2 with an angle of θ_2. Now, let us consider n_2=0. To satisfy Snell's law, θ_1 has to be 90°. This can also be explained by comparing the isofrequency contours (IFCs) of a ZIM and air at the interface. In Figure 2.2, the small circle (red), corresponding to an IFC of the ZIM, has a radius $k_{ZIM} = k_0 n_{ZIM}$ which is proportional to the effective index of the metamaterial and the larger circle (black) has a radius proportional to the index of air ($n_{Air} = 1$). In order to conserve angular momentum at the ZIM-air interface light can only leave ZIM surface at an angle ($\theta_{\max}$) very close to normal to the interface. This also explains the directional emission behavior of emitters embedded inside a ZIM[76].

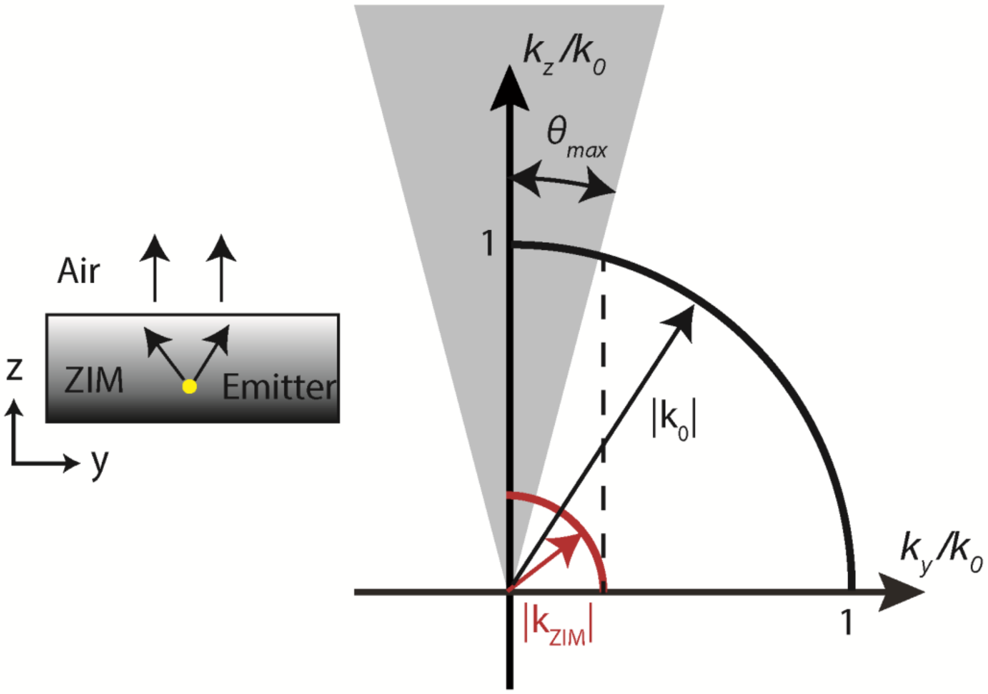

Figure 0.13 Schematic illustrating directional emission from emitters from inside a ZIM.

This chapter illustrates the first experimental realization of zero index metamaterials (ZIM) at optical frequencies with all dielectric constituents[81]. Although, impedance matched zero refractive index has been demonstrated at optical frequencies with a fishnet geometry[79], the metamaterial was restricted only to normal incidence of light. These issues have been overcome by utilizing resonant all-dielectric metamaterial with high refractive index. Here, we designed the ZIM at optical frequencies with periodic Si rod unit cells under TM polarization of light. The simple geometry of the dielectric resonators along with advancements in the top-down nano-fabrication technologies provided the possibilities of fabrication of 3D ZIMs.

2.2 Design Methodology

The ZIM design started with calculating the band structure of an infinitely periodic square lattice of Si rods. When properly designed, this structure can exhibit a Dirac cone at the Γ point in the band structure[78], a feature that is similar to the electronic band structure in graphene[82]. At the Dirac point, the metamaterial exhibits zero effective permittivity and permeability, resulting in an impedance matched ZIM[78]. From fabrication stand point, we designed the metamaterial with stack of square cross-section Si rods embedded in SiO_2. The band structure corresponding to the bulk ZIM (infinitely thick), with w = t = 260 nm and a = 600 nm, is shown in Figure 2.3(a). The band structure is computed for TM polarization with the electric field oriented along the rod axis and the Dirac cone like dispersion can be observed at the center of Brillouin zone where two transverse bands with linear dispersion intersect a flat quasi-longitudinal band, resulting in triple degeneracy. We utilized field-averaging of the Bloch modes[83] to retrieve the metamaterial's effective bulk optical properties (Figure 2.3(b)) and simultaneous zero-permittivity and permeability are obtained at the triple degeneracy frequency of 211 THz (λ_0=1422 nm). This response is directly attributable to a linear combination of electric monopole and magnetic dipole Mie resonances within the Si rods (inset of Figure 2.3(b)), allowing the effective constitutive parameters to be accurately extracted using effective medium theory[84]. This was confirmed by the excellent agreement between the extracted propagation vector, acquired using field averaging, and the computed band structure around the triple degeneracy point (Appendix A.2). A relatively broadband impedance matched low-index region is present around the zero-index point and over the frequency range from 215 THz to 225 THz there exists only one propagating band, TM4, which allows us to define an effective index of refraction for the structure for off-normal angles of incidence. The iso-frequency contours (IFCs) over this frequency range are shown in Figure 2.3(c) and it can be observed that they maintain a nearly circular shape indicating that the material maintains a relatively isotropic low-index response for TM-polarized light over this bandwidth. This all-angle response is critical for preserving the unique physics associated with low- or zero-index materials such as directionally selective transmission and emission from within the material. It should be noted that in a perfectly homogeneous zero-index metamaterial, the flat longitudinal band is not accessible with TM-polarized light. However, due to finite spatial dispersion, this band becomes quasi-longitudinal in our case and is accessible at off-normal angles of incidence. As can be seen from Figure 2.3(a), the band bends down and thus prevents single mode propagation for off-normal incidence at frequencies at and below the Dirac point (extended states of the crystal are provided in the Appendix A.2). In this frequency region, a refractive index cannot be assigned for off-normal incidence and directionally selective transmission is not preserved.

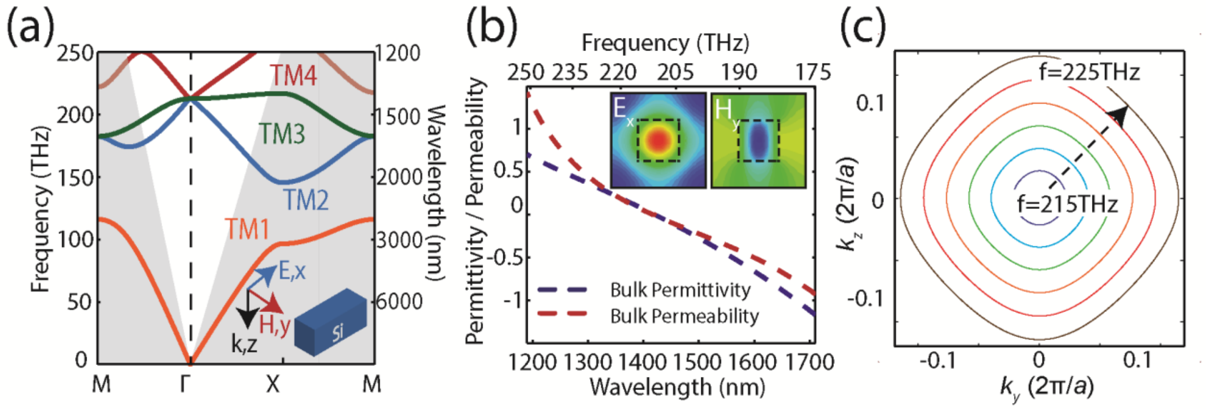

Figure 0.14 (a) Band diagram of uniform bulk ZIM (infinitely thick) for TM polarization. Dirac cone dispersion is observed at the Γ point with triple degeneracy at 211 THz. The shaded area denotes regions outside the free-space light line. (b) Retrieved effective permittivity and permeability of the bulk ZIM acquired using field-averaging. The inset shows the electric and magnetic fields within a single unit cell at the zero-index frequency indicating a strong electric monopole and magnetic dipole response. (c) IFC of the TM4 band. The contours are nearly circular (i.e., isotropic) for a broad frequency range and increase in size away from the zero-index frequency indicating a progressively larger refractive index.

One of the consequences of a low or zero-index is that light will not be guided using a conventional slab waveguide, in other words Dirac point appears in the light cone, and thus the metamaterial must be designed for free-space access. Hence, the simulated 2D periodic infinite rod structure needs to be designed as a 3D structure with periodicity along y and z direction, with orientation of the rods along x. Along z direction which is the normal direction to the plane of substrate, keeping in mind the fabrication convenience, number of unit cells needs to be minimum. We optimized the number of unit cells as 5 based on the convergence of the zero index response to the infinite periodic structure. In Fig, we show the electric and magnetic field profiles at a frequency that is slightly above the zero-index frequency, where both the index of refraction and magnitude of the wavevector are close to zero. This leads to negligible spatial phase change across the length of the ZIM ($\varphi = kL$), where L is total thickness of the ZIM structure. In the field plots (Figure 2.4), it is clear that the transmitted light leaves the ZIM / air interface with the same phase as the incident plane wave. The unit cells also show strong electric and magnetic resonances, which are resonating in-phase, a characteristics that can be attributed to infinite phase velocity leading to zero phase lag between the resonators.

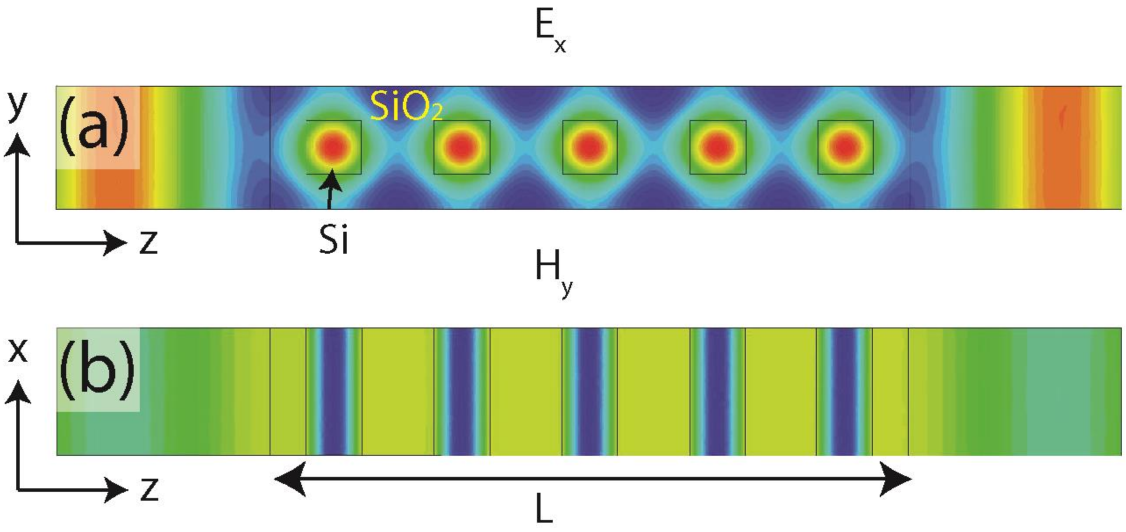

Figure 0.15 Electric and magnetic field plots demonstrating no spatial phase change of light across the ZIM. All the Si resonators are resonating in phase because of infinite phase velocity inside the ZIM.

2.3 Fabrication of Multilayer ZIM

The overall fabrication process flow is described in Figures 2.5 (a-f). To realize a free-space accessible ZIM, fabrication began with deposition of multilayer stack of 11 alternating layers of α-Si (ε=13.7, 260 nm thick) and SiO_2 (ε=2.25, 340 nm thick) (Figure 2.6 (a)) using low pressure chemical vapor deposition with a single process run on a 4 inch quartz wafer. The LPCVD tool used was a horizontal tube furnace. A quartz caged boat was used to contain the wafer to improve cross wafer uniformity. Deposition temperature was 550°C and process pressure was 300 mTorr and both were held constant throughout the deposition of both films. Process gases were introduced into the tube furnace via mass flow controllers. The α-Si layer was deposited by flowing 50 sccm's of 100% SiH_4. The SiO_2 layer was deposited by flowing 85 sccm's of SiH_4 and 120 sccm's of O_2. A brief N_2 purge was introduced between layers. This alternating process was repeated until the desired number of layers was deposited.

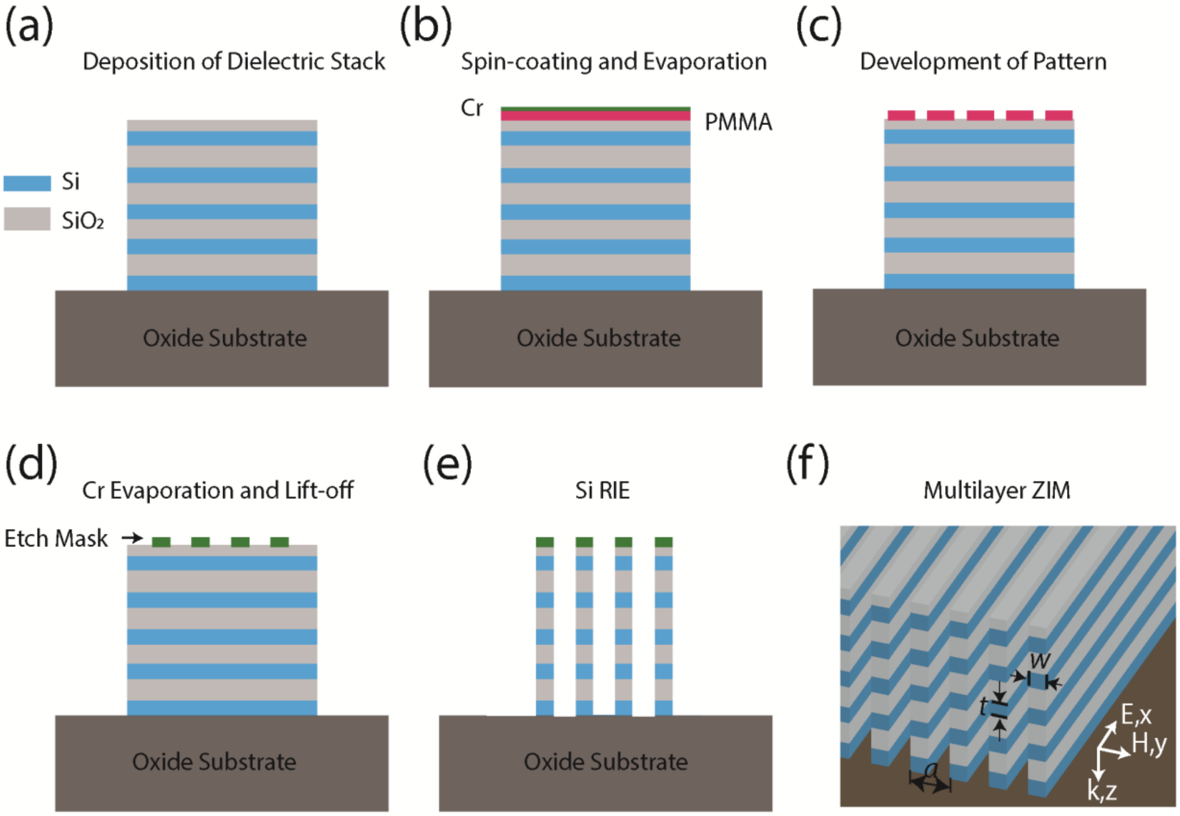

Figure 0.16 Schematic of process flow to fabricate multilayer ZIM

A hard metal etch mask was patterned using electron beam lithography (Raith and/or Jeol) and deposition of 50 nm chromium (Cr) followed by lift-off. To avoid surface charging detrimental effects, electron beam sensitive resist (PMMA) was coated with a 10 nm Cr charge dissipation layer to be chemically removed prior to the exposed resist development. A fluorine based reactive ion etching (RIE) recipe was developed in an Oxford Plasma Lab tool to etch the multilayer sample by alternating the recipe for the Si and SiO_2 layers. The final structure has a 10:1 aspect ratio with respect to the total height and gap width between the rods. The base etch recipe involved 100 W RF power, 2000 W ICP power with C_4F_8 and O_2 gas flows for the SiO_2 layers and 80 W RF, 1200 W ICP with C_4F_8, SF_6, O_2 and Ar gas flows for the α-Si layers. The oxide had a positive slope as we etched down to subsequent layers underneath. Starting with the base recipe for the upper layers, the subsequent SiO_2 layers were etched more aggressively with increasing depth. This was accomplished by changing the ratio of C_4F_8 and O_2 gas-flow which provided less passivation to the side walls during etching. The base Si etch recipe resulted in straight side walls until we reached the bottom most layer. The bottom most oxide and Si layers were etched with the most aggressive recipes and the top layers were protected by additional passivation steps. The metamaterial's internal structure was characterized by imaging the edge profile after milling cross-sections inside the array using focused ion beam milling (FIB). During all imaging, a thin layer of Cr was deposited on the sample to provide a conducting surface. A total of 5 functional layers (Si / SiO_2 pairs) results in a metamaterial with a thickness of 3 μm, about twice the free-space wavelength at the zero-index point (Figure 2.6 (b)).

We made sure that PMMA, which was spin-coated on the sample after the RIE process, filled in the gaps completely in order to provide a background with the same permittivity as the SiO_2 spacer layers. The sample with a drop casted PMMA film was placed in an evacuated desiccator to remove air bubbles and this process was followed by spinning and soft baking (120 degrees for 2 minutes) twice and reflowing at 300˚ C for 2 minutes to reach the desired thickness. The final structure was cross-sectioned with FIB milling at multiple locations to confirm the complete filling (Figure 2.6 (c)).

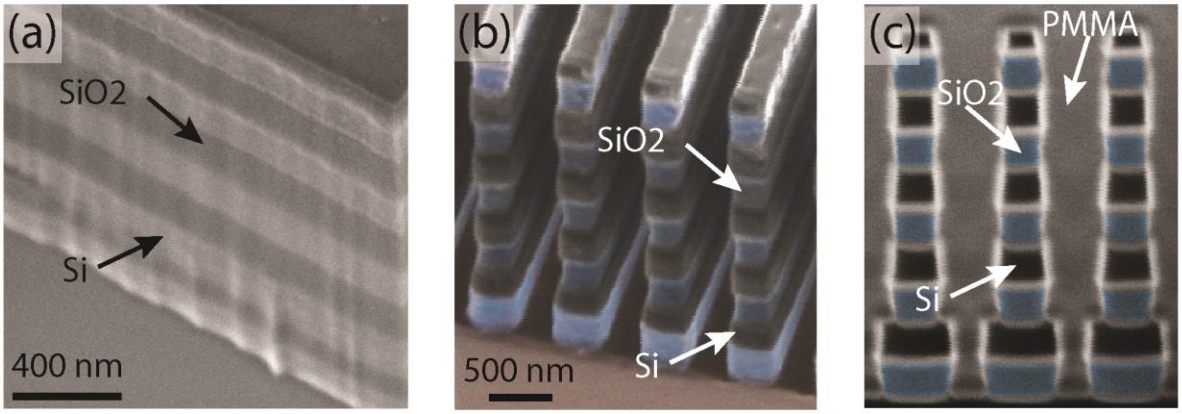

Figure 0.17 (a) SEM image of multilayer stack of Si and SiO2. (b) FIB image (isometric view) of ZIM (before PMMA filling). (c) Cross-sectional FIB showing complete filling of PMMA inside the gap regions.

2.4 Influence of Non-Uniformity

The fabricated metamaterial has both a finite thickness as well as non-uniform rod sizes and will thus deviate somewhat from the bulk parameters. To better understand the optical response of the fabricated metamaterial, full-wave finite-difference time-domain (FDTD) simulations were assigned with optical properties for arbitrary angles of incidence due to presence of the quasi-longitudinal band which is accessible at large incident angles.

In order to gauge the agreement with the simulated material properties, transmittance of the fabricated ZIM was acquired by illuminating the sample with normal-incident white light with the electric field oriented along the Si rod axis (Figure 2.7(c)). The simulated and measured transmittance show good agreement in spectral shape, though the experimentally obtained curve has a lower amplitude that is likely due to non-uniformity in rod width at the edges of the sample as well as surface roughness. The measured spectrum shows a peak transmission of 80% at 1405 nm, the spectral position corresponding to the impedance-matched low-index point. A dip in transmission also occurs at 1460 nm, corresponding to the metallic region of the sample.

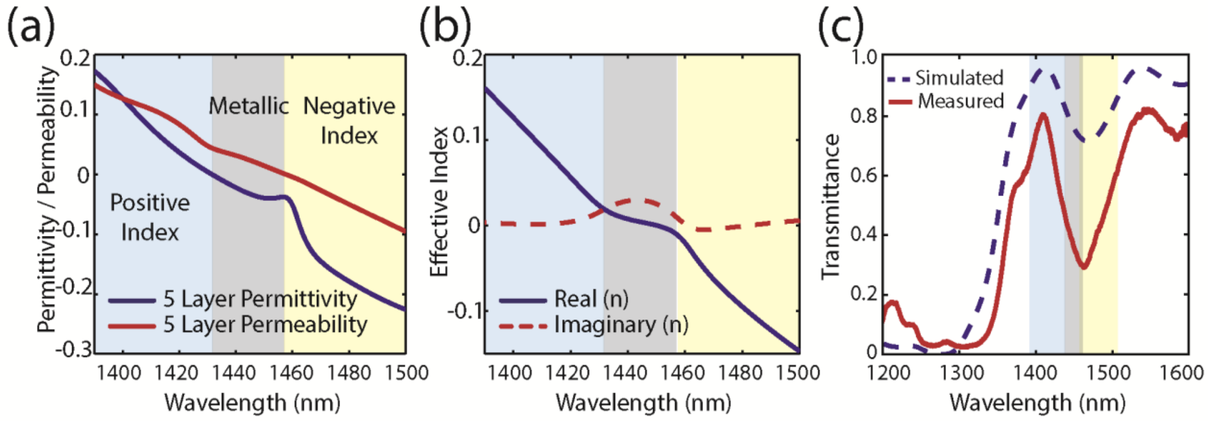

Figure 0.18 (a) Effective permittivity and permeability of the fabricated ZIM obtained using S-parameter retrieval. Regions corresponding positive index, metallic properties, and negative index are denoted with blue, grey, and yellow shading, respectively. (b) Effective refractive index of the fabricated structured obtained using S-parameter retrieval. (c) Experimental (red) and theoretical transmittance (dotted blue) curves of the ZIM (200 x 200 μm^2 total pattern area).

2.5 Experimental Characterization of the ZIM

One of the most fascinating properties of isotropic low-index materials is that light incident from free-space is only transmitted over a narrow range of incidence angles. This effect is a direct consequence of phase matching at the interface which requires that the wave vector along the interface be conserved. As illustrated with the IFCs depicted in Figure 2.8(a), in a low-index metamaterial, the wavevector is restricted to extremely small values causing light incident at high angles ($k_{y,0} > |k_{ZIM}|$) to be reflected while near-normal incident light is transmitted ($k_{y,0} < |k_{ZIM}|$). This effect is evident when examining the simulated transmittance with regard to wavelength and angle of incidence (Figure 2.8(b)) for the fabricated ZIM. The material exhibits near-zero transmission at off-normal incident angle within the positive index band centered at 1400 nm, with improving angular confinement in transmission as we approach the zero-index point. The presence of the quasi-longitudinal band within the negative index region (λ_0~1475 nm) is also apparent, allowing transmission at large incident angles.

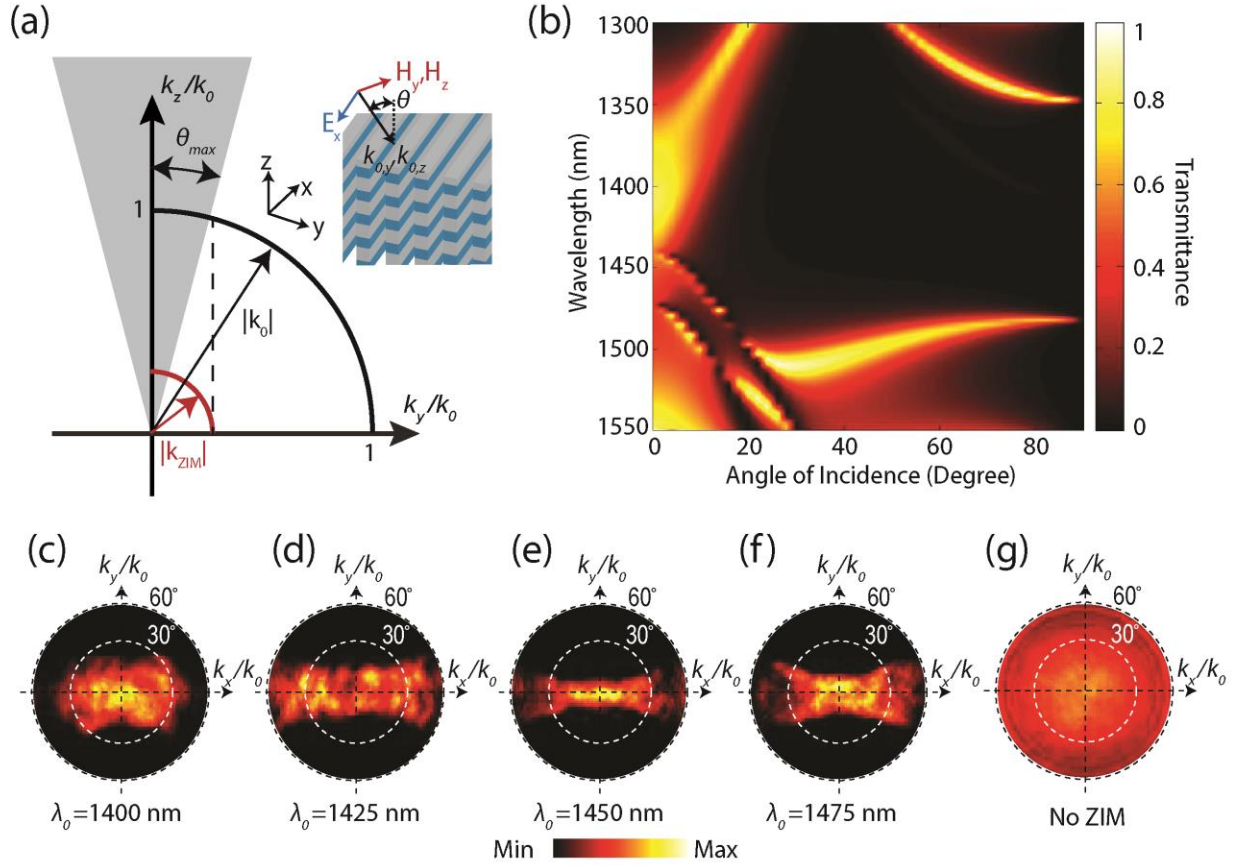

Figure 0.19 (a) IFCs of air and a low-index metamaterial illustrating angularly selective transmission due to conservation of the wave vector parallel to the surface. (b) Simulated angle and wavelength-dependent transmittance of the fabricated structure. (c-f) Fourier-plane images of a beam passing through the fabricated ZIM structure within the low index band. Angularly selective transmission can be observed in the *y*-direction due to the low effective index. Along the *x*-direction, angular selectivity is not preserved due to the one-dimensional nature of Si rods. (g) Fourier-plane image of the illumination beam demonstrating uniform intensity over the angular range measured.

To experimentally verify that the fabricated ZIM preserves these features, light transmitted through the sample was imaged in the Fourier plane. Illumination was provided by a femtosecond synchronously pumped optical parametric oscillator (Coherent, MIRA OPO) that was focused with a large numerical aperture objective (NA=0.85), providing incident angles up to 58.2°. The acquired Fourier images (Figures 2.8(c-g)) show confinement of light along the *y*-

axis of the material which is in the direction of in-plane periodicity. Within the low index region between 1400 nm and 1475 nm, tighter confinement of k_y is observed with progressive lowering of the refractive index, in agreement with the simulated data. Confinement is absent in the x-direction due to the fact that the electric field is no longer directly along the rod axis for these incident angles. The directional filtering of transmission demonstrates that a nearly isotropic low-index for TM-polarized light is indeed preserved within the fabricated metamaterial.

An additional consequence of the near-zero spatial phase change is that incoherent isotropic emitters placed within the ZIM will tend to emit coherently in the direction normal to the air / ZIM interface[5], [76], [85]. To demonstrate this effect, we first simulated the emission from a line source placed both in the center of the material as well as sources distributed throughout the volume of the material, emitting at a free-space wavelength of λ_0=1425 nm (Figure 2.8(b)) Both emission profiles are confined to an overall angular spread of 10° and are not sensitive to the position of the emitter. The two small side lobes at -60° and 60° are due to scattering from the corners of the metamaterial, an effect associated with having a material with finite area. For experimental demonstrations, we placed lead sulfide (PbS) semiconductor quantum dots (QDs) within the ZIM to act as the emitter. The QDs had a luminescence peak centered at 1420 nm and a full width at half maximum of 172 nm. The QDs were sandwiched between two PMMA layers within the ZIM, and were excited with a tightly focused 1064 nm laser beam (Figure 2.9).

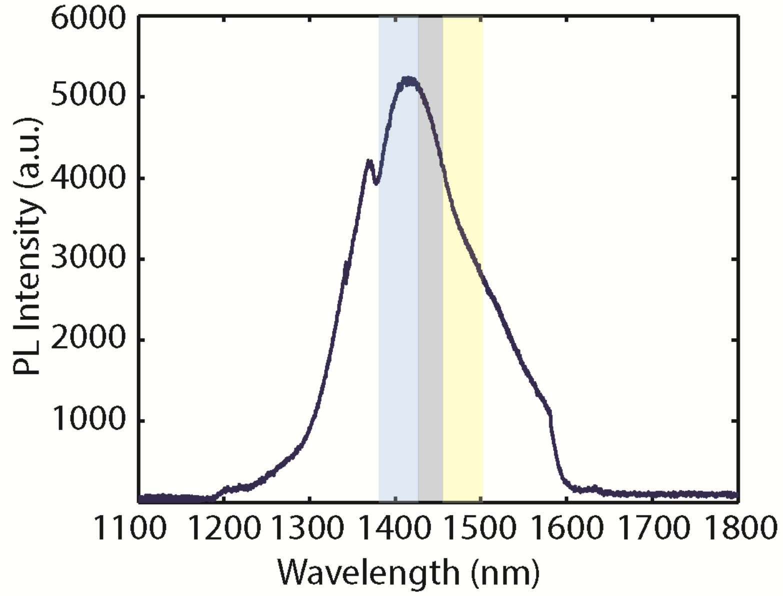

Figure 0.20 QD Emission Spectrum. Photoluminescence (PL) spectrum of PbS quantum dots (Evident Technology) used in the main text. The emission peak appears at 1425 nm, with a full-width at half-maximum of 172 nm. The blue-, gray- and yellow-shaded region corresponds to positive index, metallic properties, and negative index as acquired from S-parameter retrieval. The dip of measured luminescence spectrum at around 1380 nm is due to the water absorption line.

The Fourier-plane images (Figures 2.10(c-f)) from both an unstructured PMMA/QD film and QDs placed within the metamaterial show good angular confinement in the *y*-direction and an over two-fold increase in intensity emitted normal to the interface from the ZIM compared to the unstructured case. The increase in emission normal to the interface is a result of the uniform phase distribution within the ZIM, leading to constructive interference from emitters throughout the material[75], further supporting the realization of a near-zero refractive index. The constructive interference of multiple emitters is in competition with the reduced optical density of states associated with the low-index response. For instance, if the number of emitters is reduced to one, the emitted power in air will be greater than the ZIM in all directions. However, as expected for constructive interference within the material, the far-field intensity of waves propagating normal to the interface is proportional to the number of emitters squared. We also note that although the luminescence peak of the QDs matches the low-index band of fabricated ZIM structure quite closely, parts of the emission fall beyond the low-index band, resulting in slightly lower angular confinement compared with the transmission data.

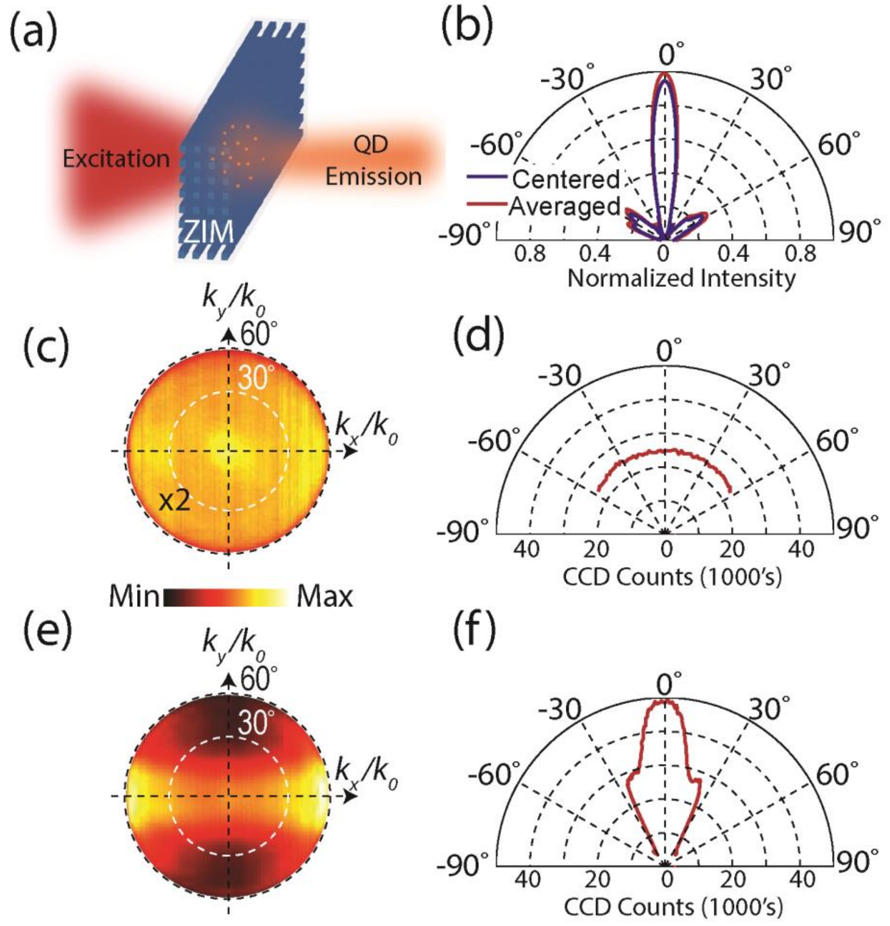

Figure 0.21 (a) Schematic of laser-pumped QD emission from within the ZIM structure. (b) Calculated emission profile for a line source placed in the center of the material (centered) and the average profile from line sources placed throughout the material (averaged). (c) 2D Fourier-plane images of quantum dot emission on the substrate, intensity is scaled by two times. (d) A cross-section of the emission taken at $k_x = 0$. (e) 2D Fourier-plane images of QD emission within the ZIM, respectively, showing enhanced rate and directivity of spontaneous emission. (f) A cross-section of the emission taken at $k_x = 0$.

2.6 Conclusion

Here we developed a mechanism to experimentally realize an impedance matched and lossless isotropic zero index metamaterial, consisting of all dielectric rod unit cells, at optical frequencies for a particular polarization (TM) of light. We exploited the electric and magnetic Mie resonances in single dielectric resonator and designed the ZIM with periodic square lattice of collection of such resonators, exhibiting simultaneous zero effective permittivity and permeability. The experimental demonstration of angular selectivity of transmission and spontaneous emission illustrates the practical realization of isotropic ZIM for TM polarized light. The realization of impedance matched ZIMs at optical frequencies opens new avenues towards the development of angularly selective optical filters, directional light sources, and large area single mode photonic devices. The advent of all-dielectric optical metamaterials provides a new route to developing novel optical metamaterials with both low absorption loss and isotropic optical properties. Proper understanding of controlling electric and magnetic Mie resonances opens the door to other applications such as perfect reflection using single layer all-dielectric metamaterial structures, which we will explore in the next chapter.

Chapter 3

Mie Resonance Based All-Dielectric Metamaterial Perfect Reflectors

3.1 Introduction

In this chapter, we exploit the electric and magnetic Mie dipole resonances of silicon (Si) cylinder resonators to design a single negative metamaterial with polarization independent near-perfect broadband reflection within the telecommunication band. The study is also extended to disordered metamaterials which demonstrates that near-unity reflection can be preserved by avoiding interactions between resonators. We also explore the opportunities for broadening the reflectance bandwidth by utilizing higher order resonances along with the fundamental resonances. This has been achieved by manipulating the resonances with more complex resonator design.

Perfect dielectric reflectors are important photonic elements due to their ability to handle high power irradiation. Although gold (Au) and silver (Ag) mirrors exhibit high reflection (~98 %) in the telecommunication band, they are not suitable for high-power applications due to their absorption (~2 %). In place of metallic mirrors, distributed Bragg reflectors (DBRs), made of alternating dielectric layers, are typically used for achieving near-perfect reflection. The primary disadvantage of Bragg reflectors is that the deposition of multiple dielectric materials is a lengthy process which adds to the cost of the product. Realization of perfect reflection from a single-layer disorder metamaterial offers advantages in terms of possibilities of simple, high-throughput, and low-cost fabrication, and in turn opens the door to future paint-like coatings of metamaterials for even larger-area implementation.

3.2 Design Methodology

We start with a discussion on the conditions required to achieve perfect reflection[86]. For a semi-infinite medium, it can be shown that the reflectance is unity when the real part of the impedance of the medium is zero. This condition is achieved when $\varepsilon' / \mu' < 0$ and $\varepsilon''\mu' = \varepsilon'\mu''$, where the complex permittivity and permeability are given by $\varepsilon' + i\varepsilon''$ and $\mu' + i\mu''$, respectively. The first condition requires that the real parts of the permittivity and permeability have opposite signs, which is readily met in the vicinity of an electric or magnetic resonance, provided that the resonances are spectrally isolated. While the second condition is more restrictive, it is readily satisfied in lossless materials. To achieve near-unity reflection with a finite thickness slab, the condition on the impedance is unchanged, but the imaginary part of the index (n'') must also be maximized to prevent evanescent tunneling across the slab.

With this analysis as a guideline, we can begin to design perfect reflecting MMs using the Mie resonances in dielectric particles. In the work presented here, we utilize the cylinder resonator geometry due to its amenability with top-down fabrication techniques. For a cylinder resonator, the positions of the magnetic and electric dipole modes are a function of the aspect ratio (AR), defined as $\mathrm{AR} = H / D$ where H is the height of the cylinder and D is the diameter. To demonstrate this dependence, scattering cross-sections for a single Si (ε = 12) cylinder resonator embedded in air are plotted in Figure 3.1(a) for two different ARs (1.25 and 0.6), where the maxima in electric and magnetic cross sections indicates the positions of the electric and magnetic modes, respectively. The electric and magnetic contribution to the scattering cross sections, with incident light polarization defined by E_x and H_y, were determined by plotting the far-field scattering cross-sections at the θ = 90° plane with φ = 90° and 0°[87], [88], where θ and φ are schematically illustrated in Figure 3.1(b). Polar plot of far-field scattering cross-sections at the θ = 90° plane (Figure 3.1(c)) confirms the excitation of electric and magnetic dipole modes. The electric dipole scattering amplitude is multiplied by 1.78 so that its amplitude matches that of the magnetic mode. The excitation of dipolar modes are further corroborated in Figure 3.1(d) which illustrates the electric and magnetic dipole field profiles at their respective resonance positions.

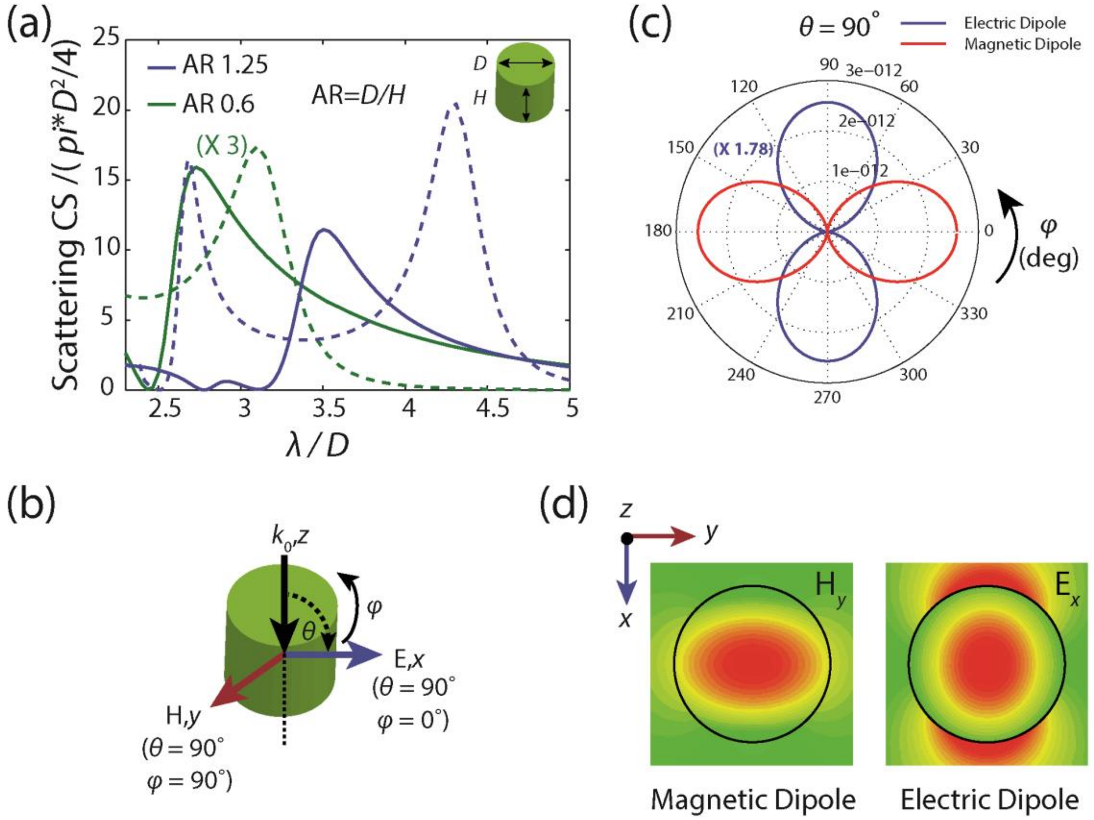

Figure 0.22 (a) Scattering cross-sections of single Si (ε = 12) cylinder resonators embedded in an air background for two different aspect ratios (AR = 1.25 and AR = 0.6). Solid and dashed lines represent the electric and magnetic contributions to the scattering cross-section, respectively. (b) Diagram showing incident plane wave polarization and the azimuthal angles of polar coordinates for scattering cross section calculation (c) Polar plot of electric and magnetic contribution to scattering cross sections (m^2) at the respective Mie modes at θ = 90° plane with φ varying from 0° to 360°. (d) Magnetic and electric field profiles at the center of single disk resonator at respective dipole modes.

To illustrate the spectral separation of electric and magnetic modes across a larger domain, the corresponding mode positions are plotted against the AR in Figure 3.2(a). At low ARs we find that the electric mode is the first resonance and increasing the AR results in a mode crossing. Further increasing the AR results in spectral separation of the modes with the largest spacing occurring at an AR ~ 1.0. After this point, increasing the AR results in slight reduction of the spectral separation and eventual saturation in the spacing of the modes. To better understand the collective response of a metamaterial formed from these resonators, the reflectance of an array of resonators is shown in Figure 3.2(b). As expected, the reflectance bandwidth is maximized at ARs corresponding to the largest separation between the modes. Furthermore, as the AR is reduced, complete modal overlap occurs, leading to a wavelength at which the resonator is impedance matched to air and a narrow transmission window appears. This effect has previously been studied for cylinder resonators as one way to achieve complete suppression of backscattering[67].

At AR ~1.0, there is also a slight dip in the middle of the reflectance band. This dip can be understood by the fact that this region is far from either resonance and thus $|\varepsilon|$ and $|\mu|$ are small, reducing the magnitude of n'' and thus reducing the strength of the reflectance. Large ARs also result in weakening of the electric and magnetic dipole resonances and a subsequent reduction in the bandwidth of the response. In the design of broadband reflectors, caution must therefore be taken to ensure that spectral separation between the modes and weakening of the resonances does not adversely affect the average reflection across the band.

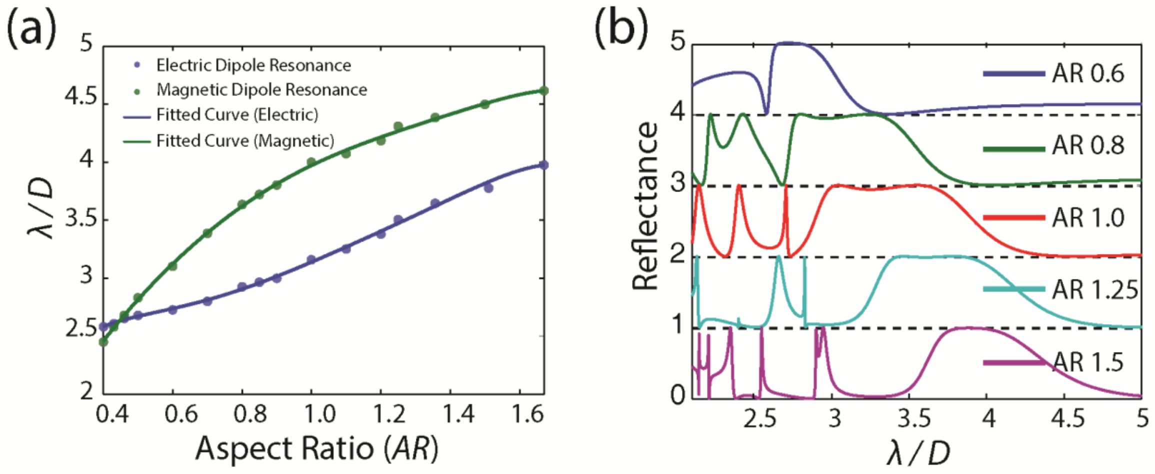

Figure 0.23 (a) Spectral positions of the electric and magnetic dipole Mie resonances as a function of the AR. The solid lines are fitted to the points as a guide for the eye. (b) Simulated reflectance plots for periodic Si cylinder metamaterials, illustrating reflectance as a function of cylinder AR.

With these studies as a guideline, we have chosen a Si cylinder resonator-based metamaterial with H = 500 nm, D = 400 nm (AR = 1.25), and a periodicity of 660 nm for experimental studies. This particular AR and cylinder geometry was chosen as it preserves a broad reflection band while the band's position remains within the measurable range of our microscopy setup. It should also be noted that in experimental studies, H was constrained by the wafers used to realize the metamaterials, as outlined below. To better understand the metamaterial's response, full-wave simulations were performed using the Floquet mode solver using the commercial finite-element code HFSS (Ansys). S-parameter retrieval[89]–[91] was used to extract the effective optical properties. These simulations were performed for Si resonators, in air, with a permittivity equal to that of our experimental samples which was measured with spectroscopic ellipsometry. As illustrated in Figures 3.2(a,b), the metamaterial is single negative with $\varepsilon' < 0$ and $\mu' > 0$ between 1315 nm and 1500 nm. This leads to an extreme impedance mismatch with $z' = 0$ across this bandwidth, as shown in Figure 3.2(c). Within this region, n'' also remains high, satisfying the conditions outlined above and resulting in a band of near-unity reflection as shown in Figure 3.2(d), with a peak reflectance of 99.9% at 1450 nm.

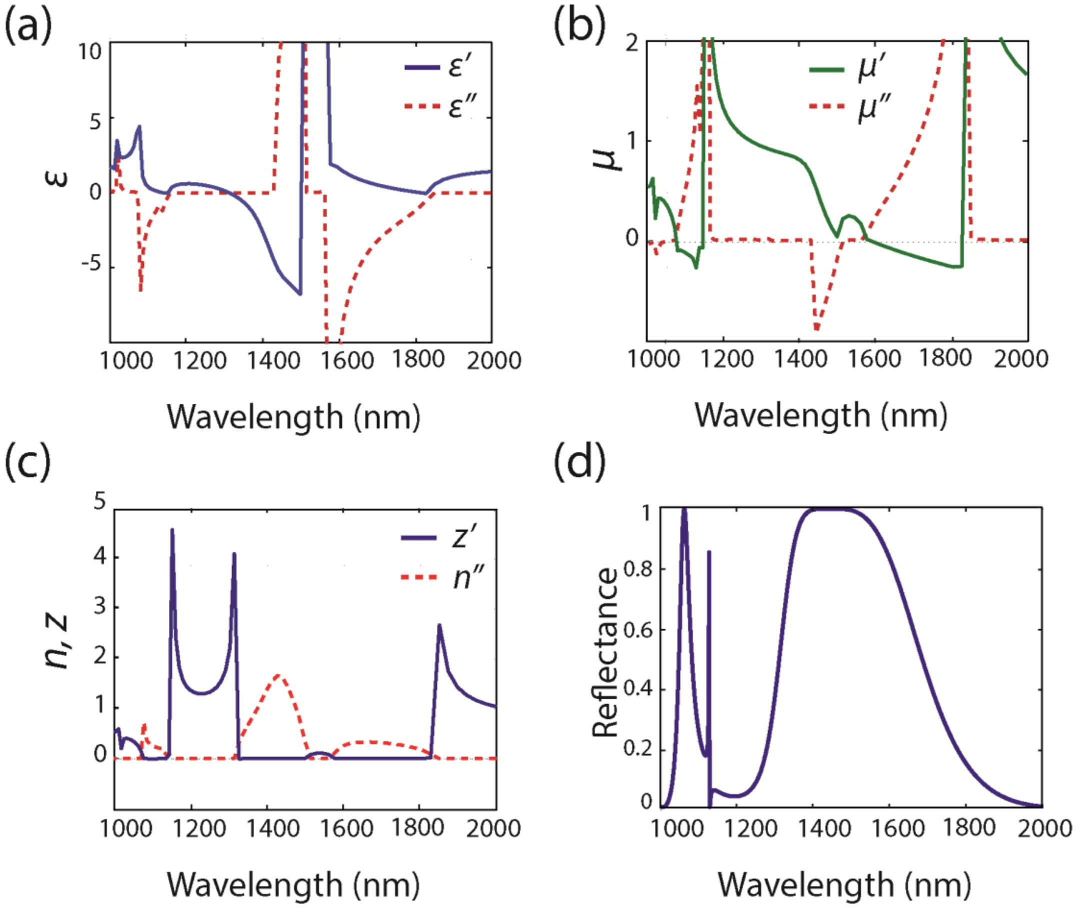

Figure 0.24 (a) Effective permittivity and (b) permeability of a periodic cylinder resonator-based metamaterial in an air background with a resonator geometry corresponding to D = 400 nm, H = 500 nm, and a periodicity of 660 nm. (c) Retrieved n'' and z' for the periodic metamaterial. (d) Reflectance of the metamaterial array numerically calculated using HFSS. A 100 nm near-perfect reflectance band is achieved (reflectance > 99%) from 1398 to 1498 nm.

3.3 Periodic Metamaterial Reflector

The designed metamaterials were realized by fabricating cylinder resonators in the crystalline Si device layer of a silicon-on-insulator (SOI) wafer (SOItech). The SOI wafers consists of a Si handle wafer, a-2 µm-thick buried silicon oxide layer (SiO_2), and a 500-nm-thick crystalline Si device layer. Electron beam lithography (EBL) was used to define the circular mask patterns in poly methyl methacrylate (PMMA) which was spun on top of the Si device layer. This PMMA mask was used to create a 40 nm thick Cr mask, defining cylinders, using a lift-off process. The device layer of the wafers was then etched using reactive ion etching (RIE) to create the arrays of Si cylinders with a diameter of D = 400 nm and height of H = 500 nm (Figures 3.4(a,b)).

The reflectance from the periodic metamaterial was measured with a white light source at normal incidence and is compared with the simulated reflectance in Figure 3.4(c). The simulated reflectance was calculated using dispersive Si optical properties which were measured using ellipsometry. To properly compare with the measured spectra, the simulations include a 2 µm SiO_2 layer below the Si resonators and a semi- infinite Si substrate. The maximum measured reflectance is 99.3% at 1503 nm and the average reflectance is over 98.0% over the wavelength span of 1355 nm to 1555 nm, which is denoted by the grey shaded region in the plot. Moreover, there is excellent agreement between the simulated and measured spectra. It should be noted that the reflectance band is slightly different than that in Figure 3.3(d) due to the presence of the SiO_2 layer and Si handle wafer below the resonators.

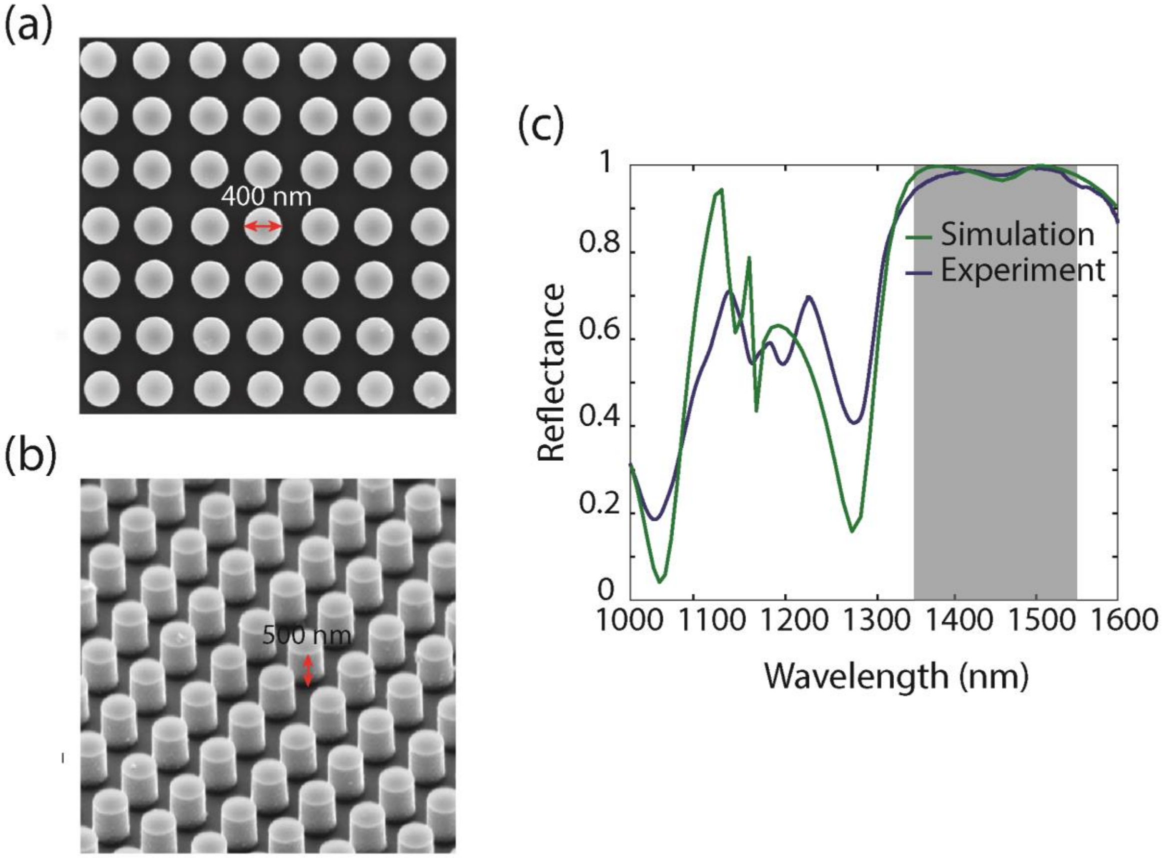

Figure 0.25 (a) Top and (b) isometric SEM images of periodic Si cylinder-based metamaterials. The scale bars in the images are equal to 1 µm. (c) Comparison between the numerically calculated and measured reflectance spectra of the metamaterials. The average reflectance between 1355 nm and 1555 nm (grey shaded region) is over 98.0%.

3.4 Disordered Metamaterial Reflector

One of the benefits of using metamaterials over photonic band gap materials is that their response should, ideally, not be a strong function of the periodicity. This is because the resonance is isolated to the unit cell, and the absence of coupling between unit cells ensures that resonance is not spectrally shifted upon distortion of the lattice. To investigate the effect of periodicity on the perfect reflectors, we have explored the reflectance from disordered arrangements of the cylinders in the metamaterials. The metamaterials were designed with periodic 2 by 2 and 3 by 3 resonator supercells and the position of each resonator within the supercell was randomized by offsetting them from their perfectly periodic x and y positions. The perfectly periodic positions for each sample are based on a resonator spacing of 660 nm, the same spacing that is used for the metamaterials presented in Figure 3.4. The disorder was quantified by computing the standard deviation in the distances between the four nearest neighbors to each resonator in the supercell and then normalizing this by the periodicity of the perfectly ordered array.

Metamaterials with 5 different levels of disorder, equal to 6%, 9%, 15%, 15% and 17% were modeled and experimentally measured for both E_x and E_y polarizations at normal incidence (Figures 3.5(a-e)). Figures 3.5(a-d) correspond to 2 by 2 resonator supercells and Figure 3.5(e) corresponds to a 3 by 3 resonator supercell configuration. Each metamaterial configuration is illustrated by SEM images of the fabricated structure in the inset of the figure. The reflectance from the disordered structures agree well with the simulated curves for both polarizations and exhibit a reflection band that is ~180 nm wide. The maximum reflectance value within the band decreases as the percentage disorder increases, with a maximum reflectance of 98.3%, 96.8%, 91.9%, 92.0% and 86.8% for E_x polarized incidence and 97.1%, 95.8%, 93.1%, 91.0% and 79.9% for E_y polarized incidence.

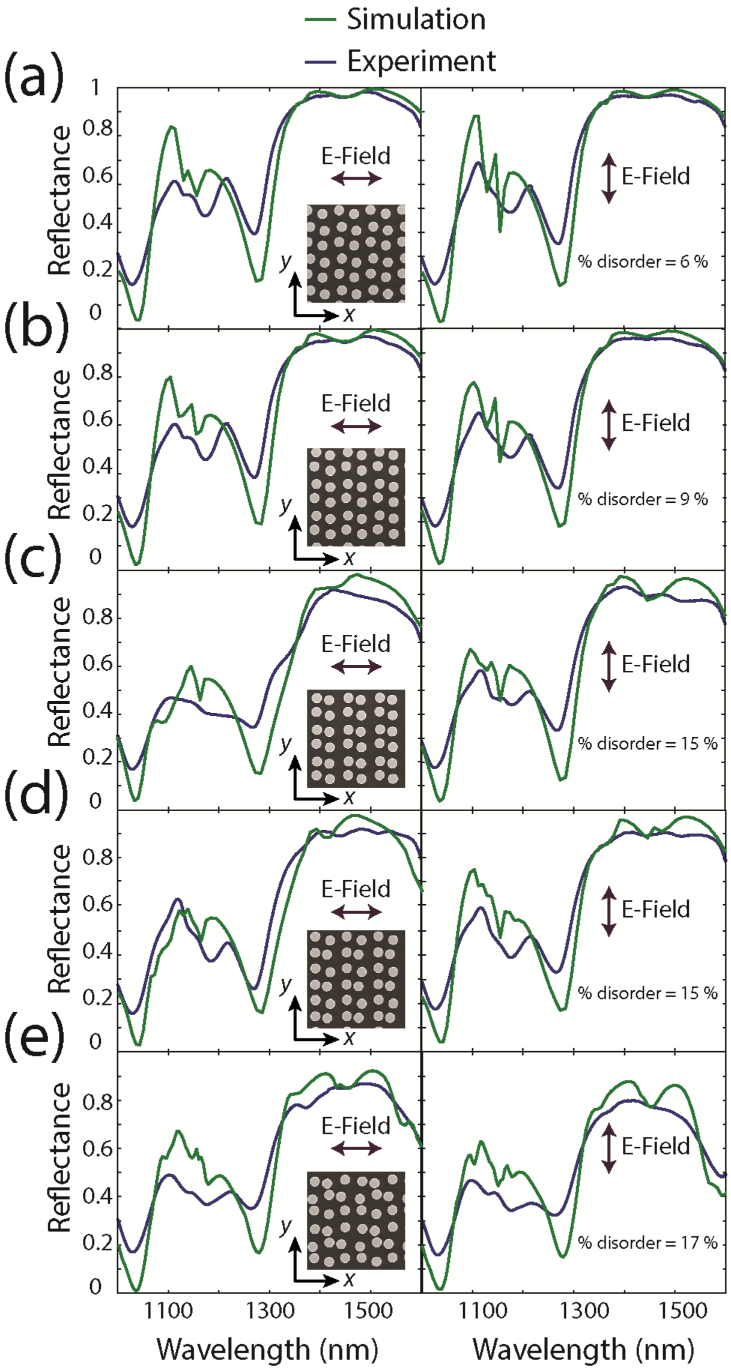

Figure 0.26 (a-e) Comparison between the simulation and measured reflectance spectra for *x* and *y* polarized incidence for metamaterials with 5 different levels of disorder (6%, 9%, 15%, 15% and 17%). SEM images of the metamaterials are shown in the insets. Panels (a-d) have 2 by 2 supercells and (e) has a 3 by 3 resonator supercell. The Figure indicate a reduction of reflectance with increasing levels of disorder for both polarizations.

The correlation between the strength of disorder and the reduction in reflectance is attributed to spatial variations in the coupling between resonators. For large disorders, cylinders within the supercell have different separations and thus different coupling strengths. Spatial variations in the coupling strengths cause the resonances to shift, leading to spatial variations in ε and μ within the supercell. This is illustrated by the far-field scattering cross-sections of a cylinder dimer, plotted as a function of separation, in Figure 3.6(a). It can be observed that narrowing of the gap between the particles leads to blue-shifting of the magnetic dipole resonance, causing it to converge with the electric dipole resonance. Moreover, because the supercell periodicity for the disordered structure is comparable to the wavelength of light within the reflection band, the spatial variations in ε and μ within the supercell lead to the diffraction of light into higher order reflection and transmission modes. This is illustrated in Figure 3.6(b) where we plot the calculated total and 0^{th} order (specular) reflection and transmission of the disordered metamaterial corresponding to Figure 3.5(e). It can be observed that while the total reflection remains high, the specular reflection is reduced due to loss to higher order modes. This issue is not present in the lightly disordered metamaterials in Figures 3.5(a,b) as their spacing remains large enough to prevent significant coupling between the resonators. So, while near-perfect reflection from single layer is not limited to periodic structures, the resonators must be prevented from coming in close proximity to one another. It should be noted that this level of control is potentially achievable when utilizing nanosphere lithography by managing the electrostatic repulsion between the dielectric spheres used for masking[92].

One way to reduce the transmission to higher order modes is to utilize a low index substrate. For instance, we found that some of the 0^{th} order reflectance can be recovered by replacing the SiO_2 / Si substrate with porous Si with an index of 1.1, which supports fewer diffraction modes. Numerical simulations also showed that the reflection band is maintained across all angles of incidence for *s*-polarized light, and up to a 20° incident angle for *p*-polarized light for ordered metamaterials. This allows the use of the metamaterial for moderately curved surfaces such as lenses and extreme curvatures or angles of incidence in applications with a well-defined polarization state.

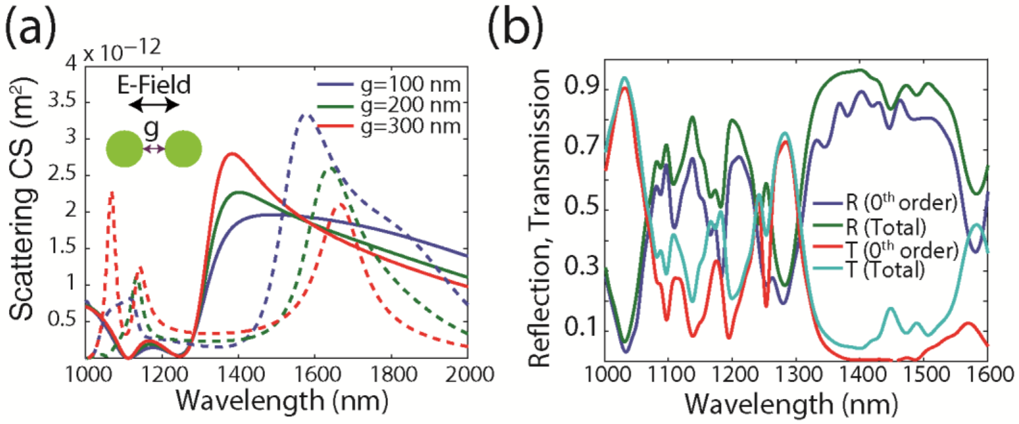

Figure 0.27 (a) Scattering cross-sections of Si cylinder dimers as a function of particle spacing. Solid and dashed lines represent the electric and magnetic contributions to the scattering cross-section, respectively. Reduction in the gap size results in a convergence of the resonance positions. (b) Reflection and transmission for a 3 x 3 supercell metamaterial with a disorder of 17%. While the total reflection remains high, light is lost to higher order reflection and transmission modes.

3.5 Ultra-Broadband Perfect Reflector

So far we explored the electric and magnetic dipole Mie resonances in single dielectric cylindrical resonators and described their roles in achieving broadband high reflection. In this section, we carry forward the systematic understanding of the origin of near perfect reflectance in a periodic metamaterial and attempt to overcome the limitations on perturbation of the modes in a cylindrical structure, where only height to diameter aspect ratio can be varied to separate the dipole modes from each other. To accomplish this, we convert the circular cylinder to an elliptical cylinder, providing control in engineering the geometry of the unit cell. As our goal is to achieve a polarization independent response the unit cell is further modified to contain elliptical cylinders with axes that are perpendicular to each other. A schematic of the unit cell is illustrated in the inset of Figure 3.7(c). The relative bandwidth of the high reflection window is defined as the ratio between the wavelength range with average reflectance above 98% and the center wavelength of the band ($\Delta\lambda/\lambda$). The three important design parameters which contribute to the broadening of reflectance bandwidth are identified as the in-plane aspect ratio, defined by the ratio between the major and minor axis of the single ellipse, vertical aspect ratio, defined as the ratio between the minor axis and height of the resonator, and the duty cycle (DC), defined as the ratio between the major axis and periodicity. First, the effects of these individual design parameters on broadening the bandwidth were separately explored. After that, the combined effects of all design parameters were fine tuned to optimize the bandwidth exhibiting maximum average reflectance. By proper engineering of cross-elliptical cylinder resonator, with in-plane aspect ratio of 4.5, vertical aspect ratio of 0.15 and DC of 0.88, a relative bandwidth ($\Delta\lambda/\lambda$) of 28% (Figure 3.7(c)) is achieved at optical frequencies. The effective permittivity and permeability plots (Figure 3.7(a)) show realization of three single-negative spectral regions ($\varepsilon' / \mu' < 0$) in succession, which are shaded in the Figure 3.7(a) (region 1, 2 and 3). The first single-negative spectral region (shaded region 1) opens up due to a broad electric resonance which exhibits negative permittivity over a wavelength range of 220 nm at the higher frequency side of the resonance. Region 2 defines a single negative spectral region of about 100 nm with permeability being negative. Adjacent to region 2, spectral region 3 again defines a negative permittivity band 30 nm wide. The real part of effective impedance (z') and imaginary part of index (n'') are plotted in Figure 3.7(b). Values of z' remains close to zero over the 3 single-negative spectral regions and n'' shows 4 consecutive peaks within these regions confirming realization of perfect reflection at the respective peak positions based on the analysis in section 3.2.1. The spectral positions corresponding to perfect reflection are marked with dashed lines in Figures 3.7(a,b) and with arrows in Figure 3.7(c).

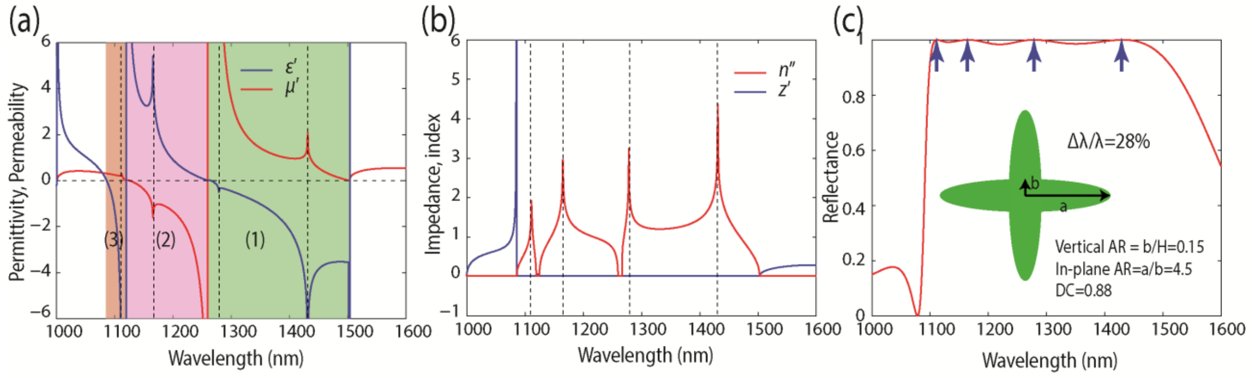

Figure 0.28 (a) Real parts of effective permittivity and permeability of metamaterial formed from cross-elliptical cylinder unit cell arranged in 2D square lattice. The shaded spectral regions (1, 2 and 3) demonstrate the region with single negative metamaterial response. (b) Real part of effective impedance (z') and imaginary part of effective index (n"). In Figs (a,b) the condition for achieving unity reflection is demonstrated with dashed lines. (c) Broadband near perfect reflectance from the metamaterial structure. Schematic of the unit cell geometry is illustrated in the inset. A broad bandwidth (Δλ/λ=28%) with average reflectance of 98% is achieved in the optical frequencies.

We recognize that broadband high reflectance can be achieved with Bragg reflectors. However, the fabrication of a Bragg reflector requires deposition of multiple layers of alternating (high and low permittivity) dielectric materials, which makes the fabrication expensive and complicated. An alternate route to achieve broadband high reflectance at optical frequencies with a single layer of patterned structures has been proposed in terms of high contrast gratings (HCG) [93], [94]. In spite of matching bandwidth and reflectance strength with a Bragg reflector, HCGs suffers from a polarization dependent response. Metamaterials composed of periodic arrays single layer of cross-elliptical cylinders, on the other hand, have a polarization independent response with a bandwidth and reflectance comparable to HCGs. Dielectric unit cells in the form of cross-elliptical cylinders could also be used to explore other novel properties such as a negative index.

3.6 Conclusion

In conclusion, the electric and magnetic dipole modes of single Si cylindrical resonators have been manipulated by changing the cylinder height to diameter aspect ratio. Separating the dipole modes leads to the formation of a single negative metamaterial with an extreme impedance mismatch, which, along with satisfying the condition of large imaginary effective index, results in broadband near perfect reflectance. Furthermore, since the metamaterial response is dominated by the Mie resonances in the individual resonators, it is tolerant to disorder in the lattice, so long as significant coupling between resonators is avoided. The potential to achieve near-perfect reflection with a compact disordered MMs opens the door to large-area fabrication using low-cost and high-throughput patterning techniques such as nanosphere lithography, which we will discuss in the next chapter. Furthermore, a general mechanism to broaden the high reflectance bandwidth is provided by manipulating the fundamental as well as higher order resonances by controlling the dielectric resonator shape.

Chapter 4

Large-Scale Metamaterial Perfect Reflectors

4.1 Introduction

In *Chapter* 3, electron beam lithography was used for a proof-of-concept demonstration of a dielectric metamaterial reflector with a sample size of 100 μm x 100 μm. However, for large-area applications, electron beam lithography is impractical. Here, we describe the design and fabrication of large-scale (centimeter-sized) MM perfect reflectors based on silicon (Si) cylinder resonators. Cylindrical resonators are a particularly interesting unit cell design because they allow spectral separation of the electric and magnetic Mie resonances by changing the aspect ratio, and can be patterned by self-assembly based nanosphere lithography, a low-cost and high-throughput fabrication technique. Using this platform, we demonstrate near-perfect reflection over large centimeter-sized areas with around half a billion resonators comprising the metamaterial. In addition, by studying the effect of lattice disorder originating from the self-assembly patterning process, it was found that the reflectance due to the magnetic resonance is more tolerant to disorder than the electric resonance due to better confinement of the optical mode. This research could lead to the use of large-scale perfect reflectors within the telecommunication band for large-area applications.

Additionally, the metamaterial approach provides the freedom to manipulate both the magnetic and electric response of the reflector. Conventional mirrors made from metal and Bragg reflectors operate as electric mirrors in which the reflected electric field undergoes a 180º phase change resulting in an electric field minimum at the mirror surface. Dielectric metamaterial perfect reflectors can exhibit perfect reflection due to both electric and magnetic dipole Mie resonances[61], [71], [86], [95]. In this case, the phase of the reflected electric field can be swept from 180º to 0º by moving from the electric to the magnetic resonance[71], [96]. Most importantly, at the magnetic resonance a reflection phase shift of 0º results in an electric field maximum at the surface of the material, strongly enhancing the light-matter interaction[97] of materials placed on the mirror. This field enhancement could be useful for applications such as surface-enhanced Raman spectroscopy or SERS.

4.2 Nanosphere Lithography: A Brief Review

Nanosphere lithography, also known as colloidal lithography or natural lithography[98], has been proven to be a simple and high throughput large-scale lithography technique with feature sizes ranging from couple of 100 nm to micrometers. It was first introduced in early 80's by Fischer and Zingsheim[99] and Deckman and Dunsmuir[98]. The process is generally categorized in to two steps. The first step is the self-assembly of polystyrene (PS) particles in a hexagonal close-packed monolayer on a substrate. The second step is the downscaling of the size of the PS particles so that it results in a hexagonal non close-packed lattice. The following fabrication steps depend on the intended applications of the device. The non-close-packed polystyrene arrays either can be used as an etch mask to pattern the metallic or dielectric layer underneath or can be used to form a shadow mask during a directional metal evaporation. Subsequent lift-off of the nanospheres yields intricately shaped plasmonic resonators[45], [100], [101].

There are a numerous methods that has been explored in generating highly close packed self-assembled PS monolayers such as spin coating[102]–[111], self-assembly at air-water interface[32]–[49], dip drying[112], colloid confinement methods[113] and many more. Different methods have their own advantages and disadvantages. After a thorough review of the nanosphere lithography literature we decided on implementing a modified technique based on self-assembly of PS nanospheres at an air-water interface followed by transfer of the pattern to the substrate.

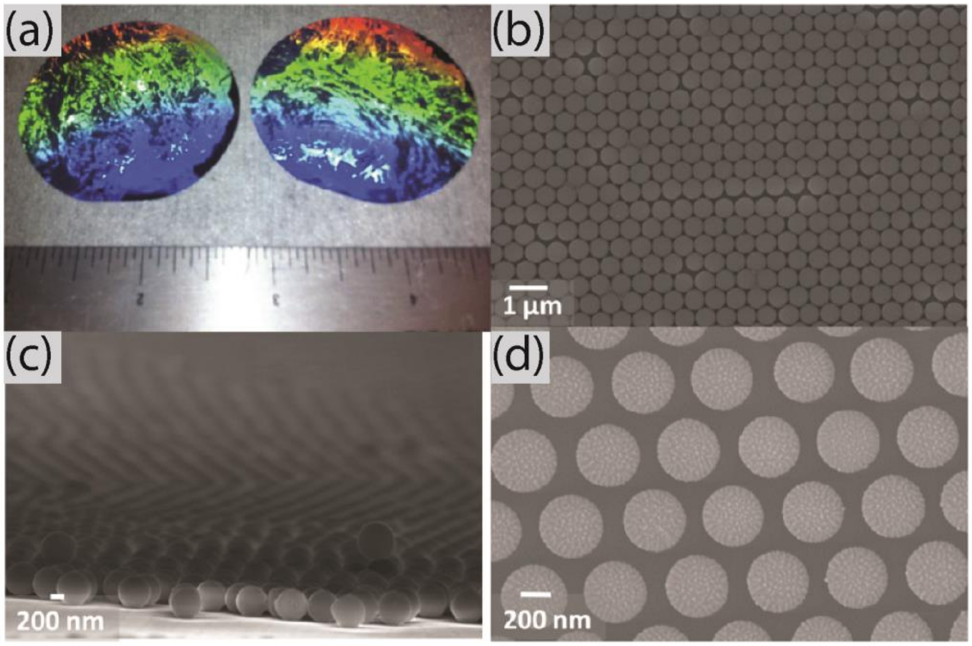

Figure 0.29 (a) Camera image of wafer of 2 cm diameter coated with close-packed monolayer of PS particles. SEM images (b) top view and (c) tilted view of the close-packed monolayer of PS particles. (d) SEM image of downscaled PS particles. Adapted from reference [114].

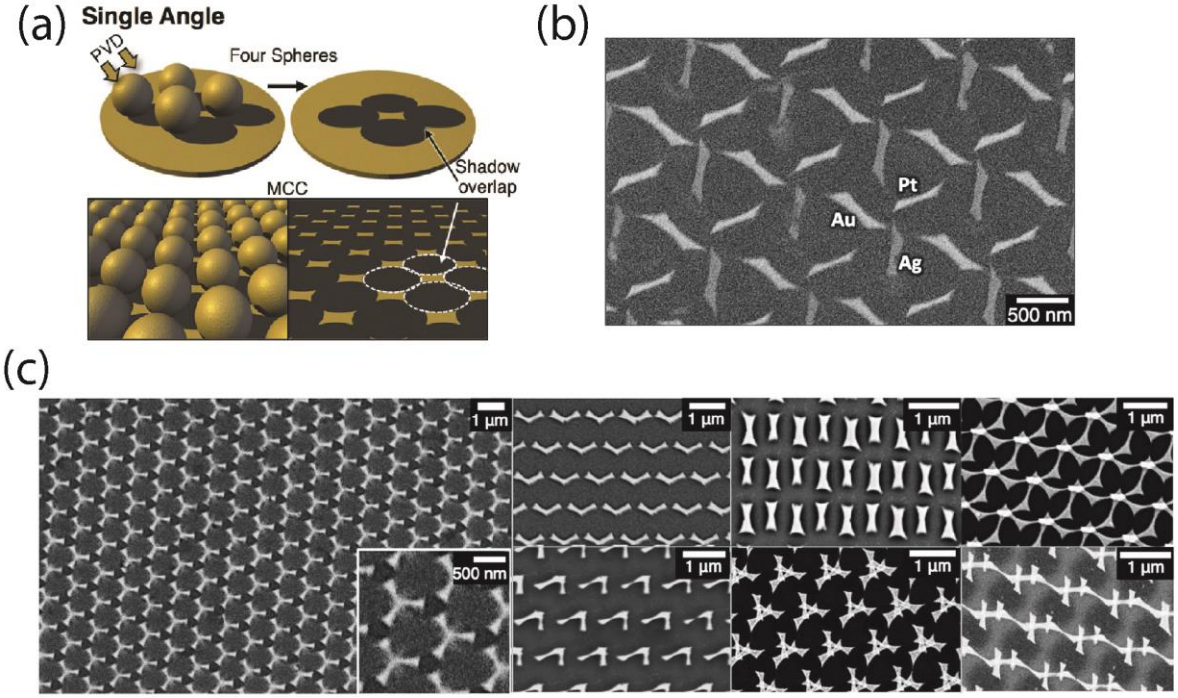

Figure 0.30 (a) Schematic of shadow nanosphere lithography demonstrating generation of a single bar or an array of bars by a single angle of deposition. (b) SEM image of an array of chiral tri-polar structure composed of three different metals of 20 nm thickness fabricated using shadow nanosphere lithography. (c) SEM images of various intricate plasmonic structures demonstrating the capability of the fabrication of complicated structure utilizing behavior of the shadow cast by nanospheres. Adapted from reference [100].

4.3 Nanosphere Lithography: Our Approach to Large-Scale Metamaterial Fabrication

In the following section I describe our modified nanosphere lithography technique. First, polystyrene (PS) spheres (820 nm in diameter) were self-assembled in a monolayer of hexagonal close packed lattice at an air-water interface[34], [41], [46], [48] (Figure 4.3(a)). Then, two key techniques—orientating the PS spheres and maximizing their concentration— were used to expedite the formation of a wafer-scale close-packed pattern with millimeter scale single grain sizes. The reorientation of PS particles at the air-water interface was accelerated by perturbing the particles with a gentle and controlled flow (5 L / min) of compressed air through a flat nozzle[46]. We maximized the concentration of PS particles at the air-water interface by minimizing loss of PS particles in the liquid phase[115] (see Methods for details). After formation of the close-packed monolayer of PS particles at the air-water interface, the pattern was transferred onto an SOI substrate placed below the water surface at a 10º inclination angle[42] by slowly draining the water from the Teflon bath.

Commercially available polystyrene spheres in an aqueous solution (10 wt%) were mixed with an equal volume of ethanol and injected on to the water surface at a rate of 5 µL/min using a syringe pump. A tygon tube with a diameter of 0.5 mm was connected to the syringe and held upright with the bevel tip of the tube just touching the water (18.2 M-Ohm) surface. This results in the formation of a meniscus onto which PS particles are deposited. This technique reduces the chance of PS particles falling into the liquid phase. Contrary to the common practice of using a surfactant (SDS or Triton-X-100) to facilitate self-assembly process, here we avoided using any surfactant as PS particles fall into the liquid phase more readily with increasing surfactant concentration. The self-assembly process was facilitated by reorienting the PS particles on the water surface using a controlled flow of compressed air through a flat nozzle (5L/min) that was aimed at the water surface. This perturbation assisted self-assembly process led to better packing and larger single grains. It took about 5-6 minutes to cover the entire water surface held in a cylindrical Teflon bath with a diameter of 100 mm. The defects in the close-packed monolayer formed at the air-water interface are unavoidable due to size variations in the PS particles and results in stress within the pattern. To relieve the stress and to accommodate the defects such as PS particles randomly dispersing in the monolayer, the pattern was transferred on a substrate at a 10° inclination angle. The substrate was placed below the water surface and the film was deposited by slowly draining the water from the bottom of the bath. The overall process of pattern transfer and drying the substrate in air took 20 to 25 minutes.

An image of a PS pattern assembled on an SOI substrate (2 cm-by-2 cm) is shown in Figure 4.3(b). The strong opalescence indicates the formation of a close-packed pattern with individual single grain sizes varying from 2 mm to 10 mm. Next, the PS spheres (SEM image in Figure 4.3(c)) were downscaled in size to 560 nm (Figure 4.3(d)) using isotropic oxygen plasma etch. This pattern served as an etch mask for the subsequent RIE processing of Si using SF_6 / C_4F_8 chemistry. Figures 4.3(e,f) show SEM images of the top and isometric views of the final metamaterial (after removal of PS mask) consisting of Si cylinders (D_{top}=480 nm, D_{bottom}=554 nm, H=335 nm and P=820 nm) arranged in a hexagonal lattice. The SEM images along with the optical image clearly demonstrate that the nanosphere lithography can yield high quality dielectric resonators over a large area.

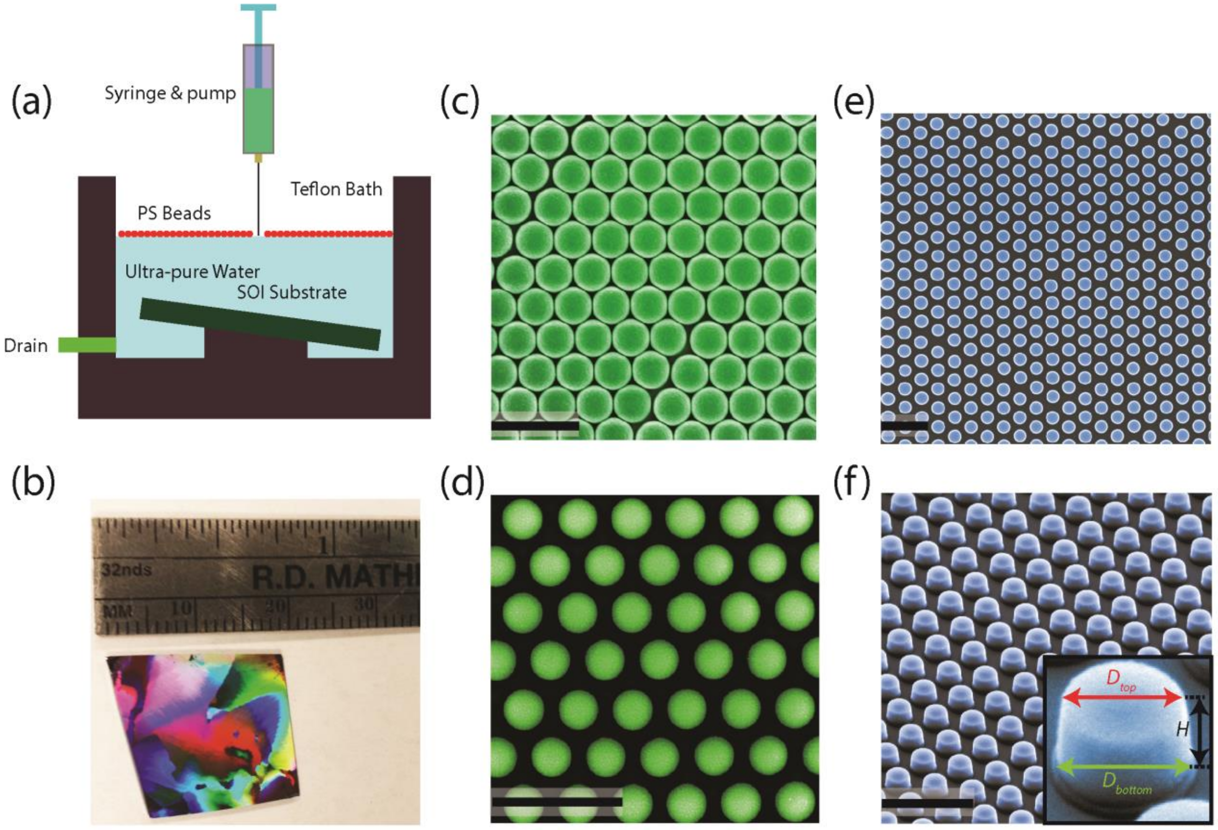

Figure 0.31 (a) Schematic of the self-assembly based nanosphere lithography technique. PS particles are first assembled in a monolayer at an air-water interface. The monolayer is then transferred to the SOI substrate by slowly draining the water from the bottom of the Teflon bath. (b) Camera image of the large-scale pattern (~2 cm-by-2 cm) of close-packed polystyrene spheres on an SOI substrate. Strong opalescence suggests fabrication of a close packed pattern. The pattern also exhibits formation of large single grains (mm size). (c-f) SEM images of (c) hexagonal close-packed polystyrene spheres (green, false color) of diameter 820 nm and (d) polystyrene spheres downscaled in size to 560 nm using isotropic O_2 plasma etching. (e) Top view of the final metamaterial structure consisting of an array of Si cylinders (blue, false color). The cylinders were formed by using SF_6/ C_4F_8 reactive ion etch chemistry. (f) Tilted view (45°) of the final metamaterial consisting of an array of Si cylinders (blue, false color). The inset shows an SEM image of a single Si resonator with a top diameter (D_{top}), bottom diameter (D_{bottom}) and height (H) of 480 nm, 554 nm and 335 nm, respectively. The scale bar for SEM images (c-f) is 2 μm.

4.4 Experimental Measurements

The size variations in PS spheres (coefficient of variance (CV) ≤ 3 %) and the self-assembly process resulted in some disorder of the lattice. The positional disorder (4.1 %) was calculated by first finding the standard deviation of nearest neighbor distances for 188 resonator samples (SEM image) and then normalizing the standard deviation to the ideal periodicity (820 nm). To characterize the role of disorder, the reflectance from the metamaterial was measured using a custom-built infra-red (IR) microscope with white light illumination at normal incidence to the metamaterial surface and was compared with the simulated reflectance from a perfectly periodic metamaterial (Figure 4.4(a)). The simulated reflectance was calculated using the dispersive optical properties of Si measured by ellipsometry. To properly compare with the measured spectra, the simulations include a 2 μm SiO_2 layer below the Si resonators and a semi-infinite Si substrate. The reflectance from the metamaterial reflector was first normalized to the reflectance from a silver mirror. The absolute reflectance of the silver mirror was also measured and used to calculate the absolute reflectance of the metamaterial reflector. The maximum reflectance measured at normal incidence was 99.7 % at 1530 nm, which is in excellent agreement with the simulation. It is important to note that the maximum reflectance from the metamaterial reflector surpasses the average reflectance of the silver mirror (97.7 %) in the telecommunications wavelength band.

To characterize the uniformity of the reflectance over a large area, we carried out a spatial scanning of reflectance at 1530 nm over a 10 mm-by-10 mm area of the fabricated sample. The spatial reflectance scan, shown in Figure 4.4(b), indicates an average reflectance of 99.2 % with a standard deviation over the entire area of only 0.21 %, which is less than the measurement noise of 0.25 %. The uniformity of the peak reflectance over such large areas indicates that the homogenized properties of the metamaterial hold over large areas despite the disorder of the lattice.

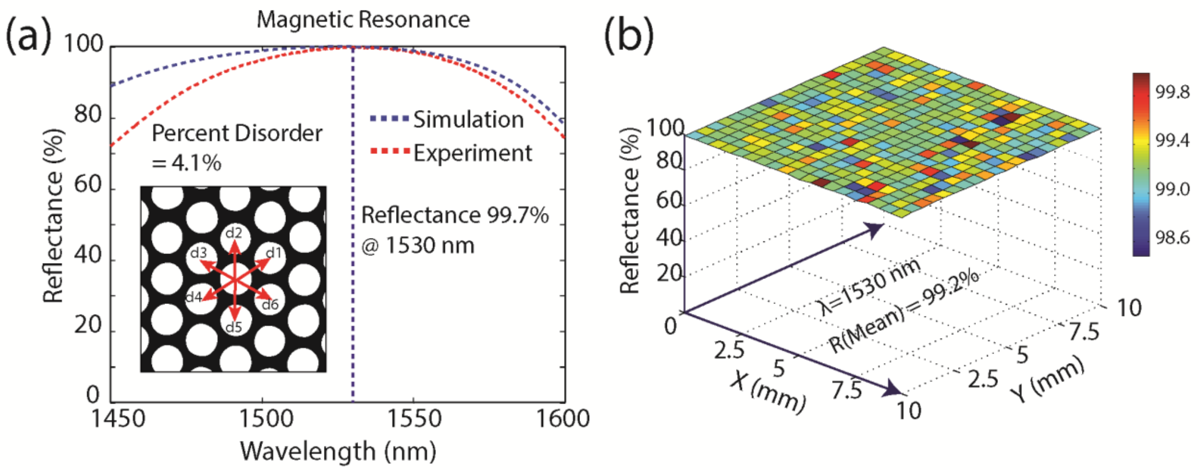

Figure 0.32 (a) Measured and simulated reflectance of the metamaterial demonstrated in Figure 4.3. A maximum reflectance of 99.7 % is achieved at 1530 nm. In the inset a binarized SEM image is shown. The percent disorder calculated using 188 resonator samples is 4.1 %. d1 through d6 denote the 6 nearest neighbor distances from a particular resonator. The simulated reflectance was calculated using a perfectly periodic metamaterial. (b) Spatial scan of reflectance at 1530 nm over a 10 mm by 10 mm area of the metamaterial. The average reflectance over the entire area is 99.2 % with measurement error of ±0.25 %.

To illustrate the angle-resolved behavior of the perfect reflector we have plotted the theoretical and experimental reflectance at 1530 nm as a function of the angle of incidence for *s* (electric field parallel to the surface) and *p*-polarizations (magnetic field parallel to the surface) in Figure 4.5. In the experimental measurements, the sample was mounted in an integrating sphere and reflectance was measured for incident angles ranging from 10° to 45° with respect to the normal direction of the substrate. The theoretical and experimental data are in good agreement and it can be observed that the reflectance for both polarizations is constant up to an angle of 15º. For larger angles, the reflectance for *s*-polarized light remains constant while the *p*-polarization experiences a marked decrease in reflectivity. We also find that the higher-order reflection modes at 1530 nm are negligible for all angles of incidence, indicating that the most of the incident energy is reflected into the zeroth order specular mode. To demonstrate the uniformity of its specular reflectance, a Vanderbilt University logo was reflected off the metamaterial at a 20° incident angle and imaged using an IR camera at 1530 nm. The diameter of the logo on the MM reflector surface was approximately 7 mm. The image produced by the MM reflector is compared to that produced by a metallic mirror in Figure 4.5(b). No distortion in the image was found in the case of MM reflector compared to the case of the planar metallic mirror.

To better understand the polarization and angular dependence of the reflection, the numerically calculated reflectance spectra for *s*- and *p*-polarizations are plotted as a function of incident angle in Figure 4.5(c, e), respectively. For *s*-polarization the magnetic dipole mode maintains a relatively constant spectral position with increasing angle of incidence as demonstrated in the reflectance spectrum in Figure 4.5(c). The presence of the magnetic dipole at an 80° incident angle and illumination wavelength of 1530 nm is further supported by the field plot in Figure 4.5(d). However, for *p*-polarization, increasing the illumination angle results in a red-shift of the magnetic mode (Figure 4(e)), decreasing reflection at 1530 nm. Another interesting feature to note here is the formation of a sharp reflectance peak due to vertical magnetic dipole resonance (H_z). The field plot corresponding to the vertical magnetic dipole at 1833 nm and an 80° angle of incidence is illustrated in Figure 4.5(d).

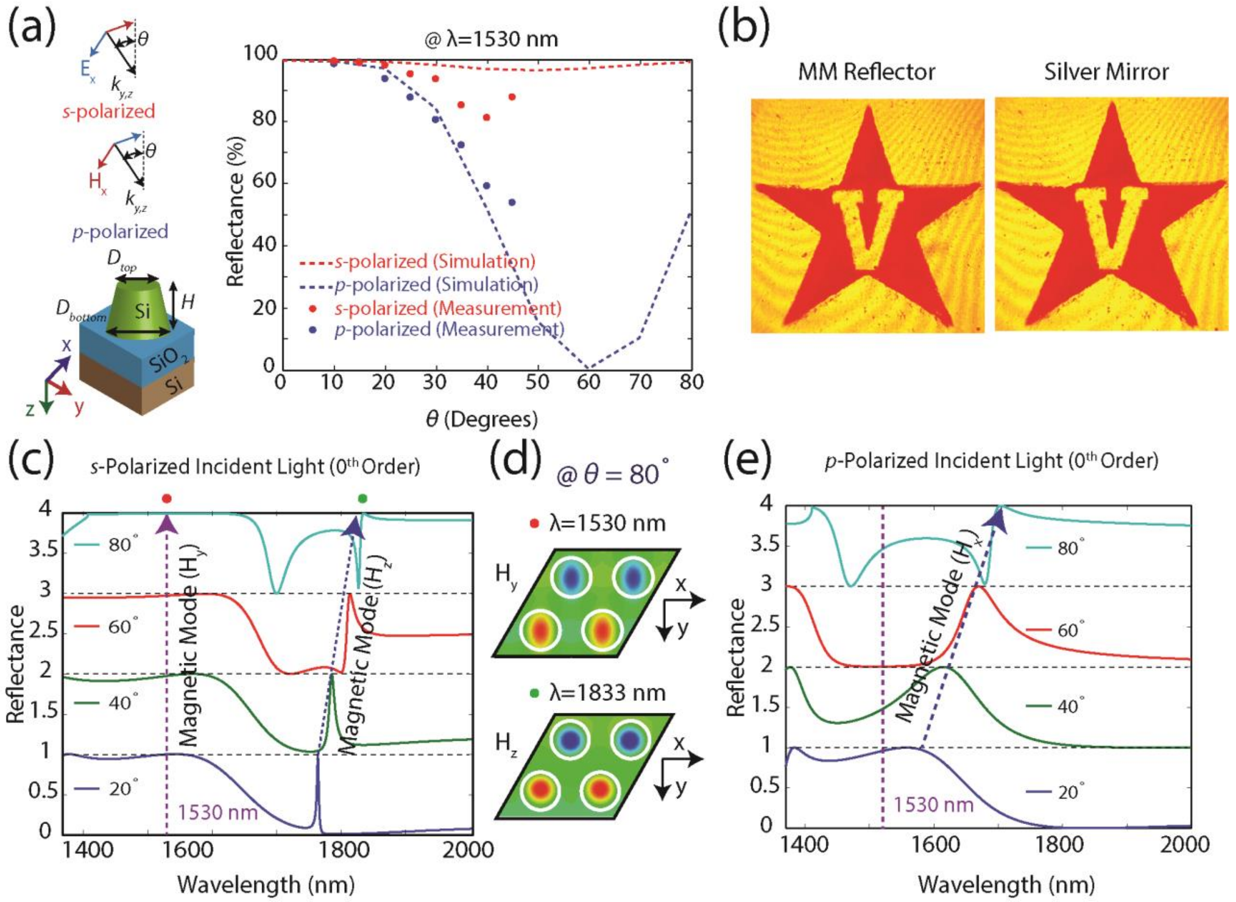

Figure 0.33 (a) Schematic of *s* and *p*-polarized incident light and the simulated and experimentally measured angle-resolved reflectances at 1530 nm. Reflectance was measured for incident angles between 10° and 45°. (b) IR camera images of a Vanderbilt logo that was reflected off of the MM reflector and a silver mirror with a 20 degree angle of incidence. The MM reflector leads to strong specular reflectance. The beam diameter at the surfaces of the reflectors was ~7 mm. (c) Simulated angle-resolved specular reflectances for *s*-polarized light at 20°, 40°, 60° and 80° angle of incidence. (d) Magnetic field plots (H_y and H_z) illustrating magnetic dipole resonances. (e) Simulated angle-resolved specular reflectances for *p*-polarized light at 20°, 40°, 60° and 80° angles of incidence.

It is also critical to understand what role disorder plays on the electric and magnetic resonances of the surface. Figure 4.6(a) compares the measured reflectance from a MM with a disorder of approximately 4 % and the simulated reflectance from a perfectly periodic metamaterial with a hexagonal lattice (*P*=820 nm). While the measured reflectance shows excellent agreement with the simulated reflectance at the magnetic resonance, it is approximately

15 % less than the simulated reflectance at the electric resonance. This is because the electric mode is leaking into the regions between the resonators, whereas the magnetic mode is well confined within the resonator. To achieve tolerance to disorder, the electric mode must be more confined inside the resonator which can be achieved by increasing the aspect ratio. In Figure 4.6(b) we present the simulated and measured reflectance from a metamaterial with a resonator height of 500 nm, increased from 335 nm in the original design. The new design has a 200 nm broad reflectance band centered at 1700 nm with an average measured reflectance greater than 98 %. The simulated electric field plot shows better confinement for the electric mode inside the resonators (D_{top}=460 nm, D_{bottom}=600 nm, H=500 nm, P=820 nm) than that observed in Figure 4.6(a) which ultimately results in higher reflectance near the electric mode in the fabricated samples.

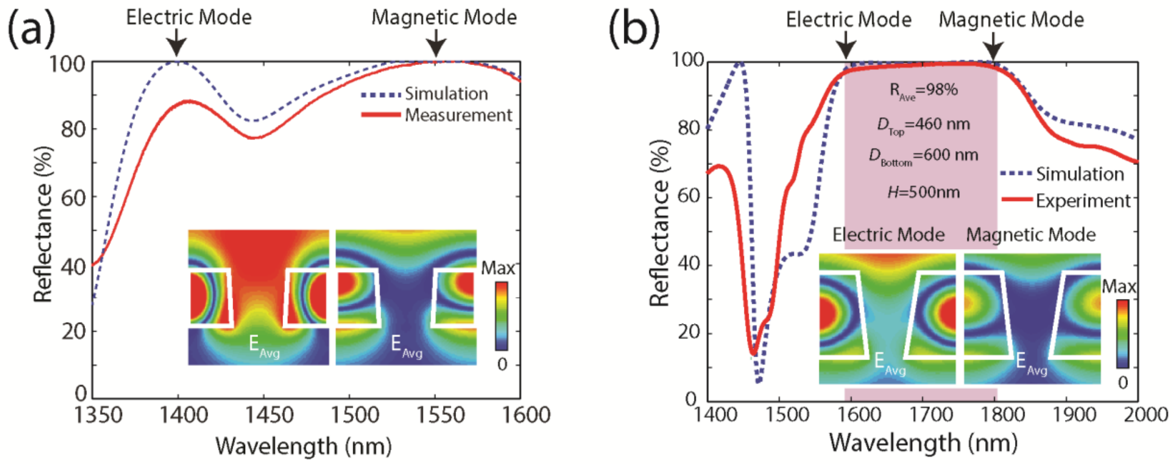

Figure 0.34 (a) Comparison of the simulated reflectance spectra of a perfectly periodic metamaterial and the measured reflectance spectra of a metamaterial with 4% disorder in the lattice. The figure demonstrates the higher tolerance to disorder of the magnetic mode compared to the electric mode. Simulated time-averaged electric fields are shown for the two modes in the inset. The electric mode results in more field being located outside of the resonator, resulting in a lower tolerance to disorder. (b) Simulated and experimental reflectances of a broadband mirror demonstrating strong reflectance over a 200 nm bandwidth with an average reflectance (experiment) of 98%. The resonator dimensions are D_{top}=460 nm, D_{bottom}=600 nm, H=500 nm and the periodicity of lattice is P=820 nm. Simulated time-averaged electric field for the electric and magnetic modes are shown in the inset. Better confinement of electric mode is apparent.

It is interesting to note that the metamaterial perfect reflector design, in contrast with metallic mirrors, can be used to realize magnetic mirrors in which the maxima of the electric field is located at the surface of the metamaterial. However, only when the magnetic mode is spectrally separated from the electric mode will the perfect reflection due to the magnetic mode lead to the formation of a magnetic mirror. Due to the moderate dielectric constant of Si, the resonators must be separated optimally to minimize coupling while at the same time avoiding diffraction. This can be achieved using a metamaterial design with $AR=H/D$=1.675 and $D_n=D/P$=0.24. As shown in Figure 4.7(a), the reflection phase at the magnetic-dipole resonance (λ_n=1.16) remains close to zero, consistent with a magnetic mirror, while the difference in reflection phase between the electric (λ_n=1.01) and magnetic resonances is close to 180°. Figure

4.7(b) illustrates the phase offset[71] of the reflected electric field of the metamaterial reflector compared to a perfect electric conductor (PEC), demonstrating the magnetic mirror response. Furthermore, the metamaterial reflector shows no offset in reflection phase compared to a PEC at the electric resonance, as shown in Figure 4.7(c).

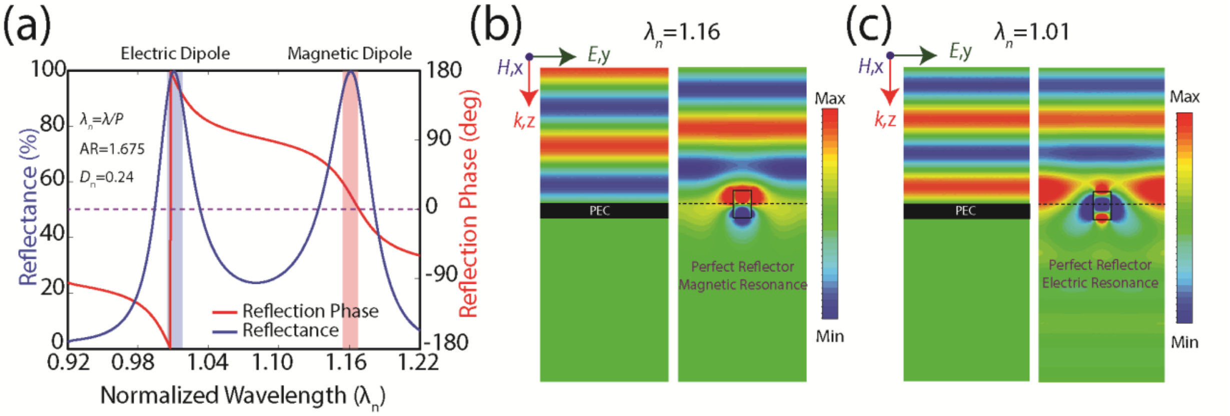

Figure 0.35 (a) Simulated reflectance with respect to normalized wavelength. Perfect reflection is present for both the spectrally separated electric and magnetic modes. This results in a perfect electric reflector with a reflection phase close to 180°, the same as a metallic mirror. The magnetic mode however has a reflection phase close to zero. (b) Electric field plots demonstrating the phase offset due to a metamaterial perfect magnetic reflector with respect to a perfect electric conductor (PEC). (c) Electric field plots demonstrating no phase offset between a metamaterial perfect electric reflector with respect to a perfect electric conductor (PEC).

4.5 Conclusion

In summary, we demonstrated that dielectric MMs can overcome two serious issues of plasmonic metamaterials—absorption loss and scalability limitations. Furthermore, these reflectors are tolerant to disorder and can be designed for either narrowband or broadband performance. To the best of our knowledge, this is the first reported effort for scaling up the fabrication of all-dielectric metamaterials to large areas using a simple, low-cost, and high-throughput method. This research could pave the way towards experimental demonstrations of other large-scale metamaterials and metasurfaces with even more complex optical properties.

Chapter 5

Large-Scale Gradient Metasurface Using Nanospherical Lens Lithography: A Perspective of Advanced Large Scale Lithography with Spatial Control of Patterns

5.1 Introduction

Self-assembly based nanosphere lithography has been proven to be a low cost and high throughput patterning technique for large area patterning of materials. In *Chapter 4*, we have extensively studied and demonstrated large scale fabrication of dielectric metamaterials using nanosphere lithography. While the technique is restricted to the fabrication of circular patterns, asymmetric patterns such as ellipses can be generated using a more advanced nanosphere lithography technique commonly known as nanospherical lens lithography or nanosphere photolithography[116]–[118]. Here, we take advantage of nanospherical lens lithography, which utilizes light-focusing through the nanospheres to expose the underlying photoresist, to further develop a novel large scale gradient lithography technique allowing spatial control over the orientation of asymmetric patterns.

5.2 Nanosphere Lens Lithography: Past Achievements

In order to illustrate the large scale gradient lithography technique we have to first understand how basic nanospherical lens lithography works. Nanospherical lens lithography or nanosphere photolithography is a novel photolithography technique that utilizes a self-assembled planar array of spheres as optical lenses to generate regular hole-patterns over large areas on a photoresist. Figure 5.1 shows the basic process flow of nanosphere photolithography. First, a thin photoresist film is spin coated on the substrate (Figure 5.1(a)) and soft baked at 95° C.

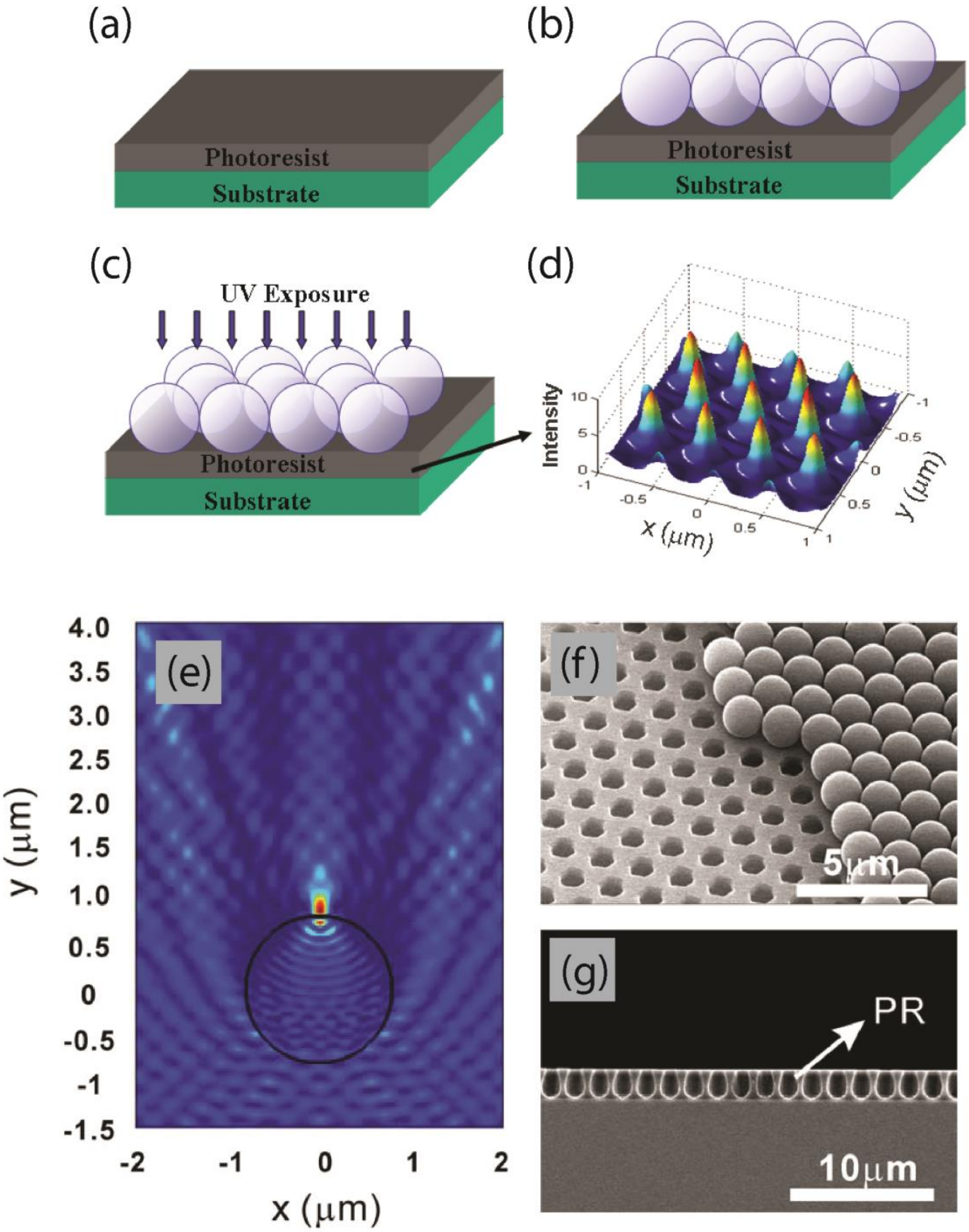

Figure 0.36 (a-c) Schematic of photolithography using PS nanospheres. (d) Simulated electric field distribution in photoresist layer. (e) 3D FDTD simulation demonstrating light focusing ability of single PS nanosphere. (f) SEM image of circular-hole patterns on photoresist after development. Some left-over PS nanospheres helps to visualize that the circular-hole patterns are transferred from the nanospheres. (g) Cross-sectional view of circular-hole patterns in photoresist. Adapted from references [119] (a-d), [120] (e-g).

Then, polystyrene spheres are self-assembled in a monolayer on the photoresist layer (Figure 5.1(b)). After that, the polystyrene particles are exposed with UV light which is focused on the photoresist layer by the polystyrene spheres exposing the resist (Figure 5.1(c)). Figure 5.1 (d) shows the intensity plot on the photoresist surface. The focusing of UV light with a single PS particle is demonstrated with the simulated field plot (Figure 5.1(e)). After the exposure, the sample was sonicated in DI water to remove the PS particles. Finally, the photoresist is developed and rinsed in DI water to reveal the final pattern as illustrated in Figures 5.1(f, g).

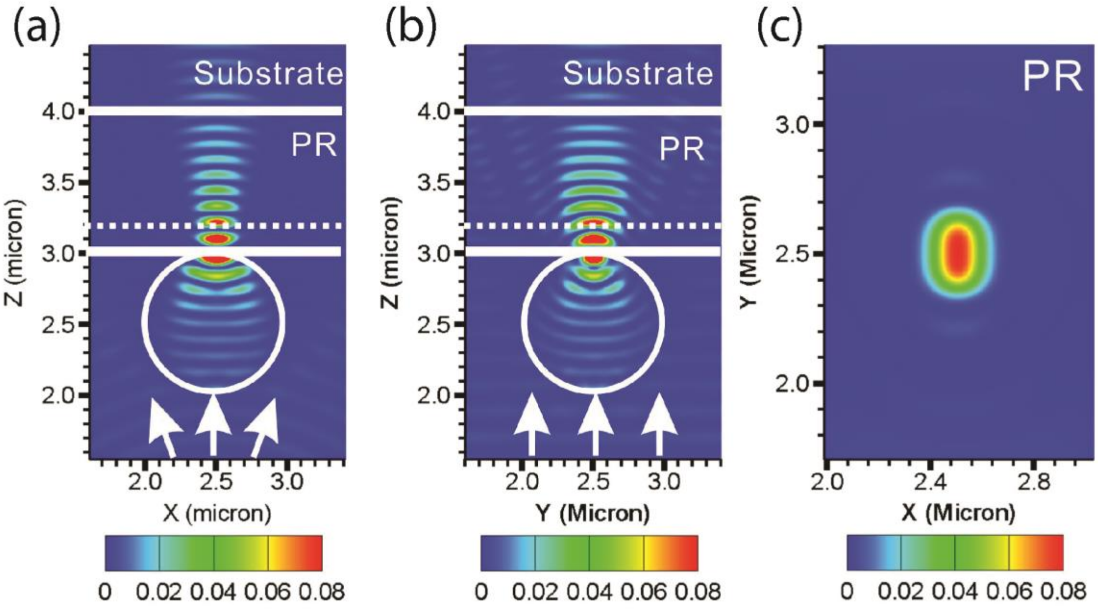

Figure 0.37 (a-c) Simulated electric field demonstrating field concentration in elliptical spatial pattern as asymmetric UV light focused by PS nanosphere. Adapted from reference [118].

The simulated field profiles in the vicinity of a nanosphere with a diameter of 1 μm are illustrated in Figures 5.2(a–c) at 3 orthogonal planar cross-sections i.e. at *xz*, *yz*, and *xy*. The asymmetric UV light (365 nm) is emitting from a line-shaped source oriented along the y axis. The asymmetric light propagation is defined by its two finite propagation vectors k_x and k_z, with

k_y=0 (Figures 5.2(a, b)), i.e. propagation vector along the axis of the line source is zero. This asymmetry in the in-plane wave vector causes asymmetry in focusing of light by the nanospheres. Because of the finite wave vector along x direction (finite k_x and hence divergent beam) light is more tightly focused along x compared to y direction (as k_y=0) and it generates asymmetric or elliptical focusing spot size in xy plane (Figure 5.2(c)).

Figures 5.3(a-d) illustrate SEM images at different stages of the lithography. Figure 5.3(a) illustrates SEM images of PS nanospheres assembled on the photoresist layer. The SEM image of elliptical-hole pattern is demonstrated in Figure 5.3(b). The SEM images of final structures with two different orientations of the metal nanorods (after metal deposition and lift-off) are shown in Figures 5.3(c, d).

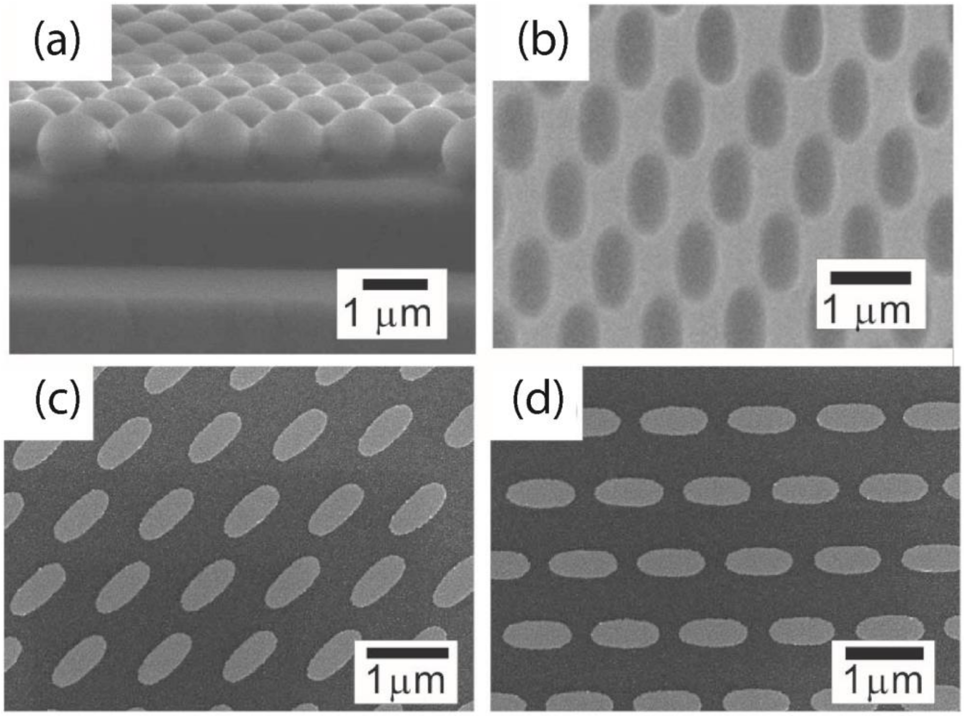

Figure 0.38 SEM images at different steps of lithography to generate elliptical patterns. (a) Self-assembled close-packed nanospheres. (b) Elliptical-hole patterns in photoresist after lift-off. (c,d) metal nanorods after lift-off, oriented differently. Adapted from reference [118].

5.3 Large-Scale Metasurface Using Modified and Advanced Nanospherical Lens Lithography

5.3.1 Optical Set Up for Lithography

With this basic understanding of nanospherical lens lithography, here we describe our approach to modify the basic nanospherical lens lithography to further develop large scale gradient metasurfaces. Figure 5.4(a) demonstrates the schematic of the optical set-up for the exposure. A CW Nitrogen (N_2) laser (405 nm) is used as the light source. The 405 nm laser light first goes through a 50:50 non-polarizing cube beam splitter and is reflected off of a digital micro-mirror device (DMD), which imparts a desired spatial pattern in the reflected light with this pattern being imaged at the sample. Here, it is important to note that spatial patterning of light is important to define a particular region in the sample having a particular orientation of the elliptical pattern. The spatially patterned light (Figure 5.4 (b)) is again reflected from the beam splitter. The orientation of the ellipse is controlled by masking the Fourier plane with a rectangular slit. The rectangular slit transmits all the k-vectors along the length of the slit, while suppresses the high *k*-vectors in the direction of the short axis. All the higher order diffracted modes from the micro-mirror array are also masked at the Fourier plane. The transmitted light, which is masked at the Fourier plane, defines the asymmetric illumination that is incident on the monolayer of nanospheres and in turn is focused asymmetrically by the PS particles to generate the elliptical-hole pattern in the underlying photoresist. It is important to note here that the orientation of the patterned ellipse is normal to the slit axis (Figure 5.5(c)). To define different regions on the sample with different orientations of ellipses the spatial patterning of the light is is accompanied by rotating the axis of the slit which is mounted on a rotation stage.

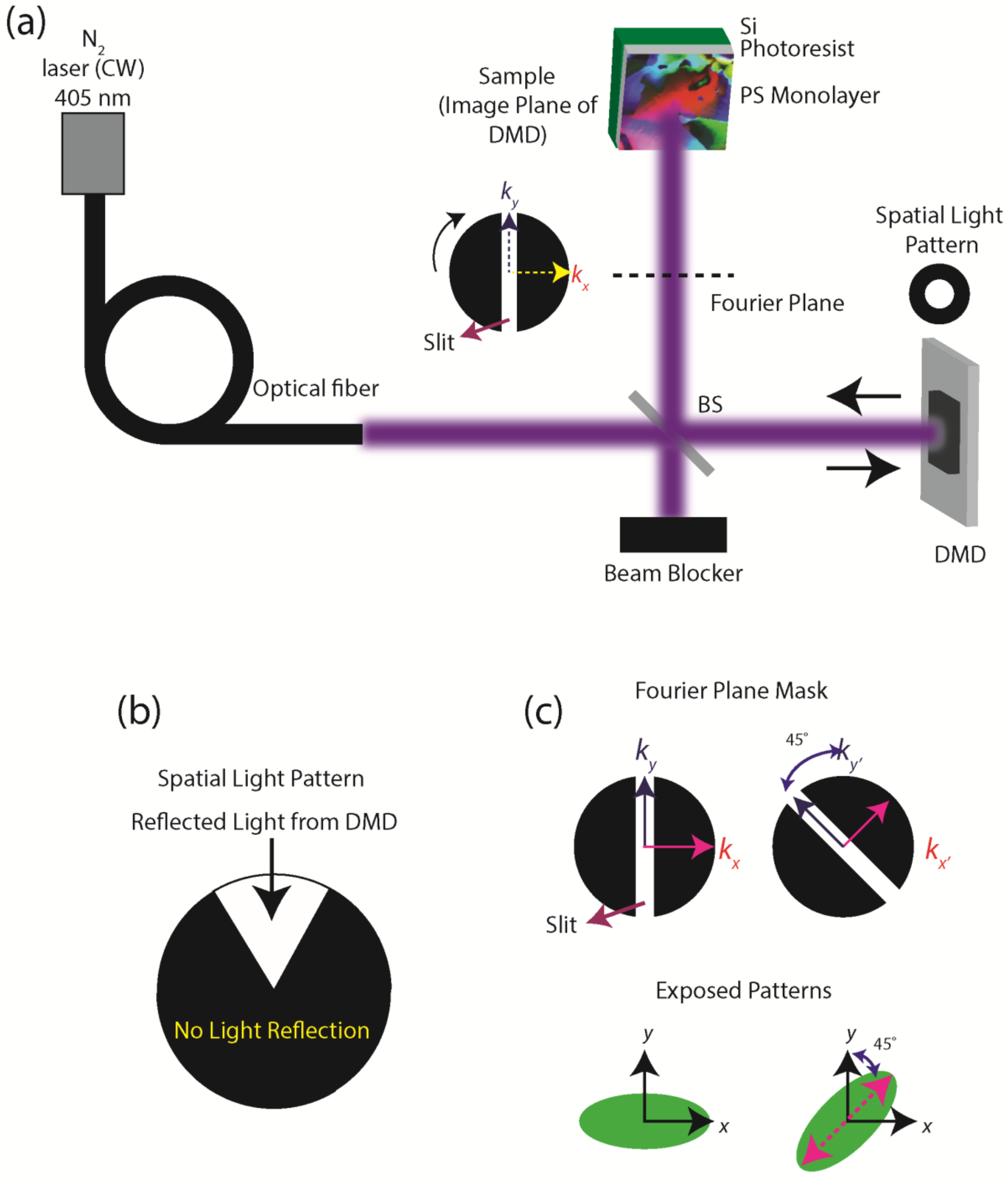

Figure 0.39 (a) Schematic of the optical set-up for gradient patterning using nanosphere lens lithography. (b) Schematic of spatial light pattern. (c) Fourier plane masking to achieve elliptical hole patterns oriented differently.

5.4 Motivation: Metasurfaces

The motivation behind developing the advanced nanosphere photolithography technique is to achieve low cost and high throughput fabrication of metasurfaces that are composed of spatially varying resonators. ‘Metasurfaces’ are planar ultra-thin optical components that provide complete control over the phase of light, opposed to conventional optical elements that solely depend on accumulating phase during propagation over an optical path that is much larger than the wavelength. With complete control of light i.e., spatial phase variation from 0 to 2π, metasurfaces provide a new design methodology that can be used to realize novel ultra-thin optics such as ultrathin planar lenses[121], [122], optical vortex beam generation[123], [124] and holograms[125]–[127]. Metasurfaces typically utilize asymmetric electric dipole resonances to allow 0 to 2π phase control for the cross-polarized light. Initial metasurface work started by utilizing plasmonic antennae, however, one of the drawbacks of plasmonic metasurfaces is that they generally suffer from low efficiency because of weak coupling between incident and cross-polarized fields. In order to increase efficiency, efforts have been made to combine an array of plasmonic nano antennae with a metal ground plane to achieve 80% efficiency for anomalous reflection and linear polarization conversion. However, the use of metallic nano antennae still limits the efficiency because of ohmic loss at optical frequencies. The efficiency for polarization conversion was recently boosted up to 98% over a 200 nm bandwidth in the short infrared band by replacing metallic nano antennas with dielectric nano antennas. This allowed high efficiency optical vortex beam generation over a band from 1500-1600 nm by azimuthally varying the phase of the cross polarized reflected light[65]. Some selected examples of metasurfaces are demonstrated in Figure 5.6.

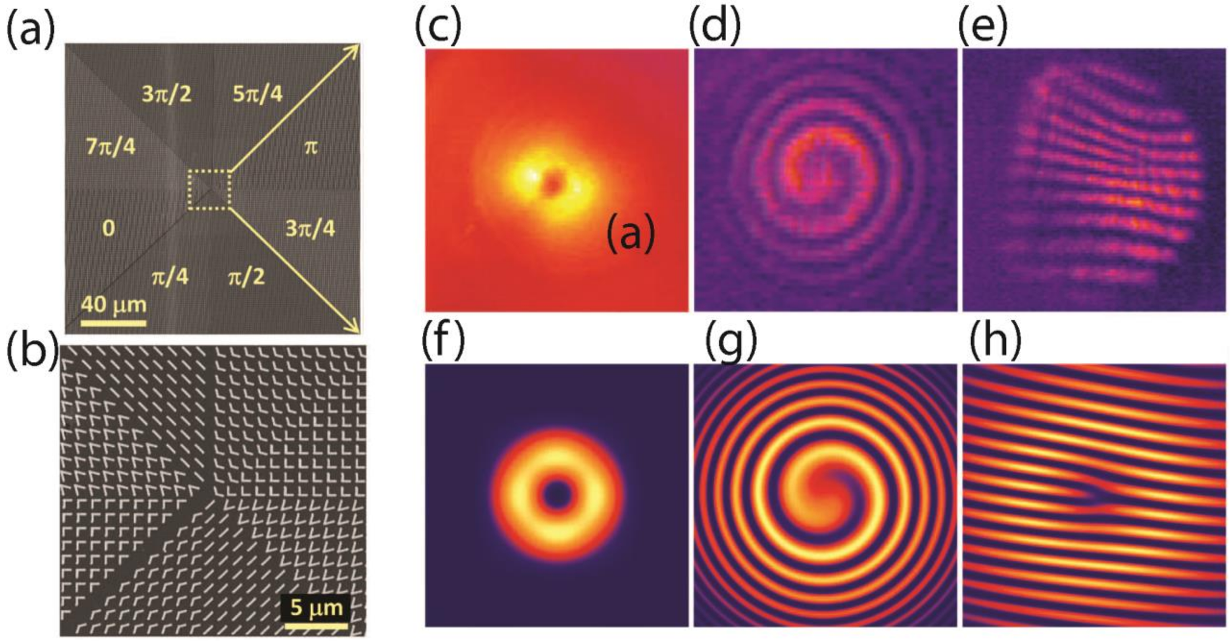

Figure 0.40 Demonstartion of Metasurface utilizing linear cross-polarized transmitted light. (a) SEM image of a plasmonic interface that creates an optical vortex. The plasmonic pattern consists of eight regions, each occupied by one constituent antenna of the eight-element set of Fig. 2F. The antennas are arranged so as to generate a phase shift that varies azimuthally from 0 to 2p, thus producing a helicoidal scattered wavefront. (b) Zoom-in view of the center part of (a). (c and d) Respectively, measured and calculated far-field intensity distributions of an optical vortex with topological charge one. The constant background in (c) is due to the thermal radiation. (e and f) Respectively, measured and calculated spiral patterns created by the interference of the vortex beam and a co-propagating Gaussian beam. (g and h) Respectively, measured and calculated interference patterns with a dislocated fringe created by the interference of the vortex beam and a Gaussian beam when the two are tilted with respect to each other. The circular border of the interference pattern in (g) arises from the finite aperture of the beam splitter used to combine the vortex and the Gaussian beams (20). The size of (c) and (d) is 60mmby 60mm, and that of (e) to (h) is 30 mm by 30 mm. Adapted from reference [123].

5.5 Metasurface Utilizing Pancharatnam-Berry Phase

The type of metasurface that we are interested in exploring here is one that modifies the geometric or Pancharatnam-Berry phase of the incident beam[128][129]. Such surfaces work with circularly polarized light and utilize spatially varying orientations of nanorods[127], [130]. Using our fabrication methodology the spatial orientation of elliptical dielectric cylinders can be controlled, which in turn will lead to control the geometric phase or Phancharatnam-Berry phase acquired through polarization conversion of circularly polarized light. The uniqueness of Pancharatnam-Berry phase is that it is not a function of particular antenna design or material properties and hence possesses a broadband response. Figure 5.6 illustrates metasurfaces utilizing Pancharatnam-Berry phase.

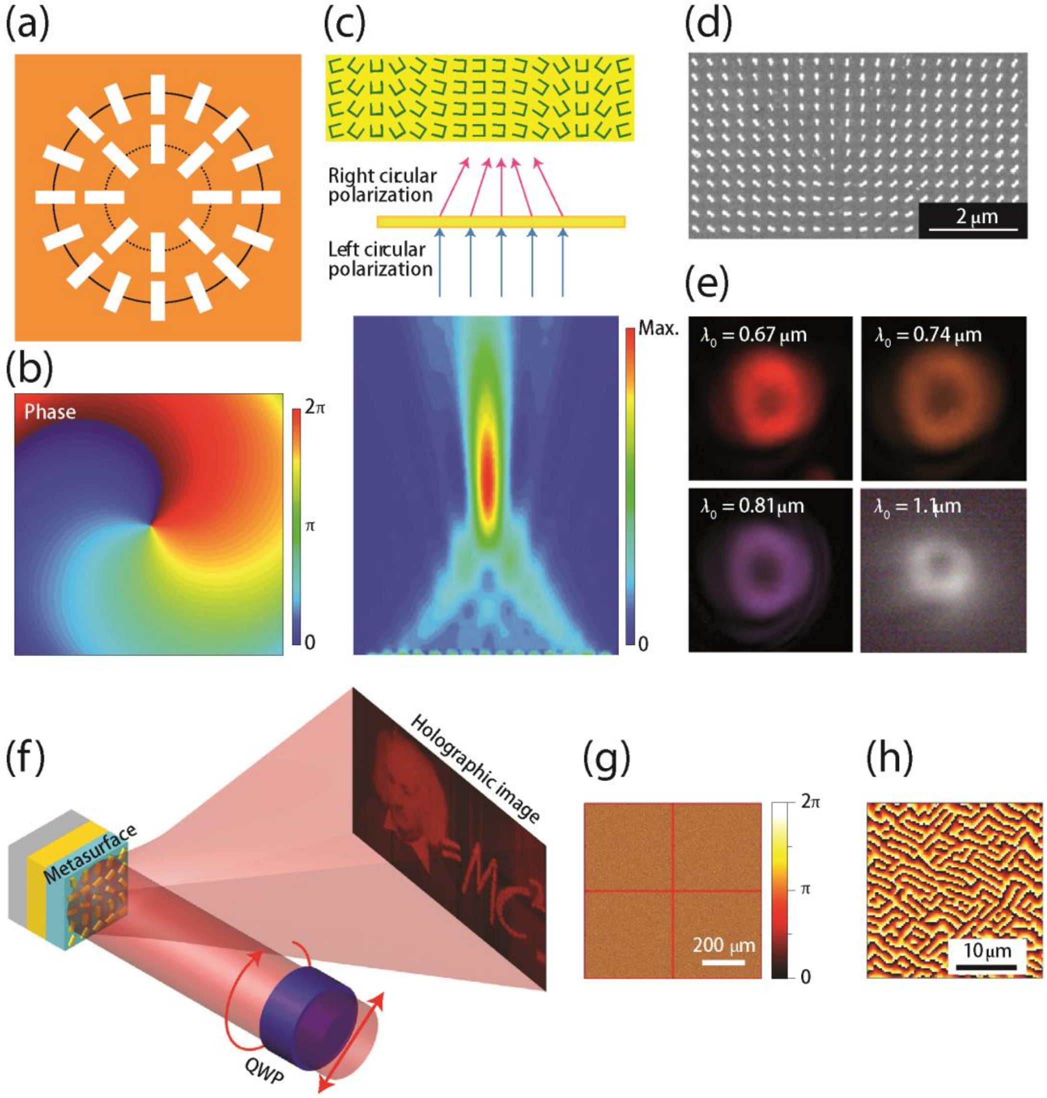

Figure 0.41 Demonstartion of Metasurface utilizing circular cross-polarized light utilizing Pancharatnam-Berry phase. (a) Geometry of a metasurface composed of rectangular apertures defined in a metal film and arranged into an array with rotational symmetry. (b) Simulated phase distribution of the azimuthally polarized transmitted field. Incident light is circularly polarized. (c) Upper panel: Schematic of a planar cylindrical lens consisting of arrays of U-apertures with

different orientations. Lower panel: Schematic and simulation showing that the lens focuses the right-handed circularly polarized (RHCP) component of the transmission when the incident light is left-handed circularly polarized (LHCP). (d) SEM image of a dipolar antenna array designed for generating an optical vortex beam with L = 1 (RHCP incidence/LHCP detection). The antennas have the same geometry but spatially varying orientations. (e) Measured intensity distribution of vortex beams generated by the metasurface in panel d at different wavelengths from 670 to 1,100 nm. (f) Illustration of the reflective nanorod-based computer-generated hologram (CGH) under a circularly polarized incident beam. The circularly polarized incident beam, which is converted from a linearly polarized one by passing through a quarter wave plate (QWP), falls on the metasurface. The reflected beam forms the holographic image in the far field. (g) The 16-level phase distribution with 2 × 2 periods designed to generate the target holographic image in the far field. (h) Enlarged phase distribution (100 × 100 pixels) of the upper-left corner of (g). Adapted from references [131] (a,b), [132] (c), [124] (d,e), [127] (f,g,h).

5.6 Design Methodology

Here, we demonstrate geometric dielectric metasurface reflectarray, consisting of elliptical dielectric cylinders, a dielectric spacer layer, and a metal ground plane. The motivation behind the demonstration of geometric metasurface is the ease in controlling the geometric phase or Pancharatnam-Berry phase simply by controlling the geometric orientation of the elliptical nanorods. The principle that governs the geometric metasurface is that it inverts the direction of the electric field of the incident circularly polarized (CP) light in transmission or reflection[133], [134]. This maintains the polarization direction in reflection (because reflection itself is accompanied by a π phase shift) and inverts the polarization in transmission. A multilayer design is implemented to increase the polarization conversion efficiency[65]. The design rationale is derived from the fact that a circularly polarized beam is completely converted into its cross-polarized counterpart in transmission as it passes through a half-wave plate because of the phase delay of π between its fast and slow axes. To obtain full conversion of one circularly polarized state to another the phase difference in reflection from light linearly polarized along the major and minor axes of the nanorod must be equal to π. Figure 5.7(a) shows that the simulated reflectance from an elliptical Si nanorods array for both polarizations i.e. along major and minor axes of the ellipse is more than 99% while at the same time maintaining a reflection phase difference of π for both polarizations over a broad wavelength range of 1600-1850 nm (Figure 5.7(b)). Hence, irrespective of the orientation of nanorods, this reflectarray acts as a very efficient reflective wave plate which inverts the polarization direction of electric field upon reflection and in turn maintains the handedness of incident circularly polarized light. We note here for future reference that the reflected light that maintains the handedness of the incident beam will be referred to as cross-polarized and that of the opposite handedness will be referred to as co-polarized. This convention is followed because CP light goes through inversion of the polarization state upon normal reflection i.e. left-handed polarized light converts to right handed polarized light and vice-versa.

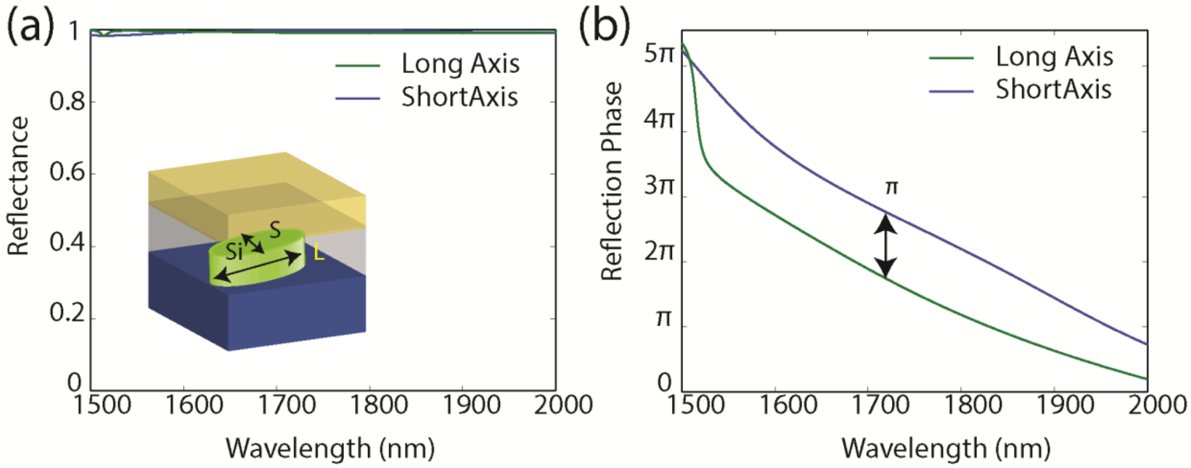

Figure 0.42 (a) Reflectances from an array of elliptical cylinder resonators with electric field polarized along long and short axes, respectively. (b) Reflection phase plot demonstrating π phase difference between reflections from two linear polarizations for 200 nm broad bandwidth.

While the polarization conversion of circularly polarized light can be achieved irrespective of the orientation of the elliptical nanorods in the reflectarray, a geometric phase or Pancharatnam– Berry phase, which is acquired upon cross-polarized reflection, can offer complete phase control from 0 to 2π by changing the orientation of the nanorods. The efficient control of the phase of light utilizing geometric phase is the key feature of the geometric metasurface reflectarray. Figure 5.8(b) shows that our design maintains broadband cross-polarized reflectance over 99% from 1600-1850 nm as a function of the orientation angle of (θ) of the elliptical cylinder resonators. The transformation of circular polarization is accompanied by a geometric phase change of $\varphi=2\theta$, where θ is the orientation angle of nanorods[135][127]. Hence, by changing the orientation angle of the elliptical cylinder resonators from 0 to 180 degrees, a complete sweep of 0 to 2π phase can be obtained in the cross-polarized light. The simulated reflection phase (Figure 5.8(c)) as a function of angle for broad wavelength range of 1600-1850 nm confirms this.

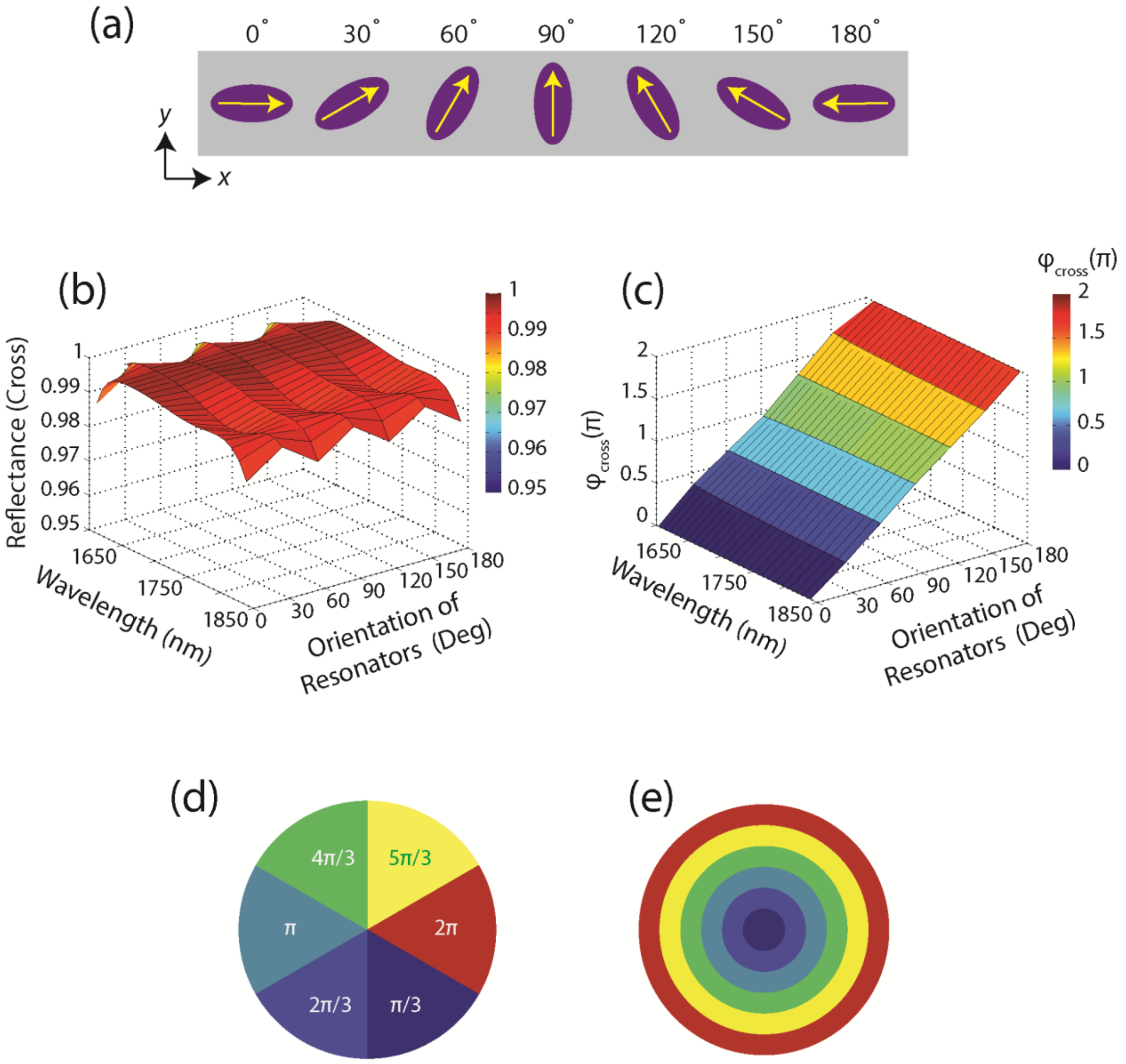

Optical Vortex Generator

Axicon

Figure 0.43 (a) Schematic of elliptical patterns with different orientations. (b) Broadband cross-polarized reflectance as a function of orientation of resonators. (c) Broadband cross-polarized reflection phase as a function of orientation of resonators. Complete phase control from 0 to 2π is demonstrated for over 200 nm bandwidth. (d,e) Phase profiles for optical vortex generator and axicon, respectively.

5.7 Practical Implementation

The first step in the fabrication of an asymmetric dielectric meta-reflectarray is the deposition of 400 nm of high density amorphous Si on quartz substrate using low pressure chemical vapor deposition (LPCVD) furnace. The substrate is then diced to 20mm X 20 mm sized samples. The sample is spin-coated at 6000 rpm with diluted AZ5214 photoresist which is diluted with equal volume of solvent (AZ EBR) to get 500 nm thin photoresist layer. The photoresist is soft baked at 95° C and immersed in MIF 316 solution to provide hydrophilicity to the surface, which helps in the self-assembly of PS monolayer on the photoresist film. The same procedure as described in the previous chapter is used in the process of self-assembly and pattern transfer on the substrate. AZ5214 is sensitive to both i-(~365 nm) and h-line (~405 nm) exposure. Here, we utilize the h-line exposure (405 nm) because of the optimized working wavelength of 400-700 nm for the DMD and also for the availability of laser source. After the exposure, the polystyrene particles are removed by sonication of the sample in DI water. The photoresist is developed with MIF 316 developer which reveals the elliptical-hole arrays.

The remainder of the fabrication follows the conventional lift-off process to metallize the elliptical mask followed by reactive ion etching (RIE) of the underlying silicon. 250 nm PMMA is then spin-coated on the sample, followed by soft baking (180 degrees for 2 minutes) and reflowing at 300° C for 2 minutes to reach the desired thickness and flatness. In the last step, 150 nm of silver is thermally deposited on top of the sample, serving as the ground metal plane. The entire process is summarized in Figure 5.5.

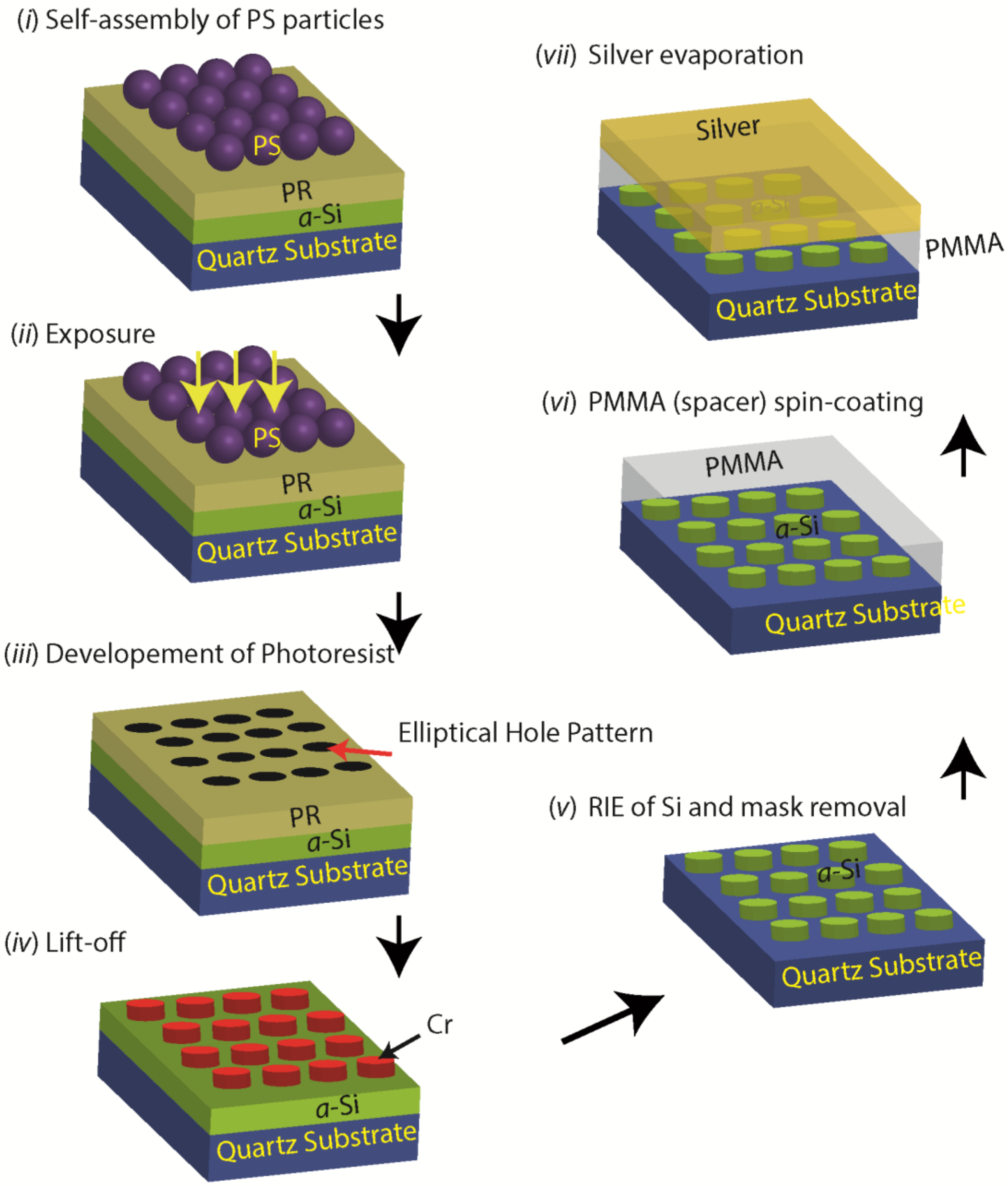

Figure 0.44 Schematic of fabrication process flow.

5.8 Future Demonstrations

The two most important parameters to create a metasurface are complete 0 to 2π phase control and efficient conversion of polarization. In our design we have demonstrated over 99% efficiency in polarization conversion along with complete phase control using a dielectric meta-reflectarray. With the advanced lithography technique outlined in this chapter the fabrication of different metasurfaces such as lenses, axicons, optical vortex generators or phase holograms will be greatly simplified and expedited with at the same time cost of fabrication will be highly reduced. However, the experimental demonstration of such a metasurface is not within the scope of this dissertation and will be explored in detail in future work.

5.9 Conclusion

Here, we demonstrated the idea of a novel lithography approach that combines asymmetric pattern generation with the spatial control of resonator orientation using spatial light patterning using a DMD. The overall lithography set-up is simple and should result in high throughput fabrication of metasurfaces. Moreover, in addition to controlling the orientation of the patterns the size of the pattern can also be controlled spatially by controlling the intensity of the incident light using grayscale masking. Better control over resonator size can also be implemented by controlling the Fourier plane masking. We believe that the demonstration of a simple, low-cost and high-throughput gradient lithography technique will lead to the implementation of metasurfaces for practical applications.

Chapter 6

Conclusion and Future Outlook

6.1 Conclusion

The advent of metamaterial research started with the use of metal based unit cells[1][18] and many interesting demonstrations have followed including negative index of refraction[25]–[27], ultra-high index[8], epsilon near zero[5]–[7], [136], electromagnetically induced transparency[137]–[144], chirality[145]–[148], nonlinearity[149]–[155], magnetic mirrors[97], and spatial control of phase [72], [123], [125], [127], [156]. However, at optical frequencies the path towards further improvement using metal based metamaterials face immense challenges mostly because of parasitic loss due to absorption. Secondly, with scaling to high frequencies dimensions of the unit cells gets extremely small and the intricate unit cell designs prohibit large area scalability due to the need for expensive patterning equipment. Thirdly, the intricate unit cell designs also render the optical properties anisotropic. While metal based designs served well to understand the physics of metamaterials, the search for alternative approaches is now in full swing. Dielectric metamaterials are excellent alternatives which address all the challenges faced by metal based metamaterials. Dielectric materials are lossless at optical frequencies and exhibit electric and magnetic dipole Mie resonances with very simple and isotropic resonator geometries, which, in turn, can result in an isotropic optical response. Finally, due to simple resonator designs dielectric metamaterials offer large area scalability with simple, low cost, and expedited lithography processes. The purpose of my research has been to take advantage of all these interesting features and hopefully contribute to advancing this field of study.

In Chapter 2, I experimentally demonstrated zero-index-metamaterial with multilayered design at optical frequencies[81]. A proper design methodology has been followed to achieve Dirac cone like dispersion in band diagram of a square lattice of dielectric (Si) rods with square cross section. Effective metamaterial properties have been retrieved to demonstrate impedance matched zero index of refraction. Rigorous fabrication challenges were overcome to achieve uniform resonator dimensions in the direction normal to the plane of substrate. Finally, zero index of refraction was experimentally demonstrated with directional transmission and directional enhanced emission from quantum dots from inside the ZIM.

In Chapter 3, I explored the advantage of using dielectric (Si) cylinder unit cell as it offers control over spectral manipulation of electric and magnetic resonances. With optimized design, I was able to demonstrate broadband perfect reflection from sub-wavelength single layer metamaterial formed from ordered and disordered arrays of Si cylinders[95][157]. Because of the simple unit cell design, this research leads to the farther demonstration of perfect reflection from large area using low cost and high throughput fabrication technique for practical applications.

In Chapter 4, I scaled the metamaterial perfect reflector to large area (centimeter size). To fabricate large area metamaterial, I developed a modified nanosphere lithography technique with self-assembly of polystyrene particles which forms a highly close packed monolayer. The size of the polystyrene particles is then reduced using isotropic oxygen plasma etching and the downscaled polystyrene particles are used as mask for subsequent reactive ion etching of silicon. The influence of disorder in the lattice imparted by the self-assembly process, on reflection was studied at electric and magnetic modes. It was found that reflection at magnetic modes is more tolerant to that of electric modes. This was because of the fact that magnetic mode is more confined in the resonators than the electric modes and disorder does not influence the optical response at magnetic mode. I farther proposed a mechanism and demonstrated that with increasing aspect ratio the electric mode can also be confined inside the resonators which will lead to high reflectance at electric mode and can be used to achieve broadband reflectance. Finally, a design is numerically proposed for achieving magnetic mirror at optical frequencies, which can be fabricated conveniently in large area with the present capability.

In Chapter 5, the perspective of advancement of nanosphere lithography is discussed which can lead to achieve gradient metasurface with spatially varying resonator sizes and orientations. The key to achieve this advanced nanosphere photolithography technique is to first spatially pattern light using a digital micro-mirror device (DMD) which is imaged at the sample and second, controlling the wave vector of light at the Fourier plane for asymmetric light illumination at the sample. Spatial patterned light defines the pixel locations on the sample while orientation of rectangular slit at the Fourier plane controls the orientation of the elliptical-hole pattern in the photoresist. The asymmetric light incident leads to asymmetric focal spot on the photoresist and in turn leads to formation of elliptical-hole pattern.

6.2 Future Outlook

2015 is being celebrated as the International Year of Light. As a researcher in optical metamaterials I take pride in the contributions that metamaterials research has made in the advancement of the fields of photonics and plasmonics. Still, there is a long and bumpy road ahead for metamaterials that requires further research advances. Here, I will briefly describe the major challenges that can be addressed by advancing the future research in the direction of my dissertation work.

The performance of all-dielectric metamaterials can be greatly improved at telecommunication wavelengths if the dielectric permittivity of the constituent material is high, because of stronger and more confined dipole resonances and sub-wavelength unit cell geometries. Silicon serves as the most suitable material in this wavelength range because of its comparatively high permittivity ($\varepsilon \sim 12$) and low loss. However, it should be actively pursued to develop a metamaterial which has low-loss and high effective permittivity, ε_{eff} (much higher than ε of silicon). This artificial high permittivity metamaterial with low-loss would serve as an ideal constituent to further develop a "Meta-Metamaterial" design, i.e. a metamaterial which is composed of unit cells made of homogeneous metamaterials. Though the idea may sound a little far-fetched, the motivation can be derived from experimental demonstration of high-permittivity metamaterials in THz wavelengths[8].

Another interesting area for advancement is the active tunability of silicon based metamaterial properties at telecommunication wavelengths. This can be achieved with the thermo-optic and electro-optic effects in silicon i.e. changing index of refraction of silicon as a function of an increase in temperature[158] or electric field[159]. These effects has been experimentally demonstrated for silicon based waveguides[160]–[163]. Experimental demonstration of the tunability of resonances of silicon resonator based dielectric metamaterials is yet to be done and is subject to future study.

Finally, for practical applications and commercialization of metamaterials, development of a cost-effective well-ordered large area fabrication with minimum defect is essential.

Appendix

A.1 Retrieval of Effective Index from Bloch Modes

Retrieval of the permittivity and permeability was carried out by extracting the average field components from the TM Bloch modes at the boundary of the unit cell $\left(\bar{E}_x, \bar{D}_x, \bar{H}_y, \bar{B}_y, \bar{H}_z, \bar{B}_z\right)$. In the extraction of the permittivity and permeability, we ensure the continuity of the tangential and normal components of the average field at the unit cell boundary, ensuring that Maxwell's equations are satisfied. The constitutive equations for the average fields are then given by,

$$\begin{bmatrix} \bar{D}_x \\ \bar{B}_y \\ \bar{B}_z \end{bmatrix} = \begin{bmatrix} \varepsilon_0 * \varepsilon_x & A_{xy} & A_{xz} \\ A_{yx} & \mu_0 * \mu_y & A_{yz} \\ A_{zx} & A_{zy} & \mu_0 * \mu_z \end{bmatrix} \begin{bmatrix} \bar{E}_x \\ \bar{H}_y \\ \bar{H}_z \end{bmatrix} \tag{A.1}$$

The diagonal elements of the 3 x 3 parameter tensor define the permittivity (ε_x) and permeability (μ_y, μ_z) of the bulk structure along the *x*, *y* and *z* directions respectively.

A.2 Optical Property Retrieval from Bloch Modes and Extended States

To ensure that an accurate retrieval of the material properties was acquired, we compared the retrieved wavevector, computed with the retrieved effective index, to the band structure calculated numerically using MIT Photonic Bands (MPB) in the range from Γ to X, as illustrated in Figure A.1(a). The retrieved band structure has a very good agreement with the MPB band structure at smaller k_y, though it deviates at large k_y as spatial dispersion becomes apparent near the band edge. Only the transverse bands are considered in the calculation of the effective optical properties.

In order to properly assign a refractive index to a material for off-normal angles of incidence, there must be only one propagating band at a particular frequency. To verify that there is only one propagating band within the material, we simulated the extended states of the crystal, shown in Figure A.1(b). Within the frequency range from 215 THz to 225 THz, slightly above the zero-index point, there is a single band (TM4) throughout k-space. Within this region, a refractive index may be assigned to the metamaterial, though it may change slightly with the angle of incidence, as illustrated in the IFC plot shown in Figure 2.1(c).

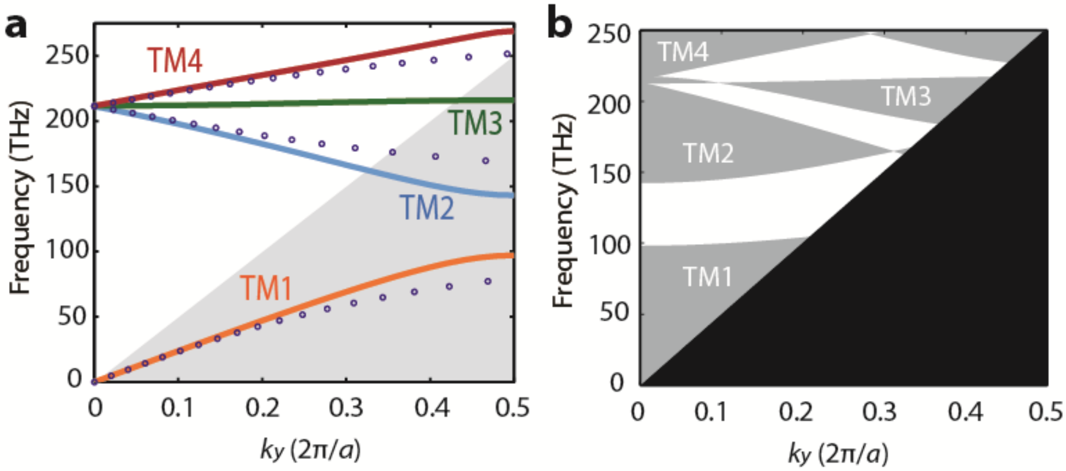

Figure A. 1 Comparison of optical properties and band structure and extended states of the metamaterial. a, The solid lines represent the band structure of the square lattice calculated from MPB and the circles correspond to band diagram retrieved from effective index n_{eff} and the dispersion relation $k_y = n_{eff}\,\omega/c$. The mismatch of the two methods at the band edge is due to the fact that the effective medium approximation no longer holds in those regions. b, Extended states of the crystal showing that only one band (TM4) is present between 215 THz and 225 THz, allowing an effective index to be assigned to this region.

A.3 Comparison of Normal and Angle Dependent Transmission from ZIM and Homogeneous Media

To verify the use of effective constitutive properties in the case of the ZIM, we also simulated normal and angle dependent transmission of a homogeneous medium with the same effective optical properties. The ZIM structure that was simulated consisted of 5 identical unit cells along the light propagation direction and the homogenous medium it was compared to was modeled with the optical properties acquired from the bulk metamaterial retrieval (Figure 2.1(b)). In Figure A.2(a) and A.2(c), we compare the transmittance at normal incidence for the effective medium and ZIM, respectively. Transmittance for both cases stays near unity over the wavelength range of 1200 nm to 1600 nm, with some undulation in transmission occurring in the case of the ZIM. This undulation can be attributed to the limited thickness of the material and thus the optical properties have not fully converged to the bulk case. In Figure A.2(b) and A.2(d), the transmittance with respect to angle of incidence is plotted for the homogenous medium and the ZIM at the wavelengths of 1340 nm (n = 0.254) and 1380 nm (n = 0.121). These wavelengths lie within the frequency region where only a single band (TM4) exists. The close match between the results supports the assignment of effective optical properties to the ZIM.

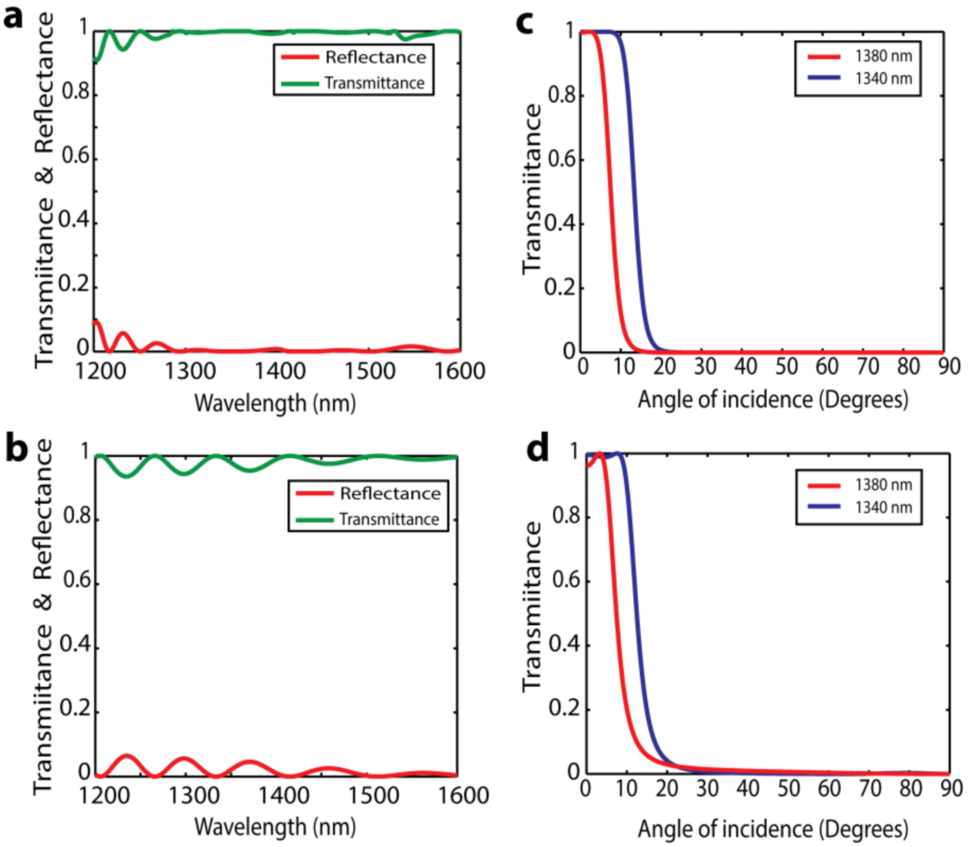

Figure A. 2 Comparison of normal and angle dependent transmittance of a homogeneous medium and the ZIM structure. a,c, Transmittance of the homogeneous medium and ZIM structure (5 periods), respectively, under normal incidence. b,d, Angle dependent transmittance of the homogeneous medium and ZIM structure, respectively, at wavelengths of 1340 nm and 1380 nm.

A.4 Homogeneous Effective Materials Properties

To further justify our claim that the proposed metamaterial structure can indeed be homogenized as an effective medium and has an isotropic low index property for TM-polarized light, we conducted numerical simulation with a Gaussian beam incident at the ZIM from multiple angles. The wavelengths of the incident beams (1340nm and 1380nm) are chosen such that they fall within the bandwidth where only one propagating band (TM4) exists.

The simulated electric field profiles with multiple angles of incidence and wavelengths are shown in Figures A.3(a-f). In all cases, we see no higher order diffraction taking place at the exit surface of the sample. The transmitted light from the material is plane wave like as shown in Figures A.3(a,b,d,e) for normal and low angle incidence, while light transmission is clearly forbidden at even higher angles of incidence due to the conservation of parallel angular momentum (Figures A.3(c,f)).

From the field plots in Figure A.3(b), with 10° incidence at 1340 nm, the light refracts at an angle of ~ 43° with clearly longer effective wavelength inside the material. From simple calculation from Snell's law we find the corresponding n_{eff} agrees well with retrieved index of 0.254. The same phenomenon occurs with 5° incidence at 1380 nm where the refraction angle is ~ 46°, which corresponds to a n_{eff} of 0.121 and again matches our parameter retrieval result.

In Figures A.3(g-i), we illustrated the refraction phenomenon at 1458 nm which is negative index region where calculated index is -0.121, i.e. the same absolute value of index for 1380 nm wavelength. With 0° angle of incidence the light transmits normally out of the material with plane wave profile. With 5° incidence we can clearly see the negative phase propagation inside the medium, finally light transmitting out of the exit surface at 5° from the normal. But contrary to the refraction phenomenon at 1380 nm, refraction is not forbidden at 30º angle of incidence for 1458 nm wavelength, due to coupling to the longitudinal band at higher angle.

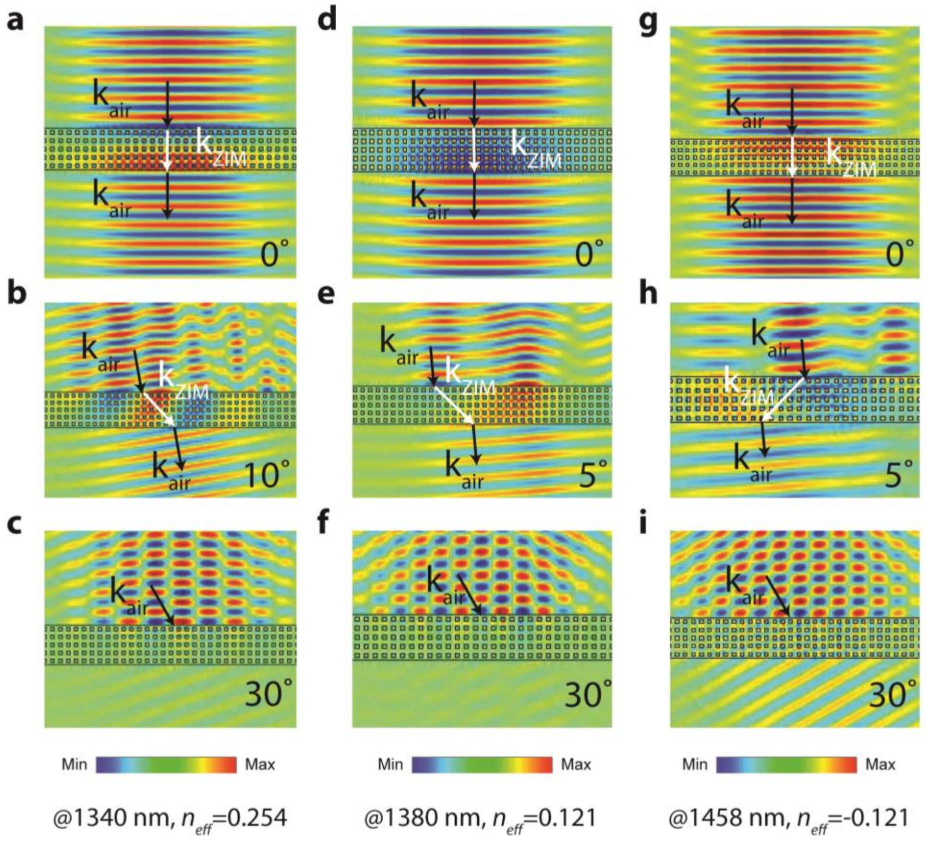

@1340 nm, n_{eff}=0.254 @1380 nm, n_{eff}=0.121 @1458 nm, n_{eff}=-0.121

Figure A. 3 Simulated electric field plot of uniform periodic 5 layered ZIM probed with a Gaussian beam. a-c, Light incidence at 0°, 10°, 30° respectively at wavelength of 1340 nm. d-f, Light incidence at 0°, 5°, 20° respectively at wavelength of 1380 nm. g-i, Light incidence at 0°, 5°, 20° respectively at wavelength of 1458 nm.

A.5 Comparison of Dispersion Relation and Effective Optical Properties as a Function of Si Rod Filling Fraction

We compared the dispersion relations and corresponding effective optical properties of the bulk ZIM as a function of the Si filling fraction to identify changes that could arise due to fabrication imperfections. Figures A.4(a,c) show the band diagram with the Si filling fraction set at smaller (0.400) and larger (0.500) values than the zero-index case (0.433,Figure A.4(b)). With deviated filling fraction, the triple-degeneracy at the Γ point breaks up and the dispersion of two transverse bands changes from linear to quadratic. A bandgap opens between the two transverse modes, leading to a discontinuity in the effective optical properties as well as impedance mismatch at the band edge, as shown in Figure A.4(d) and Figure A.4(f). A similar effect is present in the fabricated structure due to non-uniform Si rod size.

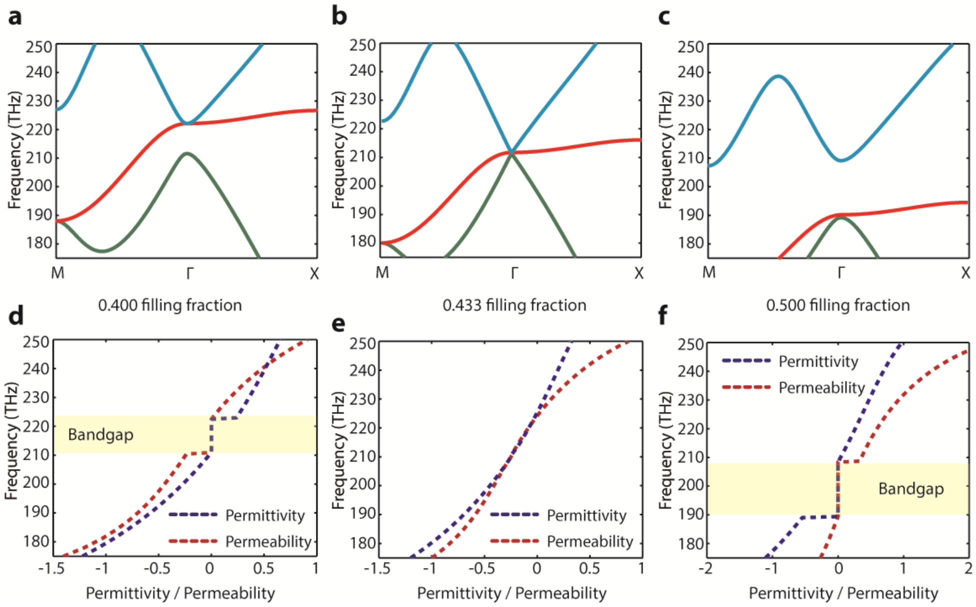

Figure A. 4 Band diagram and parameter retrieval for three different filling fractions. a-c, Band diagram of a square lattice with Si filling fraction of, a 0.400, b 0.433, c 0.500. The lattice constant is 600 nm, with $\varepsilon_{Si} = 13.7$, $\varepsilon_{SiO_2} = 2.25$. d-f, Corresponding retrieved optical properties of the bulk material using field averaging. A bandgap appears when the Si filling fraction deviates from the ideal design. In this case, at the band edge where index is low, the permittivity and permeability no longer match each other, leading to impedance mismatch to free space.

A.6 Characterization of Disorder

Here, we provide the lattice positions of the resonators composing the disordered metamaterials shown in Figures 3.5(a-e) as well as the percentage of disorder. The disorder in the lattice has been realized by placing the resonators in 2 x 2 and 3 x 3 resonator super cells and off-setting the resonators' *x* and *y* positions from a nominal spacing of 660 nm.

The percentage disorder in the different lattices is characterized by taking the standard deviation of the distances between the 4 nearest neighbors to each resonator and normalizing the standard deviation by the period of the perfectly ordered lattice (Fig. S2). With this approach, a higher disorder represents a larger offset in the resonator position from its location in the perfectly ordered lattice.

Table A.1 Resonator positions of the disordered metamaterials

Figure	**Supercell**	**x (µm)**	**y (µm)**	**Periodicity (µm)**	**Percent Disorder**
4a	2 x 2	-0.264	0.404	1.36	6 %
		0.354	0.234		
		-0.380	-0.245		
		0.267	-0.406		
4b	2 x 2	-0.241	0.374	1.36	9 %
		0.354	0.234		
		-0.322	-0.231		
		0.357	-0.425		
4c	2 x 2	-0.231	0.33	1.36	15 %
		0.295	0.237		
		-0.255	-0.265		
		0.32	-0.428		
4d	2 x 2	-0.274	0.412	1.36	15 %
		0.231	0.332		
		-0.267	-0.253		
		0.371	-0.420		
4e	3x3	-0.561	0.6	2.04	17 %
		-0.035	0.567		
		0.735	0.725		
		-0.670	-0.098		
		0.056	0.082		
		0.561	0.002		
		-0.597	-0.583		
		0.0413	-0.75		
		0.726	-0.586		

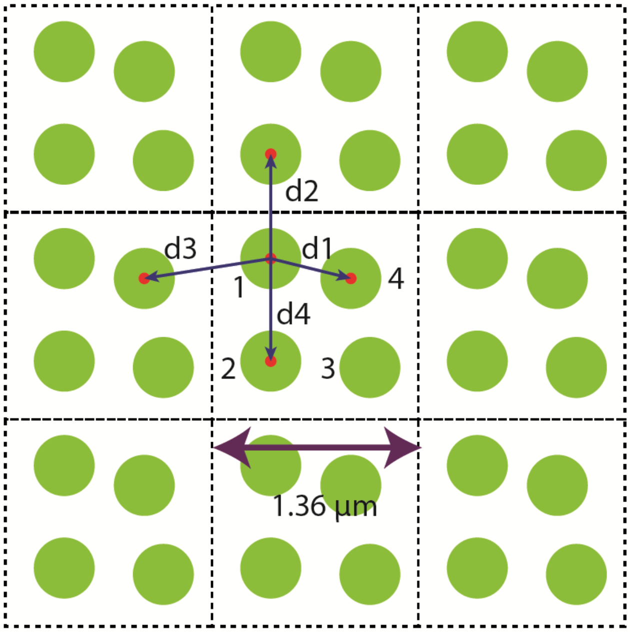

Figure A. 5 Schematic of a disordered lattice and the 4 nearest neighbor distances for one of the resonators. These distances were used to compute the standard deviation in the resonator positions from their perfectly periodic arrangement in the computation of percent disorder shown in Table A.1.

Bibliography

[1] R. A. Shelby, D. R. Smith, and S. Schultz, “Experimental verification of a negative index of refraction.,” *Science*, vol. 292, pp. 77–79, 2001.

[2] S. Zhang, W. Fan, N. C. Panoiu, K. J. Malloy, R. M. Osgood, and S. R. J. Brueck, “Experimental demonstration of near-infrared negative-index metamaterials.,” *Phys. Rev. Lett.*, vol. 95, p. 137404, 2005.

[3] V. M. Shalaev, W. Cai, U. K. Chettiar, H.-K. Yuan, A. K. Sarychev, V. P. Drachev, and A. V Kildishev, “Negative index of refraction in optical metamaterials.,” *Opt. Lett.*, vol. 30, pp. 3356–3358, 2005.

[4] J. Valentine, S. Zhang, T. Zentgraf, E. Ulin-Avila, D. A. Genov, G. Bartal, and X. Zhang, “Three-dimensional optical metamaterial with a negative refractive index.,” *Nature*, vol. 455, no. 7211, pp. 376–9, Sep. 2008.

[5] A. Alù, M. Silveirinha, A. Salandrino, and N. Engheta, “Epsilon-near-zero metamaterials and electromagnetic sources: Tailoring the radiation phase pattern,” *Phys. Rev. B*, vol. 75, no. 15, p. 155410, Apr. 2007.

[6] R. Liu, Q. Cheng, T. Hand, J. J. Mock, T. J. Cui, S. A. Cummer, and D. R. Smith, “Experimental demonstration of electromagnetic tunneling through an epsilon-near-zero metamaterial at microwave frequencies.,” *Phys. Rev. Lett.*, vol. 100, p. 023903, 2008.

[7] M. Silveirinha and N. Engheta, “Tunneling of electromagnetic energy through subwavelength channels and bends using epsilon-near-zero materials.,” *Phys. Rev. Lett.*, vol. 97, p. 157403, 2006.

[8] M. Choi, S. H. Lee, Y. Kim, S. B. Kang, J. Shin, M. H. Kwak, K.-Y. Kang, Y.-H. Lee, N. Park, and B. Min, “A terahertz metamaterial with unnaturally high refractive index.,” *Nature*, vol. 470, no. 7334, pp. 369–73, Feb. 2011.

[9] J. B. Pendry, “Negative Refraction Makes a Perfect Lens,” *Physical Review Letters*, vol. 85. pp. 3966–3969, 2000.

[10] N. Fang, H. Lee, C. Sun, and X. Zhang, “Sub-diffraction-limited optical imaging with a silver superlens.,” *Science*, vol. 308, pp. 534–537, 2005.

[11] J. B. Pendry, D. Schurig, and D. R. Smith, “Controlling electromagnetic fields.,” *Science*, vol. 312, pp. 1780–1782, 2006.

[12] D. Schurig, J. J. Mock, B. J. Justice, S. A. Cummer, J. B. Pendry, A. F. Starr, and D. R. Smith, “Metamaterial electromagnetic cloak at microwave frequencies.,” *Science*, vol. 314, pp. 977–980, 2006.

[13] J. Valentine, J. Li, T. Zentgraf, G. Bartal, and X. Zhang, “An optical cloak made of dielectrics.,” *Nat. Mater.*, vol. 8, no. 7, pp. 568–71, Jul. 2009.

[14] A. Boltasseva and H. A. Atwater, “Materials science. Low-loss plasmonic metamaterials.,” *Science (80-.).*, vol. 331, no. 6015, pp. 290–1, Jan. 2011.

[15] N. I. Zheludev, “Applied physics. The road ahead for metamaterials.,” *Science (80-.).*, vol. 328, no. 5978, pp. 582–583, Apr. 2010.

[16] C. M. Soukoulis and M. Wegener, “Past achievements and future challenges in the development of three-dimensional photonic metamaterials,” *Nat. Photonics*, vol. 5, no. 9, pp. 523–530, Jul. 2011.

[17] J. Zhou, T. Koschny, M. Kafesaki, E. N. Economou, J. B. Pendry, and C. M. Soukoulis, “Saturation of the Magnetic Response of Split-Ring Resonators at Optical Frequencies,” *Phys. Rev. Lett.*, vol. 95, no. 22, p. 223902, Nov. 2005.

[18] D. Smith, W. Padilla, D. Vier, S. Nemat-Nasser, and S. Schultz, “Composite Medium with Simultaneously Negative Permeability and Permittivity,” *Phys. Rev. Lett.*, vol. 84, no. 18, pp. 4184–4187, May 2000.

[19] H. C. van de Hulst, *Light Scattering by Small Particles*. Courier Dover Publications, 2012, p. 470.

[20] C. M. Soukoulis and M. Wegener, “Past achievements and future challenges in the development of three-dimensional photonic metamaterials,” *Nat. Photonics*, vol. 5, no. 9, pp. 523–530, Jul. 2011.

[21] Y. Liu and X. Zhang, “Metamaterials: a new frontier of science and technology.,” *Chem. Soc. Rev.*, vol. 40, no. 5, pp. 2494–507, May 2011.

[22] V. G. Veselago, “The electrodynamics of substances with simultaneously negative values of ε and μ,” *Sov. Phys. Uspekhi*, vol. 10, pp. 509–514, 1968.

[23] J. Pendry, A. Holden, W. Stewart, and I. Youngs, “Extremely Low Frequency Plasmons in Metallic Mesostructures,” *Phys. Rev. Lett.*, vol. 76, no. 25, pp. 4773–4776, Jun. 1996.

[24] J. B. Pendry, A. J. Holden, D. J. Robbins, and W. J. Stewart, “Magnetism from conductors and enhanced nonlinear phenomena,” *IEEE Trans. Microw. Theory Tech.*, vol. 47, 1999.

[25] C. García-Meca, R. Ortuño, F. J. Rodríguez-Fortuño, J. Martí, and A. Martínez, “Double-negative polarization-independent fishnet metamaterial in the visible spectrum,” *Opt. Lett.*, vol. 34, no. 10, p. 1603, May 2009.

[26] J. Valentine, S. Zhang, T. Zentgraf, E. Ulin-Avila, D. A. Genov, G. Bartal, and X. Zhang, “Three-dimensional optical metamaterial with a negative refractive index.,” *Nature*, vol. 455, pp. 376–379, 2008.

[27] C. García-Meca, J. Hurtado, J. Martí, A. Martínez, W. Dickson, and A. V. Zayats, “Low-Loss Multilayered Metamaterial Exhibiting a Negative Index of Refraction at Visible Wavelengths,” *Phys. Rev. Lett.*, vol. 106, no. 6, p. 067402, Feb. 2011.

[28] V. M. Shalaev, “Optical negative-index metamaterials,” *Nat. Photonics*, vol. 1, no. 1, pp. 41–48, 2007.

[29] L. Peng, L. Ran, H. Chen, H. Zhang, J. A. Kong, and T. M. Grzegorczyk, “Experimental observation of left-handed behavior in an array of standard dielectric resonators.,” *Phys. Rev. Lett.*, vol. 98, p. 157403, 2007.

[30] L. Lewin, “The electrical constants of a material loaded with spherical particles,” *J. Inst. Electr. Eng. III Radio Commun. Eng.*, vol. 94, pp. 65–68, 1947.

[31] S. O’Brien and J. B. Pendry, “Photonic band-gap effects and magnetic activity in dielectric composites,” *Journal of Physics: Condensed Matter*, vol. 14. pp. 4035–4044, 2002.

[32] B. Ai, Y. Yu, H. Möhwald, L. Wang, and G. Zhang, “Resonant optical transmission through topologically continuous films.,” *ACS Nano*, vol. 8, no. 2, pp. 1566–75, Feb. 2014.

[33] B. Ai, Y. Yu, H. Möhwald, and G. Zhang, “Novel 3D Au nanohole arrays with outstanding optical properties.,” *Nanotechnology*, vol. 24, no. 3, p. 035303, Jan. 2013.

[34] S. J. Barcelo, S. Lam, G. A. Gibson, X. Sheng, and D. Henze, “Nanosphere lithography based technique for fabrication of large area , well ordered metal particle arrays Abstract : Nanosphere lithography based technique for fabrication of large area , well ordered metal particle arrays,” 2012.

[35] S. L. Cheng, C. Y. Chen, and S. W. Lee, “Kinetic investigation of the electrochemical synthesis of vertically-aligned periodic arrays of silicon nanorods on (001)Si substrate,” *Thin Solid Films*, vol. 518, no. 6, pp. S190–S195, Jan. 2010.

[36] C. Geng, L. Zheng, J. Yu, Q. Yan, X. Wang, G. Shen, and D. Shen, “Monolayer colloidal mask with tunable interstice size for nanosphere lithography,” *Thin Solid Films*, vol. 544, pp. 83–87, Oct. 2013.

[37] K. Kempa, B. Kimball, J. Rybczynski, Z. P. Huang, P. F. Wu, D. Steeves, M. Sennett, M. Giersig, D. V. G. L. N. Rao, D. L. Carnahan, D. Z. Wang, J. Y. Lao, W. Z. Li, and Z. F. Ren, "Photonic Crystals Based on Periodic Arrays of Aligned Carbon Nanotubes," *Nano Lett.*, vol. 3, no. 1, pp. 13–18, Jan. 2003.

[38] P.-C. Li and E. T. Yu, "Large-area omnidirectional antireflection coating on low-index materials," *J. Opt. Soc. Am. B*, vol. 30, no. 10, p. 2584, Sep. 2013.

[39] P.-C. Li and E. T. Yu, "Flexible, low-loss, large-area, wide-angle, wavelength-selective plasmonic multilayer metasurface," *J. Appl. Phys.*, vol. 114, no. 13, p. 133104, Oct. 2013.

[40] X. H. Li, P. C. Li, D. Z. Hu, D. M. Schaadt, and E. T. Yu, "Angular dependence of light trapping in In0.3Ga0.7As/GaAs quantum-well solar cells," *J. Appl. Phys.*, vol. 115, no. 4, p. 044303, Jan. 2014.

[41] J. Rybczynski, U. Ebels, and M. Giersig, "Large-scale, 2D arrays of magnetic nanoparticles," *Colloids Surfaces A Physicochem. Eng. Asp.*, vol. 219, no. 1–3, pp. 1–6, Jun. 2003.

[42] P. I. Stavroulakis, N. Christou, and D. Bagnall, "Improved deposition of large scale ordered nanosphere monolayers via liquid surface self-assembly," *Mater. Sci. Eng. B*, vol. 165, no. 3, pp. 186–189, Dec. 2009.

[43] A. Trzaskowska, S. Mielcarek, B. Graczykowski, B. Mroz, P. Patoka, and M. Giersig, "The effect of nickel nanostructure on surface waves propagation in silicon support," *J. Alloys Compd.*, vol. 527, pp. 96–100, Jun. 2012.

[44] F. Xie, A. Centeno, B. Zou, M. P. Ryan, D. J. Riley, and N. M. Alford, "Tunable synthesis of ordered zinc oxide nanoflower-like arrays.," *J. Colloid Interface Sci.*, vol. 395, pp. 85–90, Apr. 2013.

[45] Y. Yu, B. Ai, H. Möhwald, Z. Zhou, G. Zhang, and B. Yang, "Fabrication of Binary and Ternary Hybrid Particles Based on Colloidal Lithography," *Chem. Mater.*, vol. 24, no. 23, pp. 4549–4555, Dec. 2012.

[46] X. Meng and D. Qiu, "Gas-flow-induced reorientation to centimeter-sized two-dimensional colloidal single crystal of polystyrene particle.," *Langmuir*, vol. 30, no. 11, pp. 3019–23, Mar. 2014.

[47] C. L. Cheung, R. J. Nikolić, C. E. Reinhardt, and T. F. Wang, "Fabrication of nanopillars by nanosphere lithography," *Nanotechnology*, vol. 17, no. 5, pp. 1339–1343, Mar. 2006.

[48] C.-C. Ho, P.-Y. Chen, K.-H. Lin, W.-T. Juan, and W.-L. Lee, "Fabrication of monolayer of polymer/nanospheres hybrid at a water-air interface.," *ACS Appl. Mater. Interfaces*, vol. 3, no. 2, pp. 204–8, Feb. 2011.

[49] L. Li, T. Zhai, H. Zeng, X. Fang, Y. Bando, and D. Golberg, "Polystyrene sphere-assisted one-dimensional nanostructure arrays: synthesis and applications," *J. Mater. Chem.*, vol. 21, no. 1, p. 40, 2011.

[50] X. Cai, R. Zhu, and G. Hu, "Experimental study for metamaterials based on dielectric resonators and wire frame," *Metamaterials,* vol. 2, no. 4, pp. 220–226, Dec. 2008.

[51] Q. Zhao, L. Kang, B. Du, H. Zhao, Q. Xie, X. Huang, B. Li, J. Zhou, and L. Li, "Experimental demonstration of isotropic negative permeability in a three-dimensional dielectric composite.," *Phys. Rev. Lett.*, vol. 101, p. 027402, 2008.

[52] F. Zhang, Q. Zhao, L. Kang, J. Zhou, and D. Lippens, "Experimental verification of isotropic and polarization properties of high permittivity-based metamaterial," *Phys. Rev. B*, vol. 80, no. 19, p. 195119, Nov. 2009.

[53] B.-I. Popa and S. Cummer, "Compact Dielectric Particles as a Building Block for Low-Loss Magnetic Metamaterials," *Phys. Rev. Lett.*, vol. 100, no. 20, p. 207401, May 2008.

[54] T. Lepetit, E. Akmansoy, and J.-P. Ganne, "Experimental measurement of negative index in an all-dielectric metamaterial," *Appl. Phys. Lett.*, vol. 95, no. 12, p. 121101, Sep. 2009.

[55] C. L. Holloway, E. F. Kuester, J. Baker-Jarvis, and P. Kabos, "A double negative (DNG) composite medium composed of magnetodielectric spherical particles embedded in a matrix," *IEEE Trans. Antennas Propag.*, vol. 51, no. 10, pp. 2596–2603, Oct. 2003.

[56] K. C. Huang, M. L. Povinelli, and J. D. Joannopoulos, "Negative effective permeability in polaritonic photonic crystals," *Appl. Phys. Lett.*, vol. 85, no. 4, pp. 543–545, 2004.

[57] M. Wheeler, "Three-dimensional array of dielectric spheres with an isotropic negative permeability at infrared frequencies," *Phys. Rev. B*, vol. 72, no. 19, p. 193103, 2005.

[58] A. Ahmadi and H. Mosallaei, "Physical configuration and performance modeling of all-dielectric metamaterials," *Phys. Rev. B*, vol. 77, no. 4, p. 045104, Jan. 2008.

[59] J. Schuller, R. Zia, T. Taubner, and M. Brongersma, "Dielectric Metamaterials Based on Electric and Magnetic Resonances of Silicon Carbide Particles," *Phys. Rev. Lett.*, vol. 99, no. 10, p. 107401, Sep. 2007.

[60] K. Vynck, D. Felbacq, E. Centeno, A. Căbuz, D. Cassagne, and B. Guizal, "All-Dielectric Rod-Type Metamaterials at Optical Frequencies," *Phys. Rev. Lett.*, vol. 102, no. 13, p. 133901, Mar. 2009.

[61] J. C. Ginn, I. Brener, D. W. Peters, J. R. Wendt, J. O. Stevens, P. F. Hines, L. I. Basilio, L. K. Warne, J. F. Ihlefeld, P. G. Clem, and M. B. Sinclair, "Realizing Optical Magnetism from Dielectric Metamaterials," *Phys. Rev. Lett.*, vol. 108, no. 9, p. 097402, Feb. 2012.

[62] L. I. Basilio, L. K. Warne, W. L. Langston, W. A. Johnson, and M. B. Sinclair, “Microwave-Frequency, Negative-Index Metamaterial Designs Based on Degenerate Dielectric Resonators,” *IEEE Antennas Wirel. Propag. Lett.*, vol. 11, pp. 113–116, 2012.

[63] L. K. Warne, L. I. Basilio, W. L. Langston, W. A. Johnson, and M. B. Sinclair, “PERTURBATION THEORY IN THE DESIGN OF DEGENERATE RECTANGULAR DIELECTRIC RESONATORS,” *Prog. Electromagn. Res. B*, vol. 44, pp. 1–29, 2012.

[64] A. Evlyukhin, C. Reinhardt, and B. Chichkov, “Multipole light scattering by nonspherical nanoparticles in the discrete dipole approximation,” *Physical Review B*, vol. 84. 2011.

[65] Y. Yang, W. Wang, P. Moitra, I. I. Kravchenko, D. P. Briggs, and J. Valentine, “Dielectric meta-reflectarray for broadband linear polarization conversion and optical vortex generation.,” *Nano Lett.*, vol. 14, no. 3, pp. 1394–9, Mar. 2014.

[66] A. E. Miroshnichenko and Y. S. Kivshar, “Fano Resonances in All-Dielectric Oligomers,” 2012.

[67] I. Staude, A. E. Miroshnichenko, M. Decker, N. T. Fofang, S. Liu, E. Gonzales, J. Dominguez, T. S. Luk, D. N. Neshev, I. Brener, and Y. Kivshar, “Tailoring Directional Scattering through Magnetic and Electric Resonances in Subwavelength Silicon Nanodisks.,” *ACS Nano*, vol. 7, no. 9, pp. 7824–7832, Aug. 2013.

[68] M. Decker, I. Staude, M. Falkner, J. Dominguez, D. N. Neshev, I. Brener, T. Pertsch, and Y. S. Kivshar, “High-Efficiency Dielectric Huygens’ Surfaces,” *Adv. Opt. Mater.*, p. n/a–n/a, Jan. 2015.

[69] A. E. Krasnok, C. R. Simovski, P. A. Belov, and Y. S. Kivshar, “Superdirective dielectric nanoantennas.,” *Nanoscale*, vol. 6, no. 13, pp. 7354–61, Jul. 2014.

[70] I. Staude, M. Decker, E. Rusak, D. N. Neshev, and I. Brener, “Active Tuning of All-Dielectric,” no. 4, pp. 4308–4315, 2015.

[71] S. Liu, M. B. Sinclair, T. S. Mahony, Y. C. Jun, S. Campione, J. Ginn, D. A. Bender, J. R. Wendt, J. F. Ihlefeld, P. G. Clem, J. B. Wright, and I. Brener, “Optical magnetic mirrors without metals,” *Optica*, vol. 1, no. 4, p. 250, Oct. 2014.

[72] F. Aieta, M. A. Kats, P. Genevet, and F. Capasso, “Achromatic metasurface optical components by dispersive phase compensation,” Nov. 2014.

[73] R. M. Bakker, D. Permyakov, Y. F. Yu, D. Markovich, R. Paniagua-Domínguez, L. Gonzaga, A. Samusev, Y. Kivshar, B. Luk’yanchuk, and A. I. Kuznetsov, “Magnetic and Electric Hotspots with Silicon Nanodimers.,” *Nano Lett.*, Feb. 2015.

[74] D.-H. Kwon and D. H. Werner, “Low-index metamaterial designs in the visible spectrum,” *Opt. Express*, vol. 15, no. 15, p. 9267, Jul. 2007.

[75] E. J. R. Vesseur, T. Coenen, H. Caglayan, N. Engheta, and A. Polman, “Experimental Verification of n=0 Structures for Visible Light,” *Phys. Rev. Lett.*, vol. 110, p. 013902, 2013.

[76] S. Enoch, G. Tayeb, P. Sabouroux, N. Guérin, and P. Vincent, “A metamaterial for directive emission.,” *Phys. Rev. Lett.*, vol. 89, p. 213902, 2002.

[77] D. Adams, S. Inampudi, T. Ribaudo, D. Slocum, S. Vangala, N. Kuhta, W. Goodhue, V. Podolskiy, and D. Wasserman, “Funneling Light through a Subwavelength Aperture with Epsilon-Near-Zero Materials,” *Phys. Rev. Lett.*, vol. 107, no. 13, p. 133901, Sep. 2011.

[78] X. Huang, Y. Lai, Z. H. Hang, H. Zheng, and C. T. Chan, “Dirac cones induced by accidental degeneracy in photonic crystals and zero-refractive-index materials.,” *Nature materials*, vol. 10. pp. 582–586, 2011.

[79] S. Yun, Z. H. Jiang, Q. Xu, Z. Liu, D. H. Werner, and T. S. Mayer, “Low-loss impedance-matched optical metamaterials with zero-phase delay.,” *ACS Nano*, vol. 6, pp. 4475–82, 2012.

[80] L.-G. Wang, Z.-G. Wang, J.-X. Zhang, and S.-Y. Zhu, “Realization of Dirac point with double cones in optics,” *Opt. Lett.*, vol. 34, no. 10, p. 1510, May 2009.

[81] P. Moitra, Y. Yang, Z. Anderson, I. I. Kravchenko, D. P. Briggs, and J. Valentine, “Realization of an all-dielectric zero-index optical metamaterial,” *Nat. Photonics*, vol. 7, no. 10, pp. 791–795, Aug. 2013.

[82] K. S. Novoselov, A. K. Geim, S. V Morozov, D. Jiang, M. I. Katsnelson, I. V Grigorieva, S. V Dubonos, and A. A. Firsov, “Two-dimensional gas of massless Dirac fermions in graphene.,” *Nature*, vol. 438, pp. 197–200, 2005.

[83] I. Tsukerman, “Effective parameters of metamaterials: a rigorous homogenization theory via Whitney interpolation,” *Journal of the Optical Society of America B*, vol. 28. p. 577, 2011.

[84] Y. Wu, J. Li, Z.-Q. Zhang, and C. Chan, “Effective medium theory for magnetodielectric composites: Beyond the long-wavelength limit,” *Physical Review B*, vol. 74. 2006.

[85] R. W. Ziolkowski, “Propagation in and scattering from a matched metamaterial having a zero index of refraction.,” *Phys. Rev. E. Stat. Nonlin. Soft Matter Phys.*, vol. 70, p. 046608, 2004.

[86] B. Slovick, Z. G. Yu, M. Berding, and S. Krishnamurthy, “Perfect dielectric-metamaterial reflector,” *Phys. Rev. B*, vol. 88, no. 16, p. 165116, Oct. 2013.

[87] L. I. Basilio, L. K. Warne, W. L. Langston, W. A. Johnson, and M. B. Sinclair, "Microwave-Frequency, Negative-Index Metamaterial Designs Based on Degenerate Dielectric Resonators," *IEEE Antennas Wirel. Propag. Lett.*, vol. 11, pp. 113–116, 2012.

[88] L. K. Warne, L. I. Basilio, W. L. Langston, W. A. Johnson, and M. B. Sinclair, "PERTURBATION THEORY IN THE DESIGN OF DEGENERATE RECTANGULAR DIELECTRIC RESONATORS," *Prog. Electromagn. Res. B*, vol. 44, pp. 1–29, 2012.

[89] X. Chen, T. Grzegorczyk, B.-I. Wu, J. Pacheco, and J. Kong, "Robust method to retrieve the constitutive effective parameters of metamaterials," *Phys. Rev. E*, vol. 70, no. 1, p. 016608, Jul. 2004.

[90] D. R. Smith, D. C. Vier, T. Koschny, and C. M. Soukoulis, "Electromagnetic parameter retrieval from inhomogeneous metamaterials," *Phys. Rev. E*, vol. 71, no. 3, p. 036617, Mar. 2005.

[91] Z. Szabo, G.-H. Park, R. Hedge, and E.-P. Li, "A Unique Extraction of Metamaterial Parameters Based on Kramers–Kronig Relationship," *IEEE Trans. Microw. Theory Tech.*, vol. 58, no. 10, pp. 2646–2653, Oct. 2010.

[92] C. L. Haynes, A. D. McFarland, M. T. Smith, J. C. Hulteen, and R. P. Van Duyne, "Angle-Resolved Nanosphere Lithography: Manipulation of Nanoparticle Size, Shape, and Interparticle Spacing," *J. Phys. Chem. B*, vol. 106, no. 8, pp. 1898–1902, Jan. 2002.

[93] V. Karagodsky, F. G. Sedgwick, and C. J. Chang-Hasnain, "Theoretical analysis of subwavelength high contrast grating reflectors.," *Opt. Express*, vol. 18, no. 16, pp. 16973–88, Aug. 2010.

[94] C. Chase, Y. Rao, W. Hofmann, and C. J. Chang-Hasnain, "1550 nm high contrast grating VCSEL.," *Opt. Express*, vol. 18, no. 15, pp. 15461–6, Jul. 2010.

[95] P. Moitra, B. A. Slovick, Z. Gang Yu, S. Krishnamurthy, and J. Valentine, "Experimental demonstration of a broadband all-dielectric metamaterial perfect reflector," *Appl. Phys. Lett.*, vol. 104, no. 17, p. 171102, Apr. 2014.

[96] "IEEE Xplore Full-Text HTML : Experimental demonstration of an optical artificial perfect magnetic mirror using dielectric resonators." [Online]. Available: http://ieeexplore.ieee.org/xpls/icp.jsp?arnumber=6349206. [Accessed: 10-Feb-2015].

[97] M. Esfandyarpour, E. C. Garnett, Y. Cui, M. D. McGehee, and M. L. Brongersma, "Metamaterial mirrors in optoelectronic devices.," *Nat. Nanotechnol.*, vol. 9, no. 7, pp. 542–7, Jul. 2014.

[98] H. W. Deckman, "Natural lithography," *Appl. Phys. Lett.*, vol. 41, no. 4, p. 377, Aug. 1982.

[99] U. C. Fischer, “Submicroscopic pattern replication with visible light,” *J. Vac. Sci. Technol.*, vol. 19, no. 4, p. 881, Nov. 1981.

[100] A. Nemiroski, M. Gonidec, J. M. Fox, P. Jean-Remy, E. Turnage, and G. M. Whitesides, “Engineering shadows to fabricate optical metasurfaces.,” *ACS Nano*, vol. 8, no. 11, pp. 11061–70, Nov. 2014.

[101] J. M. Hoffmann, H. Janssen, D. N. Chigrin, and T. Taubner, “Enhanced infrared spectroscopy using small-gap antennas prepared with two-step evaporation nanosphere lithography.,” *Opt. Express*, vol. 22, no. 12, pp. 14425–32, Jun. 2014.

[102] P. Colson, C. Henrist, and R. Cloots, “Nanosphere Lithography: A Powerful Method for the Controlled Manufacturing of Nanomaterials,” *J. Nanomater.*, vol. 2013, pp. 1–19, Jan. 2013.

[103] J. C. Hulteen, “Nanosphere lithography: A materials general fabrication process for periodic particle array surfaces,” *J. Vac. Sci. Technol. A Vacuum, Surfaces, Film.*, vol. 13, no. 3, p. 1553, May 1995.

[104] E. C. Brown, S. K. Wilke, D. A. Boyd, D. G. Goodwin, and S. M. Haile, “Polymer sphere lithography for solid oxide fuel cells: a route to functional, well-defined electrode structures,” *J. Mater. Chem.*, vol. 20, no. 11, p. 2190, Mar. 2010.

[105] J. Chen, P. Dong, D. Di, C. Wang, H. Wang, J. Wang, and X. Wu, “Controllable fabrication of 2D colloidal-crystal films with polystyrene nanospheres of various diameters by spin-coating,” *Appl. Surf. Sci.*, vol. 270, pp. 6–15, Apr. 2013.

[106] P. Colson, R. Cloots, and C. Henrist, “Experimental design applied to spin coating of 2D colloidal crystal masks: a relevant method?,” *Langmuir*, vol. 27, no. 21, pp. 12800–6, Nov. 2011.

[107] N. Denkov, O. Velev, P. Kralchevski, I. Ivanov, H. Yoshimura, and K. Nagayama, “Mechanism of formation of two-dimensional crystals from latex particles on substrates,” *Langmuir*, vol. 8, no. 12, pp. 3183–3190, Dec. 1992.

[108] P. Jiang and M. J. McFarland, “Large-scale fabrication of wafer-size colloidal crystals, macroporous polymers and nanocomposites by spin-coating.,” *J. Am. Chem. Soc.*, vol. 126, no. 42, pp. 13778–86, Oct. 2004.

[109] C.-W. Kuo, J.-Y. Shiu, and P. Chen, “Size- and Shape-Controlled Fabrication of Large-Area Periodic Nanopillar Arrays,” *Chem. Mater.*, vol. 15, no. 15, pp. 2917–2920, Jul. 2003.

[110] T. J. Rehg and G. Higgins, “Spin coating of colloidal suspensions,” *AIChE J.*, vol. 38, no. 4, pp. 489–501, Apr. 1992.

[111] Y. . Zheng, S. . Chua, C. H. . Huan, and Z. . Miao, “Selective growth of GaAs quantum dots on the triangle nanocavities bounded by SiO2 mask on Si substrate by MBE,” *J. Cryst. Growth*, vol. 268, no. 3–4, pp. 369–374, Aug. 2004.

[112] S. Okazaki, “Resolution limits of optical lithography,” *J. Vac. Sci. Technol. B Microelectron. Nanom. Struct.*, vol. 9, no. 6, p. 2829, Nov. 1991.

[113] Y. Xia and G. M. Whitesides, “Soft Lithography,” *Angew. Chemie Int. Ed.*, vol. 37, no. 5, pp. 550–575, Mar. 1998.

[114] A. S. Hall, S. A. Friesen, and T. E. Mallouk, “Wafer-scale fabrication of plasmonic crystals from patterned silicon templates prepared by nanosphere lithography.,” *Nano Lett.*, vol. 13, no. 6, pp. 2623–7, Jun. 2013.

[115] J.-T. Zhang, L. Wang, X. Chao, S. S. Velankar, and S. a. Asher, “Vertical spreading of two-dimensional crystalline colloidal arrays,” *J. Mater. Chem. C*, vol. 1, no. 38, p. 6099, 2013.

[116] A. B. Dark, P. Mode, M. Nanodisk, A. Fabricated, and N.-L. Lithography, “Observation of Absorption-Dominated Bonding Dark Plasmon Mode from Metal À Insulator À Metal Nanodisk Arrays Fabricated by Nanospherical-,” no. 4, pp. 3390–3396, 2012.

[117] Y.-C. Chang, H.-C. Chung, S.-C. Lu, and T.-F. Guo, “A large-scale sub-100 nm Au nanodisk array fabricated using nanospherical-lens lithography: a low-cost localized surface plasmon resonance sensor.,” *Nanotechnology*, vol. 24, no. 9, p. 095302, Mar. 2013.

[118] Y.-C. Chang, S.-C. Lu, H.-C. Chung, S.-M. Wang, T.-D. Tsai, and T.-F. Guo, “High-Throughput Nanofabrication of Infra-red and Chiral Metamaterials using Nanospherical-Lens Lithography,” *Sci. Rep.*, vol. 3, Nov. 2013.

[119] W. Wu, A. Katsnelson, O. G. Memis, and H. Mohseni, “A deep sub-wavelength process for the formation of highly uniform arrays of nanoholes and nanopillars,” *Nanotechnology*, vol. 18, no. 48, p. 485302, Dec. 2007.

[120] C.-H. Hou, S.-Z. Tseng, C.-H. Chan, T.-J. Chen, H.-T. Chien, F.-L. Hsiao, H.-K. Chiu, C.-C. Lee, Y.-L. Tsai, and C.-C. Chen, “Output power enhancement of light-emitting diodes via two-dimensional hole arrays generated by a monolayer of microspheres,” *Appl. Phys. Lett.*, vol. 95, no. 13, p. 133105, 2009.

[121] F. Aieta, P. Genevet, M. A. Kats, N. Yu, R. Blanchard, Z. Gaburro, and F. Capasso, “Aberration-free ultrathin flat lenses and axicons at telecom wavelengths based on plasmonic metasurfaces.,” *Nano Lett.*, vol. 12, no. 9, pp. 4932–6, Sep. 2012.

[122] C. Pfeiffer and A. Grbic, “Metamaterial huygens’ surfaces: Tailoring wave fronts with reflectionless sheets,” *Phys. Rev. Lett.*, vol. 110, p. 197401, 2013.

[123] N. Yu, P. Genevet, M. A. Kats, F. Aieta, J.-P. Tetienne, F. Capasso, and Z. Gaburro, “Light Propagation with Phase Discontinuities: Generalized Laws of Reflection and Refraction,” *Science*, vol. 334. pp. 333–337, 2011.

[124] L. Huang, X. Chen, H. Mühlenbernd, G. Li, B. Bai, Q. Tan, G. Jin, T. Zentgraf, and S. Zhang, “Dispersionless phase discontinuities for controlling light propagation.,” *Nano Lett.*, vol. 12, no. 11, pp. 5750–5, Nov. 2012.

[125] N. Yu and F. Capasso, “Flat optics with designer metasurfaces.,” *Nat. Mater.*, vol. 13, no. 2, pp. 139–50, Feb. 2014.

[126] P. Genevet and F. Capasso, “Holographic optical metasurfaces: a review of current progress.,” *Rep. Prog. Phys.*, vol. 78, no. 2, p. 024401, Jan. 2015.

[127] G. Zheng, H. Mühlenbernd, M. Kenney, G. Li, T. Zentgraf, and S. Zhang, “Metasurface holograms reaching 80% efficiency,” *Nat. Nanotechnol.*, no. February, pp. 1–6, Feb. 2015.

[128] S. Pancharatnam, “Generalized theory of interference, and its applications,” *Proc. Indian Acad. Sci. - Sect. A*, vol. 44, no. 5, pp. 247–262.

[129] M. V. Berry, “The Adiabatic Phase and Pancharatnam's Phase for Polarized Light,” *J. Mod. Opt*, vol 34, no. 11, pp. 1401–1407, 1987.

[130] L. Marrucci, C. Manzo, and D. Paparo, “Pancharatnam-Berry phase optical elements for wave front shaping in the visible domain: Switchable helical mode generation,” *Appl. Phys. Lett.*, vol. 88, no. 22, p. 221102, 2006.

[131] M. Kang, J. Chen, X.-L. Wang, and H.-T. Wang, “Twisted vector field from an inhomogeneous and anisotropic metamaterial,” *J. Opt. Soc. Am. B*, vol. 29, no. 4, p. 572, Mar. 2012.

[132] M. Kang, T. Feng, H.-T. Wang, and J. Li, “Wave front engineering from an array of thin aperture antennas.,” *Opt. Express*, vol. 20, no. 14, pp. 15882–90, Jul. 2012.

[133] F. Gori, “Measuring Stokes parameters by means of a polarization grating,” *Opt. Lett.*, vol. 24, no. 9, p. 584, May 1999.

[134] Z. Bomzon, G. Biener, V. Kleiner, and E. Hasman, “Space-variant Pancharatnam-Berry phase optical elements with computer-generated subwavelength gratings,” *Opt. Lett.*, vol. 27, no. 13, p. 1141, Jul. 2002.

[135] D. Lin, P. Fan, E. Hasman, and M. L. Brongersma, “Dielectric gradient metasurface optical elements,” vol. 345, no. 6194, pp. 5189–5192, 2014.

[136] D. Slocum, D. C. Adams, S. Inampudi, S. Vangala, W. D. Goodhue, V. A. Podolskiy, and D. Wasserman, "Funneling light through a subwavelength aperture using epsilon-near-zero materials," *CLEO 2011 - Laser Sci. to Photonic Appl.*, pp. 1–2, 2011.

[137] A. Miroshnichenko and Y. Kivshar, "Engineering Fano resonances in discrete arrays," *Phys. Rev. E*, vol. 72, no. 5, p. 056611, Nov. 2005.

[138] S. Zhang, D. A. Genov, Y. Wang, M. Liu, and X. Zhang, "Plasmon-Induced Transparency in Metamaterials," *Phys. Rev. Lett.*, vol. 101, no. 4, p. 047401, Jul. 2008.

[139] J. Gu, R. Singh, X. Liu, X. Zhang, Y. Ma, S. Zhang, S. A. Maier, Z. Tian, A. K. Azad, H.-T. Chen, A. J. Taylor, J. Han, and W. Zhang, "Active control of electromagnetically induced transparency analogue in terahertz metamaterials.," *Nat. Commun.*, vol. 3, p. 1151, Jan. 2012.

[140] N. Liu, T. Weiss, M. Mesch, L. Langguth, U. Eigenthaler, M. Hirscher, C. Sönnichsen, and H. Giessen, "Planar metamaterial analogue of electromagnetically induced transparency for plasmonic sensing.," *Nano Lett.*, vol. 10, no. 4, pp. 1103–7, Apr. 2010.

[141] N. Papasimakis, V. A. Fedotov, N. I. Zheludev, and S. L. Prosvirnin, "Metamaterial Analog of Electromagnetically Induced Transparency," *Phys. Rev. Lett.*, vol. 101, no. 25, p. 253903, Dec. 2008.

[142] S. Xiao, V. P. Drachev, A. V Kildishev, X. Ni, U. K. Chettiar, H.-K. Yuan, and V. M. Shalaev, "Loss-free and active optical negative-index metamaterials.," *Nature*, vol. 466, no. 7307, pp. 735–8, Aug. 2010.

[143] P. Tassin, L. Zhang, T. Koschny, E. N. Economou, and C. M. Soukoulis, "Low-Loss Metamaterials Based on Classical Electromagnetically Induced Transparency," *Phys. Rev. Lett.*, vol. 102, no. 5, p. 053901, Feb. 2009.

[144] N. Liu, L. Langguth, T. Weiss, J. Kästel, M. Fleischhauer, T. Pfau, and H. Giessen, "Plasmonic analogue of electromagnetically induced transparency at the Drude damping limit.," *Nat. Mater.*, vol. 8, no. 9, pp. 758–62, Sep. 2009.

[145] S. Zhang, Y.-S. Park, J. Li, X. Lu, W. Zhang, and X. Zhang, "Negative refractive index in chiral metamaterials.," *Phys. Rev. Lett.*, vol. 102, p. 023901, 2009.

[146] Y. Tang and A. E. Cohen, "Optical Chirality and Its Interaction with Matter," *Phys. Rev. Lett.*, vol. 104, no. 16, p. 163901, Apr. 2010.

[147] M. Decker, M. W. Klein, M. Wegener, and S. Linden, "Circular dichroism of planar chiral magnetic metamaterials.," *Opt. Lett.*, vol. 32, pp. 856–858, 2007.

[148] E. Plum, V. A. Fedotov, and N. I. Zheludev, "Optical activity in extrinsically chiral metamaterial," *Appl. Phys. Lett.*, vol. 93, no. 19, p. 191911, Nov. 2008.

[149] N. N. Rosanov, N. V. Vysotina, A. N. Shatsev, A. S. Desyatnikov, and Y. S. Kivshar, “Knotted Solitons in Nonlinear Magnetic Metamaterials,” *Phys. Rev. Lett.*, vol. 108, no. 13, p. 133902, Mar. 2012.

[150] N. N. Rosanov, N. V Vysotina, A. N. Shatsev, I. V Shadrivov, D. A. Powell, and Y. S. Kivshar, “Discrete dissipative localized modes in nonlinear magnetic metamaterials.,” *Opt. Express*, vol. 19, no. 27, pp. 26500–6, Dec. 2011.

[151] Y. S. Kivshar, “Tunable and nonlinear metamaterials: toward functional metadevices,” *Adv. Nat. Sci. Nanosci. Nanotechnol.*, vol. 5, no. 1, p. 013001, Nov. 2013.

[152] K. O’Brien, H. Suchowski, J. Rho, A. Salandrino, B. Kante, X. Yin, and X. Zhang, “Predicting nonlinear properties of metamaterials from the linear response,” *Nat. Mater.*, vol. 14, no. 4, pp. 379–383, Feb. 2015.

[153] “Nonlinear, Tunable and Active Metamaterials | Springer.” [Online]. Available: http://www.springer.com/us/book/9783319083858. [Accessed: 04-May-2015].

[154] L. Kang, Y. Cui, S. Lan, S. P. Rodrigues, M. L. Brongersma, and W. Cai, “Electrifying photonic metamaterials for tunable nonlinear optics.,” *Nat. Commun.*, vol. 5, p. 4680, Jan. 2014.

[155] M. Hentschel, T. Utikal, H. Giessen, and M. Lippitz, “Quantitative modeling of the third harmonic emission spectrum of plasmonic nanoantennas.,” *Nano Lett.*, vol. 12, no. 7, pp. 3778–82, Jul. 2012.

[156] L. Huang, X. Chen, H. Mühlenbernd, H. Zhang, S. Chen, B. Bai, Q. Tan, G. Jin, K.-W. Cheah, C.-W. Qiu, J. Li, T. Zentgraf, and S. Zhang, “Three-dimensional optical holography using a plasmonic metasurface,” *Nat. Commun.*, vol. 4, Nov. 2013.

[157] S. Pleasants, “Metamaterials: Perfect reflection,” *Nat. Photonics*, vol. 8, no. 7, pp. 498–498, Jun. 2014.

[158] F. G. Della Corte, M. Esposito Montefusco, L. Moretti, I. Rendina, and G. Cocorullo, “Temperature dependence analysis of the thermo-optic effect in silicon by single and double oscillator models,” *J. Appl. Phys.*, vol. 88, no. 12, p. 7115, Dec. 2000.

[159] R. Soref and B. Bennett, “Electrooptical effects in silicon,” *IEEE J. Quantum Electron.*, vol. 23, no. 1, pp. 123–129, Jan. 1987.

[160] F. Gan, T. Barwicz, M. A. Popovic, M. S. Dahlem, C. W. Holzwarth, P. T. Rakich, H. I. Smith, E. P. Ippen, and F. X. Kartner, “Maximizing the Thermo-Optic Tuning Range of Silicon Photonic Structures,” in *2007 Photonics in Switching*, 2007, pp. 67–68.

[161] D. Kwong, A. Hosseini, J. Covey, Y. Zhang, X. Xu, H. Subbaraman, and R. T. Chen, “On-chip silicon optical phased array for two-dimensional beam steering.,” *Opt. Lett.*, vol. 39, no. 4, pp. 941–4, Feb. 2014.

[162] J. Sun, E. Timurdogan, A. Yaacobi, E. S. Hosseini, and M. R. Watts, “Large-scale nanophotonic phased array.,” *Nature*, vol. 493, no. 7431, pp. 195–9, Jan. 2013.

[163] Q. Xu, B. Schmidt, S. Pradhan, and M. Lipson, “Micrometre-scale silicon electro-optic modulator.,” *Nature*, vol. 435, no. 7040, pp. 325–7, May 2005.